technische universität
dortmund

European **XFEL**

Dissertation
for obtaining the academic degree
Doctor rerum naturalium
(Dr. rer. nat.)

Electronic spin state studies of iron-bearing minerals contained in an X-ray heated Diamond Anvil Cell

Johannes Martin Kaa
born in Erlangen

2023

Lehrstuhl für experimentelle Physik I
Fakultät Physik
Technische Universität Dortmund

Kurzfassung

Ein bedeutender Teil der Erforschung des Inneren von Planeten wird durch die Nachstellung der erwarteten Drücke und Temperaturen in großen Tiefen im Labor durchgeführt. Während Drücke routinemäßig statisch mit einer Diamantstempelzelle erzeugt werden, um den Druckbereich in den meisten Planeten des Sonnensystems abzudecken (bis ca. 10 Mbar), sind gleichzeitige Temperaturerhöhungen ein heikles Thema, insbesondere in Verbindung mit *in-situ*-Röntgenanalyse mit hohen Belichtungszeiten. In dieser Arbeit stellen wir einen neuen Ansatz zur Bestimmung elektronischer Zustände von Materie bei hohen Drücken und Temperaturen vor, bei dem Proben in Diamantstempelzellen (DACs) durch ultrakurze und intensive Röntgenimpulse erhitzt werden, die auch zur Erzeugung für das spinzustandsensitive Röntgenemissionssignal (XES) und das struktur-empfindliche Röntgenbeugungssignal (XRD) dienen. In dem Proof-of-Concept-Experiment in der Vakuumkammer 1 (IC1) am HED-Instrument haben wir mit dieser Kombination an Messtechniken $FeCO_3$ bis zu der Schmelztemperatur bei 51 GPa erhitzt und dadurch einen durch einen Temperaturanstieg angetriebenen elektronischen Spinübergang von niedrigem Spin zu hohem Spin im Fe induziert. Nach der Konzeption, dem Bau und der Inbetriebnahme eines dedizierten von Hámos-Spektrometers in IC1 haben wir $(Fe_{0.5}Mg_{0.5})O$ bei 100 GPa und FeS zwischen 5 to 25 GPa bei hohen Temperaturen gemessen. Letzteres diente als vereinfachtes Modell für den Marsmantel und -kern und lieferte uns neue Informationen zur Erweiterung der erst kürzlich veröffentlichten seismischen Messungen. Darüber hinaus wurde das Setup für zukünftige zeitaufgelöste XES von Proben in einer DAC und inelastische Röntgenstreuungstechniken von freistehenden Proben getestet und steht für Benutzerexperimente am European X-ray Free Electron Laser zur Verfügung.

Abstract

A significant part of researching the interior of planets is done by recreating the pressures and temperatures, that are expected in large depths, in the laboratory. While pressures are routinely created statically with a diamond anvil cell to cover the pressure ranges in most planets of the solar system (up to $\approx 10\,\text{Mbar}$), simultaneous temperature increases are a more delicate topic, especially when combined with *in-situ* X-ray analysis with high exposure times. In this work, we introduce a novel approach of determining electronic states of matter at high pressures and temperatures by combining diamond anvil cells (DACs) with heating via ultra-short and intense X-ray pulses, which also serve as a probe of the spin state sensitive X-ray emission (XES) signal and structural sensitive X-ray diffraction (XRD). In the proof-of-concept experiment in the vacuum chamber 1 (IC1) at the HED instrument, we heated $FeCO_3$ up to melting temperatures at $51\,\text{GPa}$ with this technique and caused a temperature-driven electronic low spin to high spin transition in the Fe. After designing, building and commissioning a dedicated von Hámos spectrometer in IC1 we measured structural and electronic spin state changes for $(Fe_{0.5}Mg_{0.5})O$ at $100\,\text{GPa}$ and FeS between 5 to $25\,\text{GPa}$ at high temperatures. The latter sample served as a simplified model for the Martian mantle and core, giving us unique information to expand on the just recently published seismic measurements. Additionally, the setup was tested for future time-resolved XES from a DAC and inelastic X-ray scattering techniques of free-standing samples and is available for user experiments at the European X-ray free electron laser.

Acknowledgments

work.

My last but not least thanks go to my friends and family, especially my wife Teresa, for sticking with me throughout the highs and lows that come with working at a synchrotron facility, and to my soon-to-be-born son Julius, for waiting until the very last second.

Publications

Publications as first author

- **Kaa, J. M.**, Konôpková, Z., Preston, T. R., Cerantola, V., Sahle, C. J., Förster, M., Albers, C., Libon, L., Sakrowski, R., Wollenweber, L., Buakor, K., Dwivedi, A., Mishchenko, M., Nakatsutsumi, M., Plückthun, C., Schwinkendorf, J.-P., Spiekermann, G., Thiering, N., Petitgirard, S., … Sternemann, C. (2023). A von Hámos spectrometer for diamond anvil cell experiments at the High Energy Density Instrument of the European X-ray Free-Electron Laser. In Journal of Synchrotron Radiation (Vol. 30, Issue 4). International Union of Crystallography (IUCr). https://doi.org/10.1107/s1600577523003041

- **Kaa, J. M.**, Sternemann, C., Appel, K., Cerantola, V., Preston, T. R., Albers, C., Elbers, M., Libon, L., Makita, M., Pelka, A., Petitgirard, S., Plückthun, C., Roddatis, V., Sahle, C. J., Spiekermann, G., Schmidt, C., Schreiber, A., Sakrowski, R., Tolan, M., … Konôpková, Z. (2022). Structural and electron spin state changes in an X-ray heated iron carbonate system at the Earth's lower mantle pressures. In Physical Review Research (Vol. 4, Issue 3). American Physical Society (APS). https://doi.org/10.1103/physrevresearch.4.033042

Publications as Co-author

- Albers, C., Sakrowski, R., Thiering, N., Libon, L., Spiekermann, G., **Kaa, J. M.**, Gretarsson, H., Sundermann, M., Tolan, M., Wilke, M., & Sternemann, C. (2023). High-efficiency X-ray emission spectroscopy of cold-compressed Fe_2O_3 and laser-heated pressurized $FeCO_3$ using a von Hámos spectrometer. In Journal of Analytical Atomic Spectrometry. Royal Society of Chemistry (RSC). https://doi.org/10.1039/d3ja00014a

- Albers, C., Thiering, N., Sakrowski, R., Gretarsson, H., **Kaa, J. M.**, Sundermann, M., Tolan, M., Wilke, M., & Sternemann, C. (2022). Non-resonant and resonant X-ray emission at high pressure using a von Hámos setup: the case of FeO. In Journal of Physics: Conference Series (Vol. 2380, Issue 1, p. 012128). IOP Publishing. https://doi.org/10.1088/1742-6596/2380/1/012128

- Albers, C., Sakrowski, R., Libon, L., Spiekermann, G., Winkler, B., Schmidt, C., Bayarjargal, L., Cerantola, V., Chariton, S., Giordano, N., Gretarsson, H., **Kaa, J. M.**, Liermann, H.-P., Sundermann, M., Thiering, N., Tolan, M.,

Wilke, M., & Sternemann, C. (2022). Fe^{3+}-hosting carbon phases in the deep Earth. In Physical Review B (Vol. 105, Issue 8). American Physical Society (APS). https://doi.org/10.1103/physrevb.105.085155

- Zastrau, U., Appel, K., Baehtz, C., Baehr, O., Batchelor, L., Berghäuser, A., Banjafar, M., Brambrink, E., Cerantola, V., Cowan, T. E., Damker, H., Dietrich, S., Di Dio Cafiso, S., Dreyer, J., Engel, H.-O., Feldmann, T., Findeisen, S., Foese, M., Fulla-Marsa, D., …, **Kaa, J. M.**, …, Tschentscher, T. (2021). The High Energy Density Scientific Instrument at the European XFEL. In Journal of Synchrotron Radiation (Vol. 28, Issue 5, pp. 1393–1416). International Union of Crystallography (IUCr). https://doi.org/10.1107/s1600577521007335

- Randolph, L., Banjafar, M., Preston, T. R., Yabuuchi, T., Makita, M., Dover, N. P., Rödel, C., Göde, S., Inubushi, Y., Jakob, G., **Kaa, J. M.**, Kon, A., Koga, J. K., Ksenzov, D., Matsuoka, T., Nishiuchi, M., Paulus, M., Schon, F., Sueda, K., … Nakatsutsumi, M. (2022). Nanoscale subsurface dynamics of solids upon high-intensity femtosecond laser irradiation observed by grazing-incidence x-ray scattering. In Physical Review Research (Vol. 4, Issue 3). American Physical Society (APS). https://doi.org/10.1103/physrevresearch.4.033038

- Husband, R. J., Strohm, C., Appel, K., Ball, O., … **Kaa, J. M.**, …, Zastrau, U., Jenei, Z. & Lierman, H.-P. (2023). An MHz X-ray diffraction set-up for dynamic compression experiments in the diamond anvil cell. Accepted in Journal of Synchrotron Radiation. International Union of Crystallography (IUCr).

- Biedermann, N., Morgenroth, W., Spiekermann, G., **Kaa, J. M.**, …, Wilke, M., Appel, K. (2023). Stability and chemical reactions of carbonates in presence of Mg-Fe- silicates at conditions of the Earth's mantle. Submitted to Earth and Planetary Science Letters.

- Libon, L., Spiekermann, G., Blanchard, I., **Kaa, J. M.**, …, Hennet, L, Wilke, M. (2023). Reevaluating the fate of subducted magnesite in the Earth's lower mantle. Submitted to Earth and Planetary Science Letters.

- Nicolas, J., David, C., Konôpková, Z., … **Kaa, J. M.**, …, Mezouar, M., Garbarino, G., Morard, G (2023). MHz free electron laser X-ray diffraction and Modeling of pulsed laser-heated diamond anvil cell. Submitted to Journal of Applied Physics

Public outreach

- Wells, S. (2022). Hot Measure of Spin States Under Pressure. In Physics (Vol. 15). American Physical Society (APS). https://doi.org/10.1103/physics.15.s99

- Wilson, R. (2023). Annual Highlights: A journey to the center of the Earth. Annual Report 2022, Developments, Results, Impressions. European XFEL GmbH.

Contents

List of Figures

1 Introduction

Researching the deep interior of planets such as the Earth or let alone its neighbours can be particularly challenging, for it is covered under hundreds of kilometres of rocks (and in some cases are millions of kilometres away from the Earth) with no way of getting there. Direct samples can only be taken when e.g. Earth ejects them as volcanic activity or inclusions in diamonds formed below cratons [1, 2, 3]. Thus, our knowledge about the interior of planets is mainly based on those snapshots of specific parts of the interior, geochemical measurements of over a billion years old meteoroids having chondritic composition (composition of the early solar system), seismic measurements, tidal deformation measurements and experiments, recreating conditions from planets interior in the lab. Convoluting this information, our scientific picture of the Earth's interior improved significantly in the past decades, allowing us to understand its geological history and current state. Enabled by the Martian InSight mission [4, 5], carrying equipment for measuring seismic activity, Mars is the next planet in line to reveal its information down to its not yet proven solid inner core. Seismic waves, caused by meteoroid impacts are measured travelling through the Martian body, yielding information about the density and aggregate state [6, 7]. By now it is well known, that the pressure (p) in the interior of rocky planets, with roughly the size of the Earth, can reach tens to hundreds of GPa with temperatures (T) above 2000 K. Their cores usually consist of iron and nickel rich phases with some parts of light elements, such as oxygen, carbon or sulfur [8]. Having this information the core of the planets can be "recreated" during experiments in the laboratory.

The research of samples with those compositions at the appropriate pT conditions is usually conducted using the static high p environment of a Diamond anvil cell (DAC). In combination with resistive heating or laser heating to create high T, the samples can undergo planetary interior conditions and can be studied quasi-*in-situ*. To achieve a sufficient signal output for the applied measurement at those conditions, e.g. X-ray diffraction (XRD) or X-ray emission spectroscopy (XES), the high photon flux at a synchrotron or FEL source compared to an X-ray tube usually becomes necessary. Extreme-condition beamlines are well established at nearly all synchrotron facilities and are equipped with a DAC sample environment and different heating techniques.

With the development and increasing availability of hard X-ray free electron laser (FEL) sources in the last decade, it becomes possible to exploit the highly intense and short X-ray pulses to X-ray heat the samples contained in a DAC via so-called "isochoric X-ray heating". This recently implemented method [9] allows for many new approaches and sets the stone for other DAC-related developments at X-ray FELs (XFELs), such as probing laser-driven shock compression from pre-compressed samples or exploiting the pulsed pattern for piezo-driven compression. Both of which are, or will be implemented in the near future. This yields the opportunity to research matter in a phase space, which can not be achieved at the current state.

This thesis presents the results of approaching and implementing an extension to X-ray heating to research the electronic spin states of samples under extreme p and T, utilizing the state-of-the-art combination of pulsed X-ray heated DACs at a hard X-ray FEL and measurements of the spin state sensitive fluorescence. The essential part of this project is a dedicated spectrometer, specifically designed for this purpose. The presented data showcases the possibilities and limits of this new approach, allowing for making statements about possible future prospects connected to this approach.

The present work is structured in chronological order of the conducted experiments. CHA.2 explains the theory behind the methods used for this thesis. The proof-of-principle (November 2019, CHA.3), presenting the well-researched $FeCO_3$ system at the Earth's lower mantle p and T, showcases the capabilities of combining DACs with pulsed X-ray heating while measuring XES. Extensive *ex-situ* measurements were conducted to get the full picture of the experimental data collected *in-situ*. To continue from here, the designing, implementation, testing and commissioning of the spectrometer setup (2020 to 2022, CHA.4) is presented in the form of measurements of multiple samples and sample environments. This includes DAC experiments, as well as measurements on free-standing metal foils, powders and crystalline diamond samples. The setup is dedicated to XES measurements and, as it is shown, reaches its limits at measurements which provide a lower photon yield, such as X-ray Raman scattering. The first major scientific case using this setup (2022, CHA.5) is, besides others, FeS at the Martian core conditions. It is one of the first studies of the emission signal of this mineral at the given pT conditions and helps to understand the processes and formation of our planet and its neighbours. As an outlook CHA. 6 presents future possibilities of the setup and concludes the presented work.

2 Theory and applied methods

By explaining the fundamentals of interactions between X-ray photons and atoms and the resulting possibilities to study the nature of those atoms from their electron configuration via inelastic X-ray scattering to the structure, hosting the atoms via X-ray diffraction, this chapter should give an introduction to the experimental work done for this project. It also includes the basics of short-pulsed X-rays produced by the European X-ray free electron laser and the static high-pressure environment of a diamond anvil cell and how the combination of both techniques can be computed using FE-simulations. The chapter is to most parts based on Schülke [10], Hau-Riege [11], and Willmott [12].

2.1 X-ray - matter interaction

When an X-ray photon in the hard X-ray regime described by a wave vector $\boldsymbol{k_1}$ with an energy $\hbar\omega_1$ and a polarisation $\boldsymbol{\varepsilon_1}$ hits an electron of a sample, there exist three possible interactions. The photon can transfer all of its energy to the electron, ejecting the electron from its bound state and removing the photon from the system. The probability of this photoelectric effect is higher when the energy of the photon is slightly above the specific binding energy of the electron. When only a portion of the energy $\hbar\omega_1$ is transmitted to the bound electron, the scattered photon can be defined by the wave vector $\boldsymbol{k_2}$, energy $\hbar\omega_2$ and polarisation $\boldsymbol{\varepsilon_2}$ with a scattering angle of 2θ (see FIG. 2.1). Through this process the energy of the system is changed by $\hbar\omega_Q = \hbar\omega_1 - \hbar\omega_2$ with a momentum transfer of $\hbar\boldsymbol{Q} = \hbar\boldsymbol{k_1} - \hbar\boldsymbol{k_2}$. The difference between the vectors of $\boldsymbol{k_1}$ and $\boldsymbol{k_2}$ relative to the scattering angle 2θ is

$$Q^2 = k_1^2 + k_2^2 - k_1 k_2 \cos(2\theta). \tag{2.1}$$

The inelastically scattered photon can be collected and yields information about the electrons of the sample further described in SUBSEC. 2.1.2. Additionally, intra-atomic electron transitions producing secondary photons yield especially information

about the electronic spin state, as described in SUBSEC. 2.1.3.

If the photon is scattered (quasi-)elastically on the electron distribution of the sample, the energy of the scattered photon is $\hbar\omega_2 \approx \hbar\omega_1$. For that case, the absolute value of the wave vector transfer can be approximated by

$$Q = 2|\boldsymbol{k_1}|sin(\theta) = \frac{4\pi}{\lambda}sin(\theta), \tag{2.2}$$

with $|\boldsymbol{k_1}| = k_1 = {}^{2\pi}/\lambda$ [12]. Elastically scattered photons enable X-ray diffraction (XRD) measurements, further described in SUBSEC. 2.1.1.
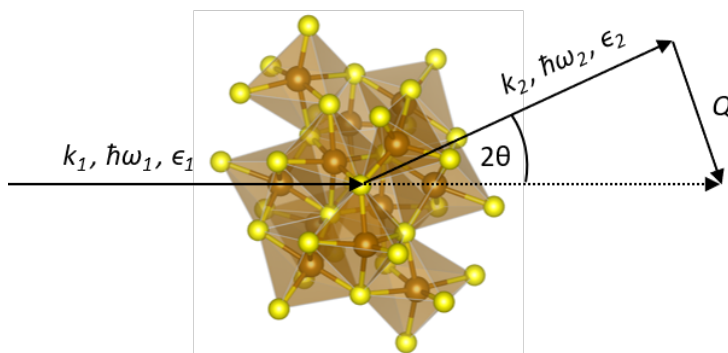
Figure 2.1: Scattering schematics of an X-ray photon ($\boldsymbol{k_1}$, $\hbar\omega_1$, $\boldsymbol{\varepsilon_1}$) on a sample with a scattering angle of 2θ to a scattered photon ($\boldsymbol{k_2}$, $\hbar\omega_2$, $\boldsymbol{\varepsilon_2}$) for the elastic case. The energy deposit on the sample is $\hbar\omega_Q = \hbar\omega_1 - \hbar\omega_2$.

2.1.1 X-ray diffraction

When photons are scattered elastically, the incoming X-ray beam can get diffracted by the crystal lattice of the sample if the Laue condition for constructive interference in the reciprocal crystal lattice is fulfilled. For this to happen, the transfer vector $\boldsymbol{Q}$ needs to be equal to a reciprocal wave vector transfer $\boldsymbol{G_{hkl}}$ for a d-spacing d_{hkl} between lattice planes with the Miller indices (hkl) with

$$|\boldsymbol{G_{hkl}}| = \frac{2\pi}{d_{hkl}}. \tag{2.3}$$

By combining EQ. 2.3 and EQ. 2.2, we get the Bragg condition

$$\frac{2\pi}{d_{hkl}} = \frac{4\pi}{\lambda}sin(\theta)$$

$$\Rightarrow nd_{hkl} = \frac{\lambda}{2sin(\theta)}, \tag{2.4}$$

with the integer n, as the largest common multiple of *hkl*. Hence, with a constant wavelength λ it is possible to measure the, besides others, phase-, pressure (p)- and temperature (T)-sensitive lattice spacing d as a function of the scattering angle θ. Additionally, and further explained in SUBSEC. 2.1.2 and 2.1.3, using a single crystal with a constant d-spacing and using the Bragg condition, we can measure a wavelength spectrum as a function of the Bragg angle θ.

When the roll angle ϕ of the measured crystal relative to the beam is unknown or there are multiple randomly ordered crystallites probed simultaneously, the diffracted signal must be collected by a 2D area detector, in most cases oriented perpendicular to the incoming beam at a distance D, to ensure the collection of the diffracted signal within a certain diffraction angle using a static sample. The diffracted signal appears as a spot on a ring with the radius $r_{2\theta} = tan(2\theta)D$, called Debye-Scherrer-rings. For powdered samples with a grain size below the X-ray spot size on the sample, the diffraction signal appears as a (near-)continuous ring. By measuring a calibrant at a known wavelength λ, the detector geometry can be calibrated and Debye-Scherrer-rings can be converted to 1D intensity plots as a function of 2θ (see scheme in FIG. 2.2). For the presented experiments, this integration was done using DIOPTAS [13]. The geometry calibration was done by refining the signal of a CeO_2-reference using the Fit2D refinement [14]. A polynomial background was fitted and subtracted from each diffraction pattern.
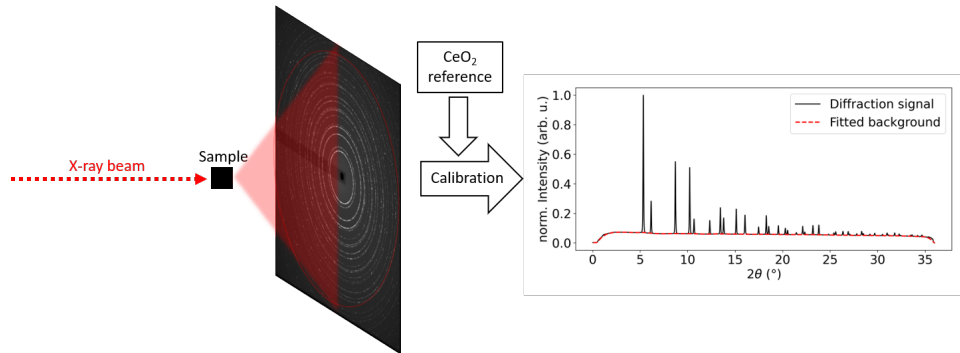
Figure 2.2: XRD data collection from a sample using a 2D area detector and calibration from a CeO_2 reference. A polynomial background (red, dashed) was fitted to the XRD pattern (black). The data was processed using DIOPTAS.

To calculate the relative intensity diffracted for each crystal plane, we first have to establish $\rho_m(r)$ as the electron charge density distribution as a function of r, i.e. the distance from the atomic centre. Using this, we can calculate the atomic scattering

factor of an atom with m electrons [15] as

$$f_m = \int_0^\infty 4\pi r^2 \rho_m \frac{sin(2Qr)}{2Qr} dr, \qquad (2.5)$$

under the assumption that $\lambda \ll \lambda_{AE}$, with the wavelength of an absorption edge λ_{AE}. When taking the complete unit cell into account, the combined scattering amplitude of a *hkl* reflection for M atoms in the unit cell is calculated by

$$F_{hkl} = \sum_{m=1}^M f_m e^{2\pi i (hu_m + kv_m + lw_m)} \qquad (2.6)$$

with the atomic coordinates (u_m, v_m, w_m). Ultimately, the relative intensity of each *hkl* peak, assuming a polycrystalline sample, can be calculated by

$$I_{hkl} = \kappa_i \frac{n}{\nu} (\psi - \psi_0) \lambda^3 |F_{hkl}|^2 e^{(-2M_t - 2M_s)} \qquad (2.7)$$

using an instrument constant κ_i, the unit cell volume ν, a geometric factor $(\psi - \psi_0)$ correcting for polarization and other factors [16], the *hkl*-plane depending structure factor F_{hkl} and a factor $e^{(-2M_t - 2M_s)}$ to include thermal vibrations M_t and static displacements M_s [17]. Thus, information about the structure from the measured sample can be extracted from the position and intensity of the diffraction peaks. When also the chemical composition is known, XRD can be used to identify the phases in the sample.

2.1.2 Inelastic X-ray scattering

The photon yield during an inelastic X-ray scattering (IXS) experiment is given by the scattering cross section σ, which is the scattering rate per photon hitting the target per time interval and area. Using a spectrometer, this value is measured in a solid angle element $d\Omega$, i.e. the accepting area of the analyser crystals, and per energy $d\hbar\omega_2$. Hence, the measured quantity in IXS measurements is the double differential scattering cross section (DDSCS)

$$\frac{d^2\sigma}{d\Omega d\hbar\omega_2} = \frac{\substack{\text{flux of photons scattered into the solid angle element } [\Omega_2, d\Omega_2] \\ \text{and into the range of energy } [\hbar\omega_2, d\hbar\omega_2]}}{\substack{\text{incident photon flux, integrated over the corresponding} \\ \text{ranges of solid angle } d\Omega \text{ and energy } d\hbar\omega_2}} \qquad (2.8)$$

as described by Schülke [10]. The mathematical expression for the DDSCS, neglecting spin-depending contributions, has been established by Kramers and Heisenberg [18] and is known by the Kramers-Heisenberg equation:

$$
\frac{d^2\sigma}{d\Omega d\hbar\omega_2} = \left(\frac{e^2}{mc^2}\right)^2 \left(\frac{\omega_2}{\omega_1}\right) \left| (\boldsymbol{\varepsilon_1} \cdot \boldsymbol{\varepsilon_2}) \langle \mathrm{f}| \sum_j e^{i\boldsymbol{q}\cdot\boldsymbol{r_j}}|i\rangle + \frac{\hbar^2}{m} \sum_n \sum_{jj'} \right.
$$
$$
\left(\frac{\langle \mathrm{f}| \left[\boldsymbol{e_2}\cdot\boldsymbol{p_j}/\hbar\right] e^{-i\boldsymbol{k_2}\cdot\boldsymbol{r_j}}|n\rangle \langle n| \left[\boldsymbol{e_1}\cdot\boldsymbol{p'_j}/\hbar\right] e^{-i\boldsymbol{k_1}\cdot\boldsymbol{r'_j}}|i\rangle}{E_i - E_n + \hbar\omega_1 - i\Gamma_n/2} \right.
$$
$$
\left. \left. + \frac{\langle \mathrm{f}| \left[\boldsymbol{e_1}\cdot\boldsymbol{p_j}/\hbar\right] e^{-i\boldsymbol{k_1}\cdot\boldsymbol{r_j}}|n\rangle \langle n| \left[\boldsymbol{e_2}\cdot\boldsymbol{p'_j}/\hbar\right] e^{-i\boldsymbol{k_2}\cdot\boldsymbol{r'_j}}|i\rangle}{E_i - E_n + \hbar\omega_2} \right) \right|^2 \times \delta(E_i - E_\mathrm{f} + \hbar\omega_Q), \quad (2.9)
$$

for the transition from an initial state $|i\rangle$ with energy E_i to an excited state $|n\rangle$ with energy E_n and lifetime Γ_n and final state $|f\rangle$ with energy E_f, the impulse $\boldsymbol{p}$ and position $\boldsymbol{r}$ for an electron j. This equation describes the resonant and non-resonant scattering process for $|i\rangle \neq |\mathrm{f}\rangle$, with the second term including the resonant conditions. For initial energies significantly different from resonant excitations, this second term can be neglected and the equation can be simplified for the pure non-resonant IXS (NRIXS) process to

$$
\frac{d^2\sigma}{d\Omega d\hbar\omega_2} = \left(\frac{e^2}{mc^2}\right)^2 \left(\frac{\omega_2}{\omega_1}\right) |\boldsymbol{\varepsilon_1} \cdot \boldsymbol{\varepsilon_2}|^2 \left| \langle \mathrm{f}| \sum_j e^{i\boldsymbol{q}\cdot\boldsymbol{r_j}}|i\rangle \right|^2 \times \delta(E_i - E_\mathrm{f} + \hbar\omega_Q), \quad (2.10)
$$

with the Thomson cross-section for purely elastic scattering processes

$$
\left(\frac{d\sigma}{d\Omega}\right)_{\mathrm{Th}} = \left(\frac{e^2}{mc^2}\right)^2 \left(\frac{\omega_2}{\omega_1}\right) |\boldsymbol{\varepsilon_1} \cdot \boldsymbol{\varepsilon_2}|^2, \quad (2.11)
$$

and the remaining term, describes the dynamic structure factor

$$
S(\boldsymbol{Q},\omega) = \left| \langle \mathrm{f}| \sum_j e^{i\boldsymbol{q}\cdot\boldsymbol{r_j}}|i\rangle \right|^2 \times \delta(E_i - E_\mathrm{f} + \hbar\omega_Q). \quad (2.12)
$$

To entangle $S(\boldsymbol{Q},\omega)$ in a similar manner as done in SEC. 2.1.1, we have to establish the time-dependent total electron density as $\rho(\boldsymbol{Q},t) = \rho_c(\boldsymbol{Q},t) + \rho_v(\boldsymbol{Q},t)$ with core electrons ρ_c and weakly bound electrons ρ_v [11]. As the next step, we can set the intermediate scattering function as an equation to calculate the time-dependent correlation of the atomic or molecular positions in the material with

$$
F(\boldsymbol{Q},t) = \frac{1}{N}\langle \rho(\boldsymbol{Q},t)\rho_0(\boldsymbol{Q},0)\rangle, \quad (2.13)
$$

for N particles and the average of the product of the electron density at time $t = 0$ and $t = t$ on an attosecond timescale as shown by e.g. Calegari et al. [19]. The total dynamic structure factor can then be calculated by

$$S(\boldsymbol{Q}, \omega) = \frac{1}{2\pi} \int_{-\infty}^{\infty} F(\boldsymbol{Q}, t) e^{i\omega t} dt. \tag{2.14}$$

This demonstrates the scattering process as a reaction to the system's electron fluctuations at time t as described by Hove [20].

FIG. 2.3 shows a schematic representation of the most common excitations for NRIXS measurements and their order of magnitude for the corresponding $S(\boldsymbol{Q}, \omega)$. It includes (quasi-) elastic scattering with a $h\omega = 0\,\text{eV}$, scattering on the excitation of conduction band electrons, i.e. the bulk plasmon in e.g. a metallic lattice, or core electron excitations, which all were measured as described in CHA. 4. The measurement techniques shown are partially dependent on the measuring geometry and therefore the momentum transfer $\boldsymbol{Q}$.
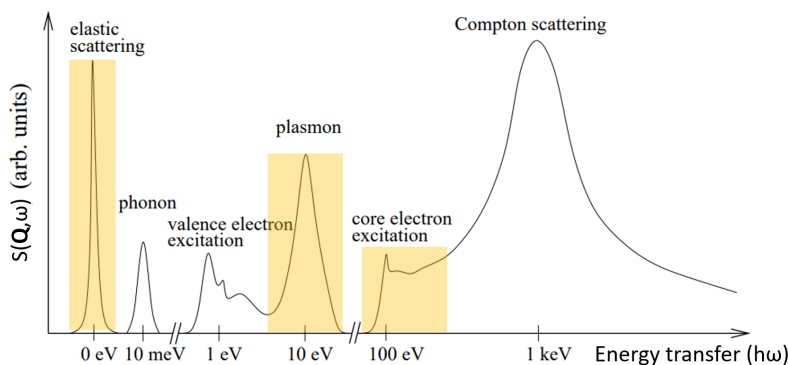
Figure 2.3: Schematic representation of IXS signal taken from a sample with their estimated $S(\boldsymbol{Q}, \omega)$ as a function of the estimated energy ranges ($h\omega$). Measured signals for this work are marked in yellow. Changed after Szabolcs [21]

2.1.3 X-ray emission spectroscopy

If the energy from an incident X-ray photon E_i is higher than that of a bound electron E_e in e.g. the K-shell, this electron is excited into a continuum state (γ) for the non-resonant emission case $E_i \gg E_e$. The atom relaxes from this excited state $|n\rangle$ into a final state $|i\rangle$ by an electron in a higher energy level switching into the lower energy vacancy by emitting the energy difference as a photon. For this process using the Kramers-Heisenberg equation (EQ. 2.9), we can simplify this equation by

only accounting for the second resonant term

$$\frac{d^2\sigma}{d\Omega d\hbar\omega_2} = \left(\frac{e^2}{mc^2}\right)^2 \left(\frac{\omega_2}{\omega_1}\right) \left|\sum_{\text{f}} \frac{\hbar^2}{m} \sum_n \sum_{jj'}\right.$$

$$\left.\frac{\langle \text{f}|\, [\boldsymbol{e_2}\cdot\boldsymbol{p_j}/\hbar]\, e^{-i\boldsymbol{k_2}\boldsymbol{r_j}}|n\rangle\langle n|\, [\boldsymbol{e_1}\cdot\boldsymbol{p'_j}/\hbar]\, e^{-i\boldsymbol{k_1}\boldsymbol{r'_j}}|i\rangle}{E_i - E_n + \hbar\omega_1 - i\Gamma_n/2}\right|^2 \times \delta(E_i - E_{\text{f}} + \hbar\omega_Q), \quad (2.15)$$

as described by Schülke [10]. One has to note that the energy of the emitted photon in X-ray emission spectroscopy (XES) is independent of the energy bandwidth of the incident X-ray beam, which makes it an optimal candidate for X-ray free electron laser (XFEL) experiments that normally provide a broad self-amplified spontaneous emission (SASE) spectrum with $\Delta E/E \approx 10^{-3}$. FIG. 2.5 shows the K-line emissions for Fe^{2+} from the excited non-resonant state $1s^1 3d^6 \gamma$ to $2p^5 3d^6 \gamma$ (Kα), $3p^5 3d^6 \gamma$ (Kβ) and $v^{-1} 3d^6 \gamma$ with a hole in the valence band (vtc). The emitted photons have distinct and element-specific energies depending on the atomic number Z and the principle quantum number n generating emission lines approximated for a hydrogen-like atom by Moseley's Law

$$E_i = hRyZ^2 \left(\frac{1}{n_1^2} - \frac{1}{n_2^2}\right) \qquad (2.16)$$

for a transition from n_1 to n_2 using the Rydberg constant Ry. This does not consider electron-electron or other interactions and therefore usually overestimates the binding energies. The correct values for the energy levels are experimentally determined and are listed in e.g. Henke, Gullikson, and Davis [22]. As an example, the Kα ($2p_{1/2}$ and $2p_{3/2}$ to 1s transition) lines for elementary Fe can then be calculated by the K and L_{II} and L_{III} edge energies to 7112 eV - 719.9 eV = 6392.1 eV and 7112 eV - 706.8 eV = 6405.2 eV, respectively. The two different energy states within the 2p orbital are due to dominant spin-orbital (jj-coupling) interactions, i.e. the interaction between the orbital angular momentum and the magnetic dipole moment due to the electrons spin, resulting in j-values of $1(l) \pm 0.5(s)$. The splitting in the Kα emission line (see FIG. 2.4) based on spin-orbit interactions E_{SO} is more dominant compared to the splitting in the Kβ emission, resulting in a not-separable asymmetric peak (K$\beta_{1,3}$, see FIG. 2.4). However, the Kβ emission line shows stronger 3d-3p electron-electron interactions, which causes a splitting in the case of a high-spin (HS) state, which is discussed in the following.

The splitting of the Kβ emission is caused by the LS-coupling, which assumes the total angular momentum $\boldsymbol{J}$ which is combined with the total orbital momentum $\boldsymbol{L}$ and the total spin angular momentum $\boldsymbol{S}$ from all electrons within the atom. The
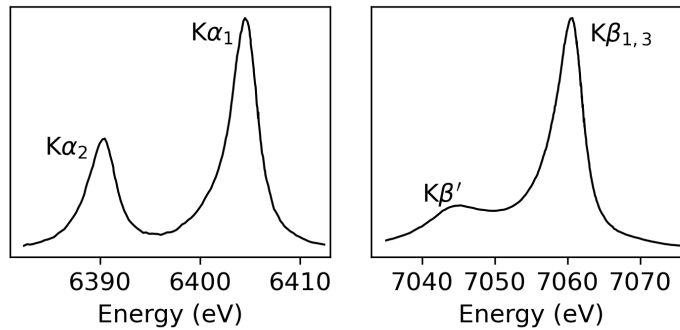
Figure 2.4: Schematics of the $K\alpha_1$ and $K\alpha_2$ [**Left**] and $K\beta_{1,3}$ showing an asymmetry to lower energies and $K\beta'$ [**Right**] emission lines for Fe.

latter is mostly driven by the spin state of the partially filled $3d^6$ orbital for the case of Fe^{2+}. If Fe^{2+} is in an HS state, meaning that the number of unpaired electrons in the 3d orbital is at a maximum, the effect of the LS-coupling is more pronounced and shows a separate $K\beta'$ peak as a shoulder of the asymmetric $K\beta_{1,3}$ main peak (FIG. 2.4. This is due to the difference in energy states if the initially excited electron from the 1s orbital has the same spin as the electrons in the 3d orbital (see FIG. 2.5). Due to the spin momentum conservation, an electron with the same spin from the 3p orbital transitions to the 1s orbital, resulting in an unpaired electron with imposing spin relative to the 3d electrons. Additionally, the main peak shows an asymmetry to lower energies in the case of an HS due to a spin-flip within the 3d orbital. This quasi-multi-electron process increases the energy level of the system due to the exchange energy splitting of spin parallel electrons [23], adding another asymmetric factor to the $K\beta_{1,3}$ peak. Vankó et al. [24] showed that the change of the integrated absolute difference (IAD) of a $K\beta$ emission spectrum compared to a reference spectrum, has a linear dependency on the electronic spin state of the sample. By the increasing asymmetry in the $K\beta_{1,3}$ peak, Lafuerza et al. [25] showed a dependency on the centre-of-mass (ΔM1) shift and the spin state. The effect on the $K\alpha$ emission line shape is smaller due to the larger distance between the 2p-3d orbitals and has been measured as a slight increase in the full-width ad half-max (FWHM) of the $K\alpha_1$ emission line [25].

Vtc transitions are counted as $K\beta$ emission and show the valence/ligand to 1s electron transitions. The different vtc emission lines are referred to as $K\beta_5$ (3d→1s), $K\beta_2$ (mixed 3d,4p and ligand 2p→1s) and the interatomic $K\beta''$ (ligand 2s→1s) emission line. Due to their close relation to the valence electrons of the metal ion, they can be used to study spin states, ligand type and orientation of the ligands [26, 27, 28]).
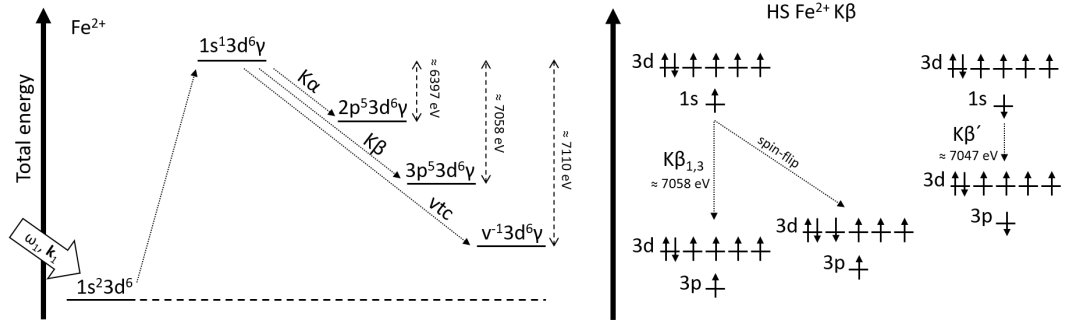
Figure 2.5: [**Left**] Energy change in the Fe^{2+} ion for the non-resonant excitation of a 1s electron into a continuum energy state γ. The incident photon $(\omega_1, \boldsymbol{k}_1)$ excites the ground state to the excited state $1s^1 3d^6 \gamma$. This state changes to $2p^5 3d^6 \gamma$ ($K\alpha$), $3p^5 3d^6 \gamma$ ($K\beta$) and $v^{-1} 3d^6 \gamma$ by interatomic electron transitions. The mean energies for the emission processes are given. [**Right**] When the system is in an HS state, the $K\beta$ peak splits into the $K\beta_{1,3}$ main peak and a $K\beta'$ satellite peak, depending on the spin of the excited electron from the 1s shell. Additionally, due to a spin-flip in the 3d orbital, a third total energy level is possible.

2.1.4 Spectroscopy measurements with a von Hámos spectrometer

The emitted and scattered signal was collected with a von Hámos spectrometer utilizing perfect Si and Ge single crystals with various d-spacings d bent to a radius of $250\,\mathrm{mm}$ or $500\,\mathrm{mm}$. The crystal with the size $l_c \times h_c$, is positioned with a Bragg angle θ_B to the sample in a distance r, equal to the bending radius, to the sample-detector axis h_y. The emitted spectrum from the source is diffracted from the analyser crystal onto the active area of the detector as seen in FIG. 2.6. The diffracted energy is relative to the Bragg angle and the crystal cut with

$$E = hc \frac{n}{2d \sin(\theta_{\mathrm{B}})}, \tag{2.17}$$

using the n-th order reflection. The diffracted signal was focused by the cylindrically bent crystals in the non-dispersive direction, resulting in a line-shaped spectrum. The background correction is shown in FIG. 2.7. The signal is averaged for each pixel in the dispersive direction y over the non-dispersive x-range on the detector. The same is done for an area shifted in x, which is used as background and is subtracted from the signal to correct for sensor gaps and scattering background. The resulting spectrum is energy calibrated by first measuring a metal foil, e.g. Fe, which is fitted to a reference. The calibrated energy range and pixel dispersion are used to calibrate the y-axis for the following runs.

The data quality can be estimated by calculating the signal-to-noise ratio (SNR) by
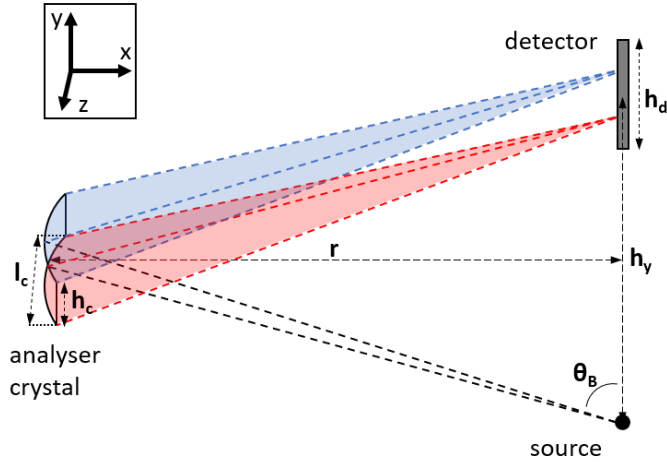
Figure 2.6: Schematic presentation of the von Hámos geometry from a point source with an analyser crystal with a cylindrical bending radius and distance to the source-detector axis **r** and a Bragg angle θ_B. The analyser crystal has a size of $l_c \times h_c$ and the detector sensor in height h_y has a height h_d. The emitted light (black) is diffracted relative to the wavelength into higher (blue) and lower (red) wavelengths. Adapted after Kaa et al. [29].
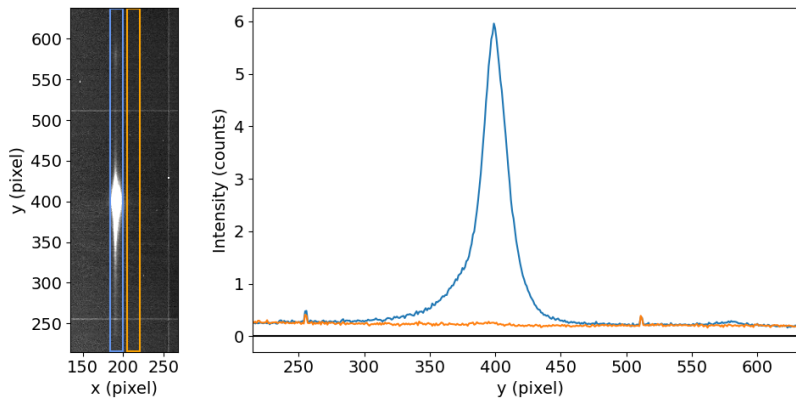
Figure 2.7: [**Left**] Excerpt of the detector array for an example run of the Ni Kβ. The signal (blue) and background (orange) are extracted from the marked areas. [**Right**] The Kβ signal (blue) shows a background including peaks for the array sensor gaps which get corrected by the background signal (orange). For the peak value $I_s = 6$ and the mean background signal $I_b = 0.23$ we can calculate a SNR value of $SNR \approx 12$.

using the peak signal count I_s and the mean background value under the spectrum I_b [30] with

$$SNR = \frac{I_s - I_b}{\sqrt{I_b}}. \tag{2.18}$$

2.2 European X-ray free-electron laser

Synchrotron sources of the 3rd- or 4th generation (e.g. PETRA III, MAX IV) provide pulsed X-ray beams with a pulse duration usually in the 1 to 500 ps range, with exceptions of dedicated fast-pulse beamlines, which can decrease the pulse length down to 400 fs (e.g. [31]). While at XFEL facilities, the photon flux per second can be similar to that of 3rd- and 4th-generation synchrotrons, the X-ray pulses provide a significantly higher photon density, i.e. peak photon flux, with pulse lengths between 10 to 100 fs and up to several hundred of pulses per second.

At the European XFEL in Hamburg, Germany, electron bunches are generated by a Nd:YLF laser beam, converted to an ultra-violet (UV) wavelength, that is shot on a Cs_2Te cathode inside a cavity using the photoelectric effect. The electron bunches are linearly focused by magnetic fields and accelerated by a superconducting radio-frequency (RF) cavity. The close-to-relativistic bunches enter the accelerator, consisting of 96 cavity units, in which the electrons packages are pre-compressed by the sinusoidal RF field. The energy gain for the electrons passing through a cavity with the length L for a position $-0.5L \leq z \leq 0.5L$ at time t and the phase relative to the crest φ_0 with an electric field perpendicular to the velocity of the electrons is

$$E_z(z, t) = E_0 \sin\left(\frac{2\pi z}{L}\right) \sin(\omega t(z) + \varphi_0). \tag{2.19}$$

With the assumption that the change in velocity is negligible and the velocity is close to the speed of light c with the relativistic factor β_0, thus $t = z/\beta_0 c$ the energy change is

$$\Delta W = \int_{-L/2}^{L/2} eE_0 \sin\left(\frac{2\pi z}{L}\right) \sin\left(\frac{\omega z}{\beta c} + \varphi_0\right) dz. \tag{2.20}$$

The change in energy is therefore dependent on the position z of the electrons, which causes an energy gradient within the electron bunch. The electric field is aligned with the position of the electron bunch in such a way, that the electrons in the back achieve a higher ΔW. To achieve bunch lengths below 100 fs, the cavity units are interrupted by three bunch compressors, consisting of a magnetic four-dipole chicane. The higher-energy electrons undergo a smaller diversion compared to the lower-energy

front electrons, compressing the length of the electron bunch. The resulting bunch
length is roughly 20 fs (FWHM) with an electron bunch energy of 10.5 GeV, 14 GeV
or 17.5 GeV after a total accelerator length of 1.7 km [32]. Afterwards, the beam
gets split into three independent undulator systems to provide X-rays for seven
instrumental end stations.

2.2.1 High-Energy-Density instrument

The High-Energy-Density (HED) instrument [33] is situated at the south branch,
called SASE2, which it shares with the Material Imaging and Dynamics (MID)
instrument. The electron beam is sent over 35 undulators with a length of 5 m
each, which consists of periodically ordered dipole magnets. The undulators are
characterised by the factor $K = \mu_k B \lambda_u$ including the magnetic field of the dipole
magnets B and their period λ_u with $\mu_k = {}^e/_{2\pi m_e c}$. SASE2 provides a K values
between 1.65 to 3.9 [34]. The periodic magnetic field, with $B_{max} = 1.1$ T [34], forces
the relativistic electron beam on a slalom path having a radiation power determined
by the Liénards equation after Willmott [12]

$$ P = \frac{2}{3} \frac{e^4 c^3}{(m_e c^2)^4} \xi^2 B^2 = 6.763 \times 10^{-18} \xi [GeV]^2 B[T]^2 \qquad (2.21) $$

with the electron energy ξ and the magnetic field B. Due to the relativistic length
contraction and the Doppler shift for the emitted photons, i.e. relativistic beaming,
the emission from the electrons happens close to exclusively in the forward direction
with a very small divergence of roughly 2 µrad for SASE2 [33]. The wavelength of the
emitted photons can be calculated using the relativistic Lorentz contraction factor
$\gamma = {}^1/\sqrt{1-(v/c)^2}$ by

$$ \lambda = \frac{\lambda_u}{2\gamma^2} \left(1 + \frac{K^2}{1} \right). \qquad (2.22) $$

With the magnetic field and period of the undulator reaching a maximum due to
technical limitations, hard energy X-rays with wavelengths in the Angstrom regime
can be produced for $\gamma > 10000$ which corresponds to an electron energy above 5 GeV.
At SASE2 the photon energy can potentially reach between 3 to 30 keV for electron
beam energies between 8 to 17.5 GeV[34]. Additionally, the electron bunches do not
only interact with the static magnetic field of the undulators but ultimately also with
the electromagnetic field of their emitted photons. The undulator length of several
tens of meters allows this interaction to induce micro-bunching of the electrons within
each electron bunch. This happens due to energy gain or loss of the electrons to and

from the photons via the parallel component of the electric field from the emitted electromagnetic waves. The Lorentz force from the magnetic field of these waves is perpendicular to the velocity of the electron and thus does not change the energy of the electron beam, but has an effect on its direction. The velocity modulation causes electron micro-bunching with the same wavelength as the emitted electromagnetic waves enabling a change from incoherent emission with an amplitude proportional to the number of electrons n_e to coherent emission increasing the radiation amplitude to be proportional to n_e^2 [35]. The resulting emission power is in the order of 1×10^{11} W or up to 3 mJ per 20 fs pulse [33]. The beam is delivered in pulse trains with 10 Hz containing up to 2700 pulses at a repetition rate of up to 4.5 MHz. The provided energy bandwidth for SASE is typical $\Delta E/E \approx 10^{-3}$. Using the self-seeding method, the bandwidth can be reduced significantly [36] as shown in FIG. 2.8.

At the end of the undulators, the electrons are deviated by a magnet and dumped
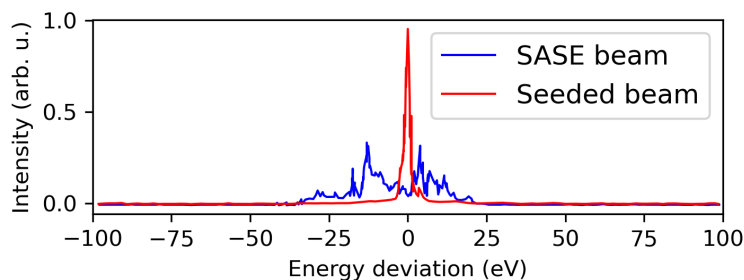
Figure 2.8: Comparison of the energy bandwidth of a SASE beam and a self-seeded beam at 9500 eV. Not to scale. Reproduced after [36].

into a heavy concrete block in the distribution X-ray tunnel (XTD) 1, while the photons are further transported over several mirrors to the experimental station. In XTD 1 and 6 the X-ray beam passes several analysers as well as beam-shaping components and optics. All components are shown in FIG. 2.9. The distribution mirror M3 distributes the beam between the two end stations. It is a Si single crystal with a B_4C coating on the bottom and a Pt coating on the top, for usage at different photon energies. The mirror is cooled by a water cooler, removing the heat via an InGa coating [37]. The X-ray gas monitors (XGMs) in XTD 1 and 6 [38] measure pulse-resolved information about the X-ray beam, including position and energy. The beam is focused with Be compound refractive lenses (CRLs). Intermediate focusing is achieved by CRL1 in XTD1, a focus correction for the monochromators by CRL2 in XTD6 and tight focussing by CRL3 in XHEXP1. The intensity of the beam can be controlled by the two sets of attenuators in XTD 1 and

6, consisting of several polycrystalline diamond plates and Si in several thicknesses, providing various attenuations. For a monochromatic beam, a four-bounce Si(111) and a high-res Si(533) monochromators are available providing an energy bandwidth of $\Delta E/E = 10^{-4}$ and $\Delta E/E = 10^{-6}$, respectively. The sample is placed in the experimental hutch in XHEXP1 in either the vacuum chamber interaction chamber 1 (IC1) for flexible sample environments or 2 (IC2) dedicated to XRD from DACs. Both chambers can be evacuated to a level below 1×10^{-5} mbar. Downstream of XHEXP1 is the beamstop, absorbing the remaining X-ray photons. Depending on the pulse energy and components in the beam, the beamline transmission from the undulators to IC1 is below 50 %. Photodiode imagers up- and downstream of the sample and in the beamstop can be calibrated using the signal from the XGMs. The pulse picker can be used for single pulse shots and temporal alignment of more complex trigger systems.
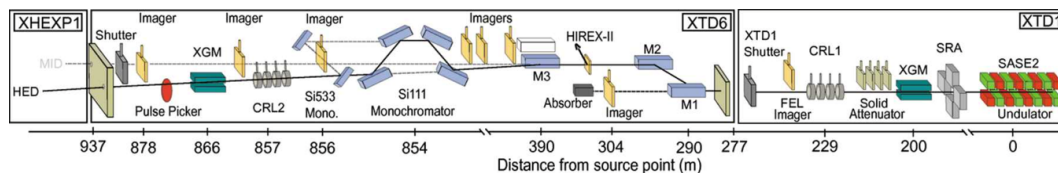
Figure 2.9: Beamline components for XTD 1 and 6 transporting the beam to HED and MID. The X-ray beam after SASE2 passes several slit systems, XGMs, focussing optics, attenuators, imagers and mirrors. If applicable, the Si(111) and Si(533) monochromators are shown as well. A third set of CRLs is located in XHEXP1 (not shown). [33]

2.3 Static high-pressure environment: Diamond Anvil Cell

To recreate the pressures expected in the interior of planets caused by the loading force of hundreds to thousands of km of rocks and melt, the diamond anvil cell (DAC) is the most commonly used device, especially in the pressure regime above 30 GPa. Pressure p can simply be described by a normal force F_n acting on an area A:

$$\mathrm{p} = \frac{F_n}{A}. \tag{2.23}$$

The DAC consists of two anvils made of diamond (mostly single-crystalline), which provide the highest bulk modulus K known in any material, polished along the crystal orientation (100). Both anvils, sitting on WC seats, have a flattened tip called culet with a diameter in the range of most commonly 100 to 1000 µm. The sample is placed in between the parallel aligned culets. A longitudinal force on the culets in an

estimated range of 0.1 to 5 kN is applied e.g. by a set of screws, creating a pressure of up to roughly 150 GPa. With a bevelled diamond, the stress during compression is differently applied in the DAC, allowing for reaching higher pressures [39]. Using so-called 2-stage or double-stage diamond anvils, pressure up to the TPa regime has been reported ([40] and references within) by effectively reducing the culet diameter below 10 µm using focused ion beam (FIB) cutting. To keep the sample in place while increasing the pressure and preventing damage by local stress on the diamond edges during contact of the two anvils, a metallic gasket ring is placed between the culets. Usually, Re with one of the highest K values (350 GPa) in all metals and the highest melting temperature (3500 K at 1 atm) from all elements [41] is used. The gasket with a thickness of 200 to 300 µm is pre-indented between the diamond anvils down to a thickness of 20 to 50 µm, depending on the maximum target pressure. The sample chamber is drilled in the centre of the indention with a diameter of 50 % of the smallest used culet using either pulsed laser ablation or electrical discharge machining (EDM) drilling. A pressure-transmitting medium is loaded in the sample chamber, embedding the sample to prevent strain caused by the uni-axial pressure. The medium has to be soft and highly compressible to allow for quasi-hydrostatic conditions. Commonly used are KCl or NaCl for lower pressures and noble gases such as Ne for high-pressure experiments. For heating experiments, an additional layer of thermal insulation such as KCl between the sample and the diamond anvils, having a high thermal conductivity, can be used.

For the experiments described in this work, a BX90 DAC with a large radial opening (BX90-RD), allowing for measurements in a scattering angle range from 70 to 110° was used. To enable those measurements, the gasket has to undergo another step during preparation, by first flipping the gasket after the first half of the indentation and sanding down the bulk caused by the pre-indention and using asymmetric seats as described by Albers et al. [42]. Additionally, a standard diamond is used upstream to increase further the available angle window for collecting the signal in the 70 to 110° scattering geometry. A Boehler-Almax (BA) diamond is used downstream, to have a larger lateral opening window for XRD measurements as shown in FIG. 2.10. The pressure in the DAC can be determined before and after the experiment, by two well-established ways. If the space in the sample chamber allows for it, a ruby ($Cr:Al_2O_3$) can be loaded near the sample. When excited with a laser, ruby shows a strong luminescence (R1 and R2) between 692 to 696 nm caused by the $^2E - {}^4A_2$ electron transition. With increasing hydrostatic pressure, the decrease of the Cr-O atomic distance in the 6-fold coordinated Cr, causes an increase in the difference between the energy levels, shifting the luminescence lines to higher wavelengths [44].
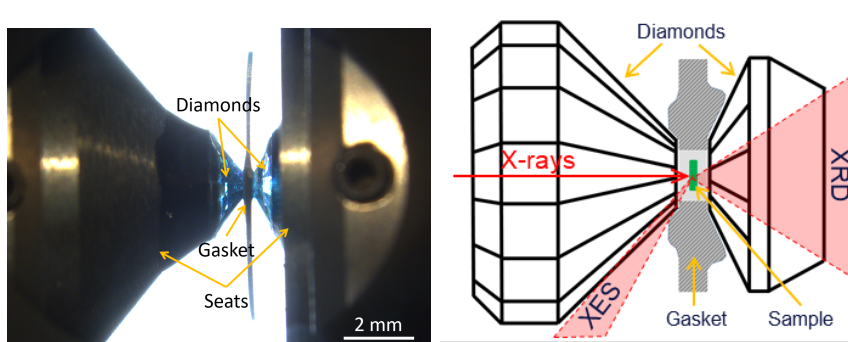
Figure 2.10: DAC setup for combined XRD and XES measurements from a DAC under the microscope [**Left**] showing the diamonds glued to the WC seats and the gasket. The schematics of the measurements [**Right**] show the beam path for XES measurements in near-90° and XRD measurements transmitted through the downstream diamond. Adapted after Kaa et al. [43].

Dewaele et al. [45] suggest the dependence of the pressure p and the high-pressure wavelength λ_R of the R1 luminescence by the equation

$$p = 199.792 \text{ GPa} \left[\left(\frac{\lambda_R}{\lambda_0} \right)^{9.61} - 1 \right], \tag{2.24}$$

with the ambient R1 wavelength λ_0.

The second method to determine the pressure is by measuring the Raman vibrational modes of the diamond anvils. Upon compression, the F_{2g} vibrational motion of the carbon tetrahedron in the diamond lattice shifts from the initial wavenumber value of $1332 \, \text{cm}^{-1}$ to higher values. When the Raman signal is collected through the diamond anvil from the culet under pressure, the resulting derivative of the spectra shows a peak with a shift in the wavenumber $\Delta\nu$ relative to the initial mode ν_0. As suggested by Akahama and Kawamura [46] the pressure can then be calculated by

$$p = 547(11) \text{ GPa} \frac{\Delta\nu}{\nu_0} \left[1 + \frac{1}{2}(3.75(20) - 1)\frac{\Delta\nu}{\nu_0} \right]. \tag{2.25}$$

2.3.1 Pressure and temperature equations-of-state in DIOPTAS

For the quantitative diffraction peak fitting using DIOPTAS from samples at high pT conditions, it is necessary to know the change in volume for compressed and heated samples. For pressure increases at ambient T, DIOPTAS assumes a third-order

Birch-Murnaghan equation-of-state (BM-EOS) [47, 48]:

$$p(V) = 1.5K_{T_0}\left[\left(\frac{V_0}{V}\right)^{7/3} - \left(\frac{V_0}{V}\right)^{5/3}\right]\left[1 + \frac{3}{4}(K'_{T_0} - 4)\left[\frac{V_0}{V})^2/3 - 1\right]\right], \quad (2.26)$$

using the isothermal bulk modulus at $T = 298\,\mathrm{K}$ $K_{T_0}[\mathrm{GPa}]$ and the volume V_0. If K'_{T_0}, the pressure derivative of K_{T_0}, is 4, the EQ. 2.26 becomes the second order BM-EOS, which underestimates the compression of a sample above $1\,\mathrm{GPa}$ as shown by Katsura and Tange [49]. Using the Anderson model [50] and the thermal expansion coefficient α_{T_0}, and the heating-corrections $\delta K_{T_0}/\delta T$, $\delta K'_{T_0}/\delta T$ replacing their ambient values in EQ. 2.26 and $\alpha_T(T) = \alpha_{T_0} + (\delta \alpha_{T_0}/\delta T)\Delta T$, the equation can be extended by the term

$$\Delta p(T) = \alpha_T(T)K_0(T)(T - 298K), \quad (2.27)$$

to combine it to

$$p(V,T) = p(V) - \Delta p(T), \quad (2.28)$$

which is solved by DIOPTAS for *V* for the given pT conditions.

2.3.2 Electronic spin state change under pressure

To understand why most HS 3d metal-bearing phases undergo a transition to a low spin (LS) state during pressure increase and subsequently an LS-HS transition during heating at high pressures, we have to expand FIG. 2.5, which assumes a uniformly distributed negative charge distribution surrounding the ion or a free ion, by the ligand field effects on the 3d electron energy levels. To do this, we have to take the electrostatic effect between the 3d electrons and the negative ligand atom charges into account. For this case, it is sufficient to assume the ligands as negative point charges. The 3d energy degeneracy gets lifted due to the uneven distribution of the 3d orbital and the position of the ligands. Energy states of orbitals closer to the negative ligand charge relatively increase, while those turning away from these charges decrease. FIG. 2.11 shows the shift in energy for a tetrahedral symmetry (e.g. $\varepsilon \mathrm{Fe}_2\mathrm{O}_3$) and octahedral symmetry (e.g. FeS-I).

An HS state is stable if the spin pairing energy exceeds the crystal field splitting energy (Δ_o and Δ_t). For the octahedral case in the pure ionic model, Δ_o is proportional to
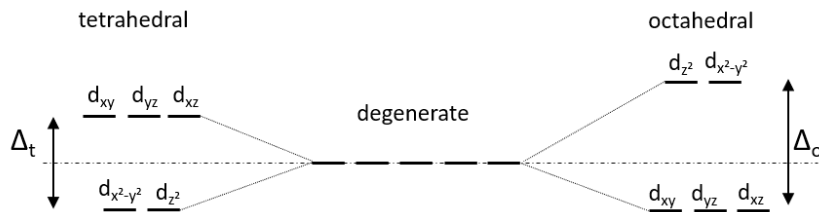
Figure 2.11: 3d orbital crystal field splitting from the degenerate (centre) to a threefold degenerate tetrahedral (left) and twofold degenerate octahedral orientation (right).

Dq which can be calculated after Lever [51]

$$\Delta_o \propto Dq = \frac{e_L^2 r_2^4}{6a_0^5},\tag{2.29}$$

with the negative charge e_L of the ligand, the average radial displacement of the metallic ion 3d electrons r_2, and the metal ion to ligand distance a_0. When the sample is compressed under hydrostatic pressure, a_0 decreases and Δ_o increases, forcing the sample into an LS state when Δ_o becomes greater than the spin pairing energy. With temperature increase, the mean a_0 value increases again, reversing the system back to HS at a certain level.

This crystal field theory (CFT) can be extended to the ligand field theory (LFT) by taking covalent bonding, especially π-bondings, and the different natures of ligands into account, which further decreases the degeneracy of the electronic energy levels, which mostly gains importance for vtc and resonant emission techniques. For this work, the simplified CFT suffices.

2.4 Heating of samples in a DAC

Besides resistive heating, the most common technique to increase the temperature of a non-transparent sample within a DAC is using an (near) infrared [(N)IR] laser or a short wavelength CO_2-laser for transparent samples with a continuous or pulsed beam. With the developments in XFELs and their broader availability for users, isochoric heating by the pulsed and ultra-short X-ray pulses developed a more widespread use. Only recently Meza-Galvez et al. [9] implemented a dedicated experimental station for combining heating with X-ray pulses, more commonly used for plasma research, with a DAC acting as a tamper [9], to heat and probe samples in a static high-pressure environment. Both techniques, laser heating and pulsed X-ray heating, are based on

the absorption through the sample which is described by the Beer-Lambert law for linear absorption

$$\frac{I}{I_0} = e^{-z\mu},\tag{2.30}$$

along z and for a linear absorption coefficient μ. The absorption cross-section $\sigma_a = \mu/\rho_m$, with the mass density ρ_m, shows a value with a order of magnitute 3 lower for a photon energy of $13\,\mathrm{keV}$ compared to a photon energy below $30\,\mathrm{eV}$ [52]. Thus, the absorption and subsequent heating with a (N)IR laser can be approximated as a surface process, while the X-ray heating is a volumetric heating effect. In both cases, the result is excited electrons (valence electrons for (N)IR laser heating and core electrons for X-ray heating for 3d metals) in the sample. As described by Allmen and Blatter [53] there are three steps involved to achieve homogeneous heat from excited electrons:

- Randomisation of motion of excited electrons by electron-electron collision and energy transfer

- Equipartition of the energy between particles and creation of thermal phonons

- Heat flow on a larger scale is based on thermal conductivity.

From a heating source $Q(t) = \rho c_t T(t)$ with density ρ, specific heat capacity c_t and temperature T, we can calculate the heat flux following the Fourier heat conduction equation

$$\rho c_t \frac{\delta T}{\delta t} = \nabla \times (\kappa \nabla T) + Q(t),\tag{2.31}$$

with the heat conductivity κ.

2.4.1 (Near) infrared laser heating

To reduce the longitudinal temperature gradient in the sample, the sample usually requires heating from both sides simultaneously. The lasers can be pulsed to achieve higher temperature stability and peak temperatures [54, 55]. Konôpková et al. [56] and Konôpková et al. [57] conducted finite element (FE) simulation for a pulsed laser ($\lambda = 1072\,\mathrm{nm}$) coupled in a Fe foil. The $7\,\mu\mathrm{m}$ thick sample was contained in a DAC and isolated with a thermal isolation layer consisting of NaCl. Fig. 2.12 shows their result after a longer time period, assuming a near-temperature equilibrium. The increased temperature in the NaCl shows that the temperature profile is driven by heat conduction with temperature peaks at the sample-isolation layer border, where
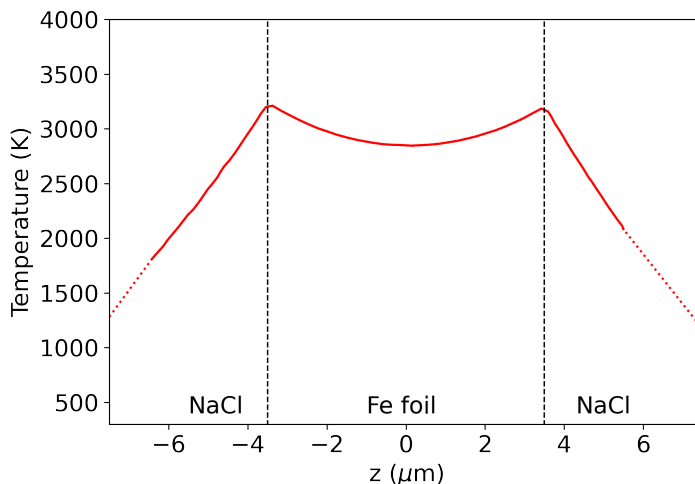
Figure 2.12: FE simulations of the temperature of laser-heated Fe contained in NaCL in a DAC by Konôpková et al. [56]. The temperature gradient within the sample is 11 % at a maximum temperature of 3200 K at the sample surface. The signal was linearly extrapolated for the temperature in NaCl (dashed). Changed after [56, 57].

the up- and downstream laser coupled into the sample. This results in a temperature gradient with a minimum in the centre of the sample. For this case, the gradient in the simulation is roughly 11 % at a maximum temperature of 3200 K. Effects expected during measurements, such as inhomogeneous coupling into the sample or uneven heating power caused by misalignment or a difference in the heating power of both laser spots, that would increase the gradient, need to be taken into account. When XES measurements at high temperatures are conducted at e.g. a synchrotron source, the sample needs to be heated over the duration of the measurement, i.e. several minutes. When there is a steep lateral temperature gradient and the sample consists of a mixture of Fe with lighter elements, thermophoresis (Soret effect) induces a depletion of Fe in the heating spot (see e.g. [58]). This can change the chemistry of the probed sample and therefore the result of the experiment. On the other hand, the long heating times allow for measurements of the heat radiation, which allows for exact temperature measurements using Planck's blackbody radiation.

2.4.2 X-ray pulse heating

When measuring with highly intense femtosecond short X-ray pulses using a tamper (e.g. diamond anvils), the sample will always be heated up within the $10^{-10} - 10^{-9}$ s time scale. FIG. 2.13 shows a simulation for a single X-ray pulse heating a 5 µm thick

Fe foil embedded in LiF in a DAC calculated by Meza-Galvez et al. [9]. After 2 ps the
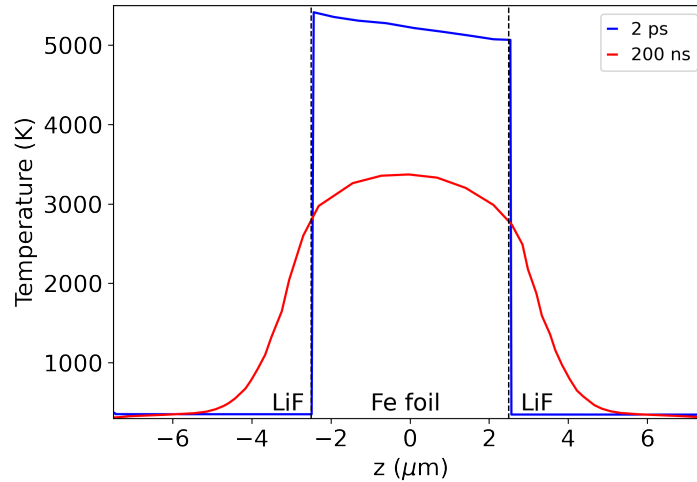
Figure 2.13: FE simulations of the temperature of laser-heated Fe contained in LiF in a DAC by Meza-Galvez et al. [9] for 2 ps (blue) and 200 ns (red) after pulse arrival . The temperature gradient within the sample is 17 % at a maximum temperature of 3370 K and 6 % at a maximum temperature of 5415 K, respectively. Changed after [9]

temperature is the highest on the upstream side with a linear decrease through the sample, caused by the linear decrease of pulse energy due to absorption in the sample. After 200 ns and due to heat conduction, the LiF temperature isolator gets heated as well and a similar but reversed temperature gradient as during laser heating can be seen.

The temperature increase happens after the (quasi-) instantaneous diffraction and emission (1s lifetime in Fe $\Gamma_{Fe} \approx 0.5 * 10^{-15}$ [59]) and will stay elevated up to the 10^{-6} s time scales. When several pulses per train with a repetition rate of MHz are used, the first pulse probes the sample at ambient temperature, while the following pulses probe the heated state, caused by the earlier pulse. This saw-tooth pattern (see FIG. 3.3) evens out with increasing peak temperatures due to an equilibrium between the heating of each new arriving pulse and cooling of the sample in-between pulses [60].

Thus, the sample stays in a hot state only for a small fraction of the run time (roughly $440 \, \mu s \, s^{-1}$ when using 100 pulses at 2.2 MHz). This ultimately decreases the Soret diffusion as shown by Jaisle et al. [61]. Even though the element distribution will stay constant, the phase distribution in the heating spot can change, when there are quenchable phases forming during the heating cycle of a single train. The next arriving train will probe the same start-chemistry, but a different phase distribution.

For more transparent samples with a higher amount of light elements (e.g. $FeCO_3$), the temperature gradient will be smaller because of less absorption, while the coupling in the sample will stay stable. Additionally, there are no alignment problems between the probing X-rays and the heating spot, which might happen during laser heating.

2.5 Additional analytical methods

The methods in this section were applied only to a low extent for this work to further understand the results of the experiments. For the sake of completeness, they are explained briefly. More detailed information about Raman spectroscopy can be found in Lewis and Edwards [62] and for electron microscopy in Egerton [63].

2.5.1 Raman spectroscopy

Raman spectroscopy using a NIR probing laser is commonly used for samples in DACs or recovered from high pressure to identify phases and, as already described in SEC. 2.3, the pressure in the diamond anvils. It is an inelastic two-photon scattering technique, where the incident photons with energy v_L excite the molecules from their vibrational ground state v_0 to a temporary virtual state, which then falls back down to an excited state v_n emitting a photon with the energy $v_L - v_n$, called a Stokes line. On the other hand, if the molecule starts out in an excited state v_n, gets excited into a virtual state and falls back down into the ground state v_0 by emitting a photon, we get an anti-Stokes line with the energy $v_L + v_n$. For the special case where the vibrational energy level of the molecule is the same after the scattering process, it is called Rayleigh scattering with $v_R = v_L$. The Raman signal $\Delta v_n = (1/\lambda_L - 1/\lambda_n)$ is given as wavenumber (cm^{-1}) for the excitation wavelength λ_L and the excited state wavelength λ_n. Stokes and anti-Stokes lines are molecule specific. A molecule shows a signal in the Raman spectrum if it shows a change in its polarizability due to the vibrational modes, for example, the stretching in the O_2 or CO_2 molecule or the F_{2g} bending in the diamond C tetrahedrons at $1332\,cm^{-1}$. The state of higher polarizability e.g. stretched $O-O$ or $C-O$ bonds, represent the virtual higher energy states of the molecule.

To study the *ex-situ* Raman signal of the quenched phases, the samples were measured with a 532 nm laser to collect the Raman spectrum in the range 300 to $1250\,cm^{-1}$. The laser was focused down to a spot size of $4\,\mu m$. The signal was collected using

a LabRAM HR800 VIS Raman spectrometer at Geoforschungs Zentrum (GFZ) Potsdam and at the Institute of Geosciences at the University of Potsdam. To determine the pressure of diamond anvils, we used the offline Raman system at the P02.2 beamline at Petra III [64].

2.5.2 Scanning and transmission electron microscopy

If the sample can be recovered after pressure release, it can be further investigated with electron microscopy by imaging the surface of the sample using scanning electron microscopy or the distribution of the electrons of ultra-thin sample foils by transmission electron microscopy. For both methods, the sample has to be placed in a small vacuum chamber and shot with a high-energy electron beam (PE). The wavelength, enabling a resolving resolution in the nm regime, depends on the accelerating voltage U and can be calculated by

$$\lambda_e = \frac{h}{\sqrt{2m_e e U}}.$$

(2.32)

For a typical voltage $U = 10\,\text{kV}$ the wavelength λ_e is $12.3\,\text{pm}$. The beam is focused using lenses down to the order of tens of nm for scanning electron microscopy (SEM) and in the sub-nm regime for transmission electron microscopy (TEM).

For measurements at the SEM, the sample has to be coated with a thin layer of metal, e.g. Au, to prevent charging artefacts by dumping high amounts of electrons in the sample. The SEM provides two different pieces of information. The sample's topography is analysed by measuring secondary electrons (SE), which are generated by the inelastic scattering from the primary electrons with the outer electrons of the sample. Those SE are low-energy electrons with energies up to $50\,\text{eV}$. Therefore they can only be measured from within $10\,\text{nm}$ depth of the sample and need to be attracted to the detector by a positive charge. The result is that on slopes on the surface of the sample, there are either more or less SE reaching the detector, depending on the position of the detector relative to the slope. This gives a 3D contrast of the surface of the sample. The yield of SE depends, besides others, on the energy of the PE and the atomic number Z, while the latter shows only a small increase with increasing Z. The second information provided by SEM is to measure elastically back-scattered electrons (BSE) to gain element-specific information. BSE are elastically scattered from the atom nucleus. The cross-section is relative $\sigma_{BSE} \sim {}^{Z^2}/_{U_{PE}^2}$, thus at a constant PE beam energy, the BSE yield is strongly increased for heavier elements.

Because the energy of the BSE is higher than those of the SE, the information gained is from larger depths in the sample. SEM measurements were conducted with a Quanta 3D field emission gun SEM.

TEM needs a sample with a thickness of only a few layers of atoms. To achieve that, the sample is first placed in a FIB to cut the TEM lamella from the sample using Ga ions. The resulting sample is then transferred to the TEM, where it is shot with an electron beam perpendicular to the surface of the sample. The transmitted electrons are either elastically or inelastically scattered in the same matter as for SEM measurements or are transmitted without interacting with the sample. For bright-field TEM measurements, the latter electrons with only a slight deflection are collected, yielding information about the space in between atoms. For dark-field TEM measurements scattered electrons at a certain angle are collected, resulting in a direct measurement of the position of atoms. In accordance with SEC. 2.1.1, a 2D area detector can collect the diffracted signal of the electron beam yielding information about the structure, crystallinity and orientation of the sample probed. TEM lamella for this work were cut using a Helios G4 UC DualBeam FIB and measurements were done in a a FEI Tecnai F20X-Twin TEM at GFZ Potsdam.

Energy dispersive X-ray spectroscopy

Samples placed and measured in a SEM can be simultaneously measured using Energy dispersive X-ray spectroscopy (EDX). Due to inelastically scattered electrons from the PE beam, there are interatomic electron transitions to fill the resulting electron vacancies in inner shells. As described in SEC. 2.1.3 these transitions are element specific, which allows to measure the chemistry of the sample. EDX measurements usually are taken in the lower hard X-ray regime and mostly cover K shell emission lines. From the normalised peak intensities of each fluorescence peak, one can calculate the element composition.

3 Proof of principle: X-ray heated iron carbonate at high pressure

In this chapter, the results from the first experiment using a prototype setup at the HED instrument at the European XFEL using a von Hámos spectrometer optimised for easy operability in combination with a DAC are presented. It serves as a test of feasibility for the combination of X-ray heated samples contained in a DAC over several X-ray trains to collect the changes in the X-ray emission as a function of the photon flux, i.e. temperature increase, in the sample. Data were collected for $455\,\mathrm{kHz}$ and $2.2\,\mathrm{MHz}$, testing measurements both at near ambient temperatures and at temperatures above melting temperature. The $FeCO_3$ system was studied in terms of the electronic spin state for Fe, which can be extracted from its Kβ emission data. Simultaneously measured changes in the samples' structure via XRD and FE simulation can be used to estimate temperatures reached at the chosen photon flux. *Ex-situ* analysis using spatial synchrotron XRD and XES measurements, spatially resolved optical Raman measurements and *post-mortem* SEM/TEM add to the full understanding of processes during X-ray heating.

Parts of this chapter were published by Kaa et al. [43]. ©2022 American Physical Society

3.1 The FeCO₃ system at 51 GPa during heating

Siderite ($FeCO_3$) is one of the main carbon-containing candidates in subducted sediments into the Earth's interior and thus an important component to the understanding of the carbon cycle within the Earth [65]. It has been extensively researched at high pressures and temperatures in the past decade. Therefore, we have a broad understanding of its stability, i.e. structural changes, decomposition and melting, at conditions up to the lower mantle as well as its electronic configuration [66, 67, 68, 69, 70]. At ambient temperature and with increasing pressures up to roughly $42\,\mathrm{GPa}$ the volume decrease of siderite in the trigonal $\overline{R}3c$ crystal symmetry is mostly driven by

compression along the c-axis [71]. The subsequent close-to isotropic volume collapse of 10 %, also connected to a change of the absorption bands from the near-infrared to the visible regime [72], is caused by a change from unpaired electrons to paired electrons in the 3d orbital of Fe, i.e. an LS-HS transition [73] which is completed above 45 GPa. Above this threshold and when pressurised further, $FeCO_3$ stays stable in this symmetry at pressures above 100 GPa [69]. This pressure-induced HS-LS transition is reversible by decreasing the pressure below 42 GPa. Up to roughly 58 GPa a full HS can also be achieved by heating the sample above 500 to 1500 K, reversing the volume collapse (see FIG. 3.1). When heated at pressures above 58 GPa, $FeCO_3$ will decompose into iron-oxides and more complex phases such as the orthocarbonate $Fe_4C_3O_{12}$ (siderite-II) and tetrahedral carbonate $Fe_4C_4O_{13}$ [69, 42] hosting HS-Fe respectively [42]. Liu, Lin, and Prakapenka [74] suggest that $Fe_4C_3O_{12}$ has a stability field at pressure above 49 GPa and temperatures above 1200 K where it coexists with $FeCO_3$. At a pressure of 51 GPa the LS state can be reversed by heating $FeCO_3$ above 1000 K [75]. Incongruent melting of HS-$FeCO_3$ [69] producing Fe_xO_x in varying stoichiometry and C containing phases such as diamond or CO_2 will begin above 1800 K.
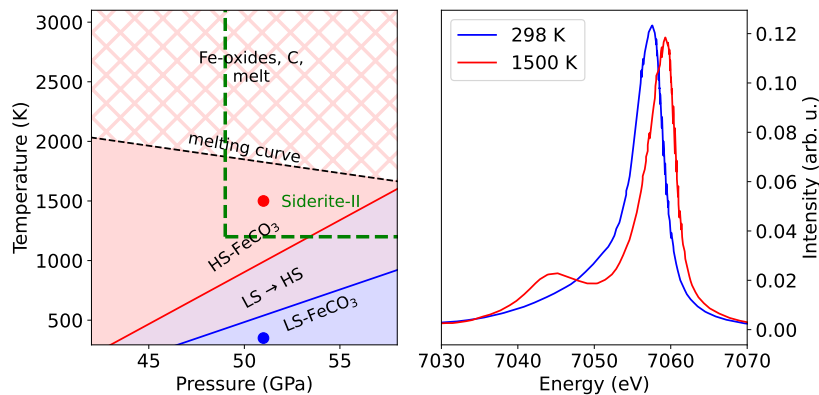
Figure 3.1: [**Left**] Phase diagram for $FeCO_3$ for pressures between 40 to 60 GPa and temperatures between 298 to 3100 K. Stability fields for LS- and HS-$FeCO_3$ are shown. Temperatures for incongruent melting are marked (black dashed line). Regions of LS Fe (blue), spin state changes (purple) and HS regions (red) are marked. The HS region above the melting curve (red hatched) is suggested by Kaa et al. [43]. Modified after Cerantola et al. [69]. Conditions under which orthorhombic siderite-II ($Fe_4C_3O_{12}$) coexists with $FeCO_3$, as suggested by Liu, Lin, and Prakapenka [74] becomes stable is marked in green. Pressure and temperature conditions for measurements of $FeCO_3$ by Weis et al. [75] [**Right**] are given for LS state (blue) and HS state (red).

The main objective of this experiment was to test the overall compatibility of combining X-ray heated DACs with longer exposure times necessary for XES measurements.

This was tested by inducing the heating-driven spin state change in the $FeCO_3$ system at high pressures.

3.2 Experimental and beam setup

The DAC was prepared as described in SEC 2.3. The pure $FeCO_3$ powder was synthesised by Cerantola et al. [69] and loaded as a pressed pellet with a diameter of $50\,\mu m$ into a $120\,\mu m$ hole drilled into the Re gasket. A ruby was placed beside the $FeCO_3$ pellet for pressure determination (see SEC 2.3). To reach a pressure of $51 \pm 1\,GPa$ diamonds with a culet diameter of $300\,\mu m$ were used. Ne was gas-loaded before closing the DAC to act as a pressure-transmitting medium and, to some extent, as a thermal insulator. No additional thermal insulator, such as KCl, between the diamond anvils and the sample was loaded.

The experiment was conducted in the vacuum chamber IC1 at pressures below $1 \times 10^{-5}\,mbar$ to reduce the air scattering signal on the detectors. Thus, the setup for this experiment was optimized for usability and low error susceptibility by reducing degrees of movement for the detector, the analyzer crystal and the DAC holder. A single cylindrically bent Si(531) analyser crystal with a bending radius of $250\,mm$ and a surface size of $110\,mm \times 30\,mm$ (H x V) was placed in a horizontal $100°$ scattering angle, reducing the background signal due to reduced unwanted scattering on the e.g. diamond anvils, with a distance of $250\,mm$ to the sample-detector axis, fulfilling the von Hámos geometry. The pitch and yaw were controlled by piezo-driven rotation stages. The height and crystal-sample distance could be slightly corrected using motorized linear stages. The crystal was positioned to utilize a Bragg-angle of $72°$, allowing for measurements between 7000 to $7120\,eV$. The crystal covers a horizontal solid angle of $0.433\,rad$, thus collecting roughly $^{(49.90\times10^{-6}\times433\times10^{-3})sr}/_{4\pi sr \times 0.192\,eV} = 8.96 \times 10^{-6}\frac{1}{eV}$ photons emitted in 4π (see SEC. 4.3 and [29]). The ePix100 detector [76, 77] with a pixel size of $50\,\mu m \times 50\,\mu m$ and a sensor size of $45\,mm \times 45\,mm$ was mounted on the vertical breadboard of IC1 on a stage roughly $160\,mm$ above the sample to collect the emitted signal. The detector sensor was placed directly above the sample position. The BX90-RD DAC was placed on a fixed holder on the Hexapod positioning system. Additionally, a second ePix100 detector was placed in transmission covering a scattering angle (2θ) of 11 to $30°$ to simultaneously measure the XRD signal. The setup can be seen in FIG 3.2. The XES detector was calibrated using a free-standing Fe foil on the sample position. To calibrate the XRD detector, a CeO_2 powder reference sample put in between Kapton

foil was measured at the sample position.

The X-ray beam was operated at SASE mode at a mean photon energy of 13 keV with pulse energies between 700 to 800 µJ, not including the beamline transmission. Each pulse train contained 10 pulses at either 455 kHz (time gap of 2.2 µs) or 2.2 MHz (time gap of 455 ns). The beam size was focused down to 20 µm × 20 µm (H x V, FWHM) on the target. The pulse energy upstream of the focussing optics was measured in an absolutely calibrated XGM. The intensity during the experiment was changed by using various sets of solid attenuators and was set between 51.9 to 255.2 µJ. We heated the sample over several minutes per run, accumulating over several heating cycles within each train. The pulse energy was increased on the same spot. Information on the pulse energy of SASE2 and HED as well as the number of trains accumulated for each run can be found in TAB S1.

XES and XRD data were obtained at 10 Hz and were treated as described in SEC. 2.1.1 and SEC. 2.1.3.
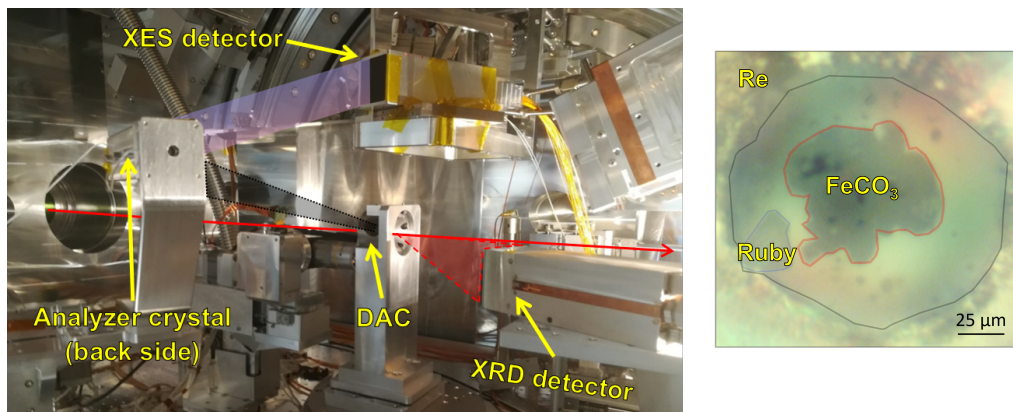
Figure 3.2: [**Left**] A picture inside IC1 of the setup for the $FeCO_3$ experiment. The DAC was placed in a single DAC holder on the Hexapod. The single Si(531) analyzer crystal is seen from the back and positioned to utilize a 72° Bragg angle. Above the sample, the ePix100 detector for the XES measurements was placed to collect the emitted signal. An additional ePix100 detector was placed in the transmission of the sample to collect the elastically scattered XRD signal. [**Right**] A picture taken with a microscope of the sample chamber within the Re gasket (grey). The ruby (blue) and the $FeCO_3$ (red) are marked. The sample, analyser crystal and detector is positioned in the von Hámos geometry. Changed after Kaa et al. [43].

3.3 Finite element - simulation

TAB 3.1 shows the thermodynamic properties for $FeCO_3$ and diamond assumed for the finite element (FE) simulation for the temperature using COMSOL [1]. The temperature development within each train was calculated for a sample absorption of 5 µJ at 455 kHz and 15 µJ at 2.2 MHz for a 20 µm (H x V, FWHM) beam with a Gaussian shape. Assuming a beamline transmission after the XGM in XTD 6 of 0.5 for the optical components, a transmission of 0.45 for the 2.3 mm thick diamond in upstream and a sample absorption of 0.25 for 20 µm thick $FeCO_3$ [22], only 5.6 % of the incident pulse energy is absorbed by the sample. Thus, the calculations respond to pulse energies in the XGM of roughly 90 µJ and 268 µJ and are comparable to the runs with the highest photon energy for both 455 kHz and 2.2 MHz.

	d	c_t	κ	δ
$FeCO_3$[78, 79, 80]	30	70	25	5000
Diamond[9]	2500	630	1500	3520

Table 3.1: Properties of $FeCO_3$ in LS state at 50 GPa and for diamond anvils. Thickness d in [µm], specific heat capacity c_t in [$J\,mol^{-1}\,K^{-1}$], thermal conductivity κ in [$W\,m^{-1}\,K^{-1}$] and density δ in [$kg\,m^{-3}$]. Adapted after Kaa et al. [43]. ©2022 American Physical Society.

FIG 3.3 shows the temperature development within each train. With each arriving pulse, the sample gets probed quasi-immediately before a heating spike and partial cooling before the next arriving pulse. At 455 kHz despite longer time gaps between pulses, the sample heats up to a maximum of 700 K and gets probed at a maximum of 500 K, which is on the lower border of the LS-HS transition. While at 2.2 MHz due to shorter gaps, i.e. more efficient heating, the temperatures reach a maximum of 3000 K and the sample gets measured at a maximum of 2500 K with 6 pulses measuring above melting temperature. The temperature taken from 10 µm off-axis has an equivalent evolution with temperatures up to 500 K below the central temperature, causing a temperature gradient in the signal of the probed sample.

---

[1]Simulations were conducted by Dr. Z. Konôpková [43]
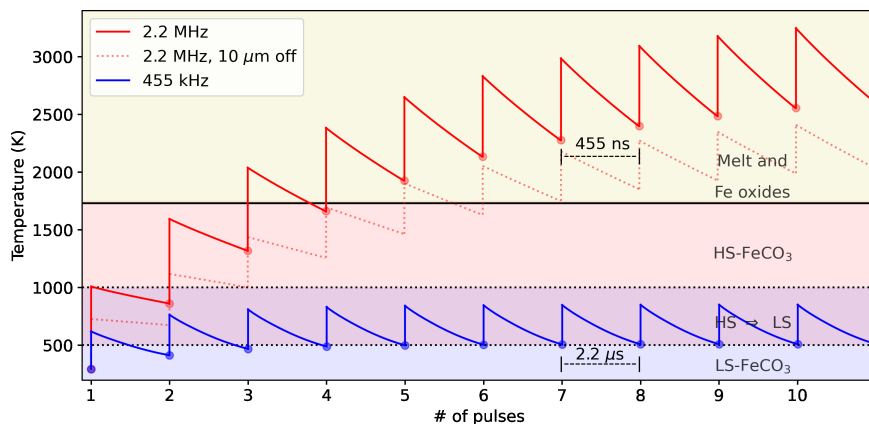
Figure 3.3: FE-simulation using Comsol for $FeCO_3$ at $455\,kHz$ (blue) and $2.2\,MHz$ (red) in the center (full) and $10\,\mu m$ off axis (dotted), assuming $5\,\mu J$ and $15\,\mu J$ sample absorption, respectively. (For phase boundary temperatures see FIG 3.1). Dots show when the sample gets probed quasi-instantaneously. Changed after Kaa et al. [43].

3.4 In-situ results

3.4.1 X-ray emission spectroscopy - Fe Kβ during heating

For testing the setup, the emission signal for the Kβ line for the free-standing Fe foil was measured at a pulse repetition rate of $455\,kHz$ for quasi-non-heating measurements (see FIG 3.4). The achieved focus of the emission line on the detector had a maximum horizontal width of 28 pixel or $1.4\,mm$ due to a lack of degree of freedom for the detector positioning, thus subsequent limited focusing possibilities. Using the K$\beta_{1,3}$ main peak position and the vtc peak, we calibrated the energy scale assuming a constant energy dispersion over the energy window by fitting the measured signal to a high-resolution reference by Hölzer et al. [81]. The resulting energy dispersion is $0.23\,eV/pixel$. When comparing the FWHM of the K$\beta_{1,3}$ signal for the measured foil ($5.50\,eV$) to the FWHM of the high-resolution reference ($3.53\,eV$) the instrumental broadening can be calculated to a value of $4.22\,eV$, assuming a Gaussian distribution, while the expected and optimal broadening for a perfect crystal in von Hámos geometry would be in the sub-eV regime [29]. This broadening is due to the insufficient focus of the signal on the detector.

Data taken on the $FeCO_3$ sample is shown in FIG 3.5 for close-to-ambient temperatures ($455\,kHz$ pulse repetition rate) and runs with heated sample ($2.2\,MHz$ pulse repetition rate). At $455\,kHz$ repetition rate and with a pulse energy of $78.4\,\mu J$ the
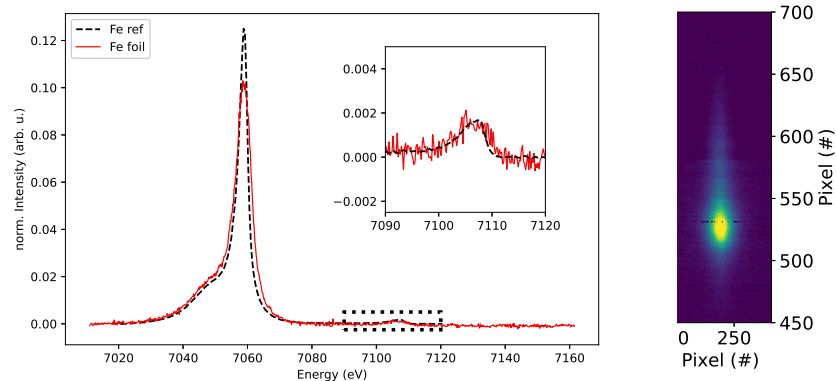
Figure 3.4: [**Left**] Kβ emission line of a free-standing Fe foil (red) including the vtc signal (cropped). A high-resolution reference signal from Hölzer et al. [81] is shown (black, dashed). [**Right**] The detector image of the Kβ emission signal.

heating was sufficient to introduce a slight change from an LS state to mixed spin states, suggesting temperatures above $450\,\mathrm{K}$ (FIG 3.1), as seen in the slight shift of the K$\beta_{1,3}$ main peak to higher energies relative to the $51.9\,\mathrm{\mu J}$ run. Subsequently, only the run taken with $51.9\,\mathrm{\mu J}$ can be used as an LS state reference to calculate the difference to each spectrum for calculating the corresponding IAD values as confirmed by XRD (see SUBSEC. 3.4.2).

Data taken with $2.2\,\mathrm{MHz}$ shows an energy shift, as expected, at lower pulse energies due to more efficient heating at higher repetition rates. The peak shift becomes more apparent in the difference to the $455\,\mathrm{kHz}$ LS state reference. The first changes can be seen at $18.0\,\mathrm{\mu J}$. The energy shift increases with increasing pulse energy and reaches a plateau above $51.7\,\mathrm{\mu J}$. When compared to HS references (see FIG 3.1) it becomes clear, that even at $255.0\,\mathrm{\mu J}$ a complete HS state has not been achieved yet, but it maxes out at an estimated $45\,\%$ HS when compared to a linear combination of LS and HS state references by Weis et al. [82] (see FIG 3.5). Due to the high noise data, the spin state can not be calculated by the IAD value but can be estimated by the M1-shift of the K$\beta_{1,3}$ peak, which reaches a maximum of $0.7\,\mathrm{eV}$, which corresponds to an HS fraction of $43\,\%$ compared to the references reported in Weis et al. [75] (see FIG 3.12).

Due to the low efficiency of the spectrometer and the relatively low pulse energies needed for this experiment an analysis of the vtc signal is not possible. The SNR at the highest photon flux has a value of 9, which is well below the suggested SNR value of 100 by [30] to be able to analyse the vtc signal of Fe. Therefore, the vtc will not be taken into account further for *in-situ* data of the FeCO$_3$ sample.
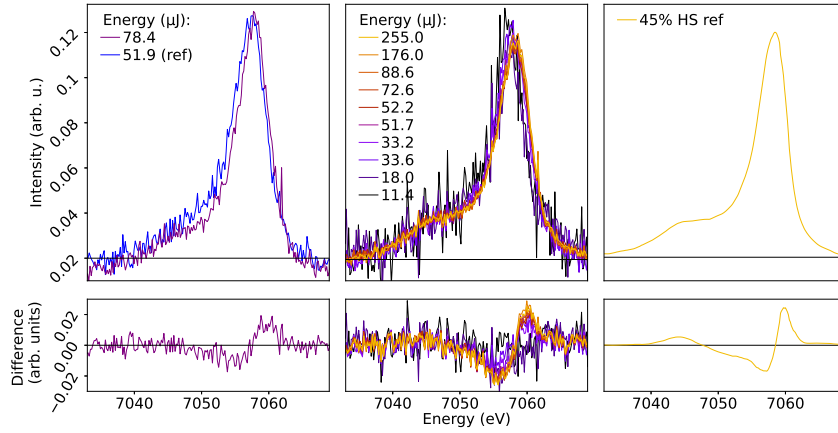
Figure 3.5: [**Left**] Near-ambient temperature runs at $455\,\text{kHz}$ for $51.9\,\mu\text{J}$ and $78.4\,\mu\text{J}$. [**Center**] High temperature runs at $2.2\,\text{MHz}$ up to $255.0\,\mu\text{J}$. There is a clear shift in energy for the $K\beta_{1,3}$ main peak and a slight increase in the $K\beta'$ shoulder visible. For both graphs, the difference to the LS state reference at $455\,\text{kHz}$ with $51.9\,\mu\text{J}$ is shown on the bottom. [**Right**] LS and HS state reference by Weis et al. [82] combined to a intermediate state spectrum containing $45\,\%$ HS state. Changed after Kaa et al. [43].

3.4.2 X-ray diffraction

The *in-situ* XRD data shown in FIG 3.6 contain information about phase distribution including melting, allowing for an estimation of the temperature, and the volume changes in $FeCO_3$ caused by the electronic spin state change, thus the HS fraction of Fe in $FeCO_3$. The starting phase of the runs at $455\,\text{kHz}$ repetition rate and runs at low pulse energy and $2.2\,\text{MHz}$ repetition rate was siderite [71, 83] in its LS state. With increasing pulse energy the volume expansion and a second set of diffraction peaks at lower 2θ angles start to appear. This can not only be seen at $2.2\,\text{MHz}$ but also at $455\,\text{kHz}$, as the pulse energy was already sufficient to heat the sample and induce a slight increase in the HS fraction in $FeCO_3$ (see SUBSEC 3.4.1). The LS-HS ratio increases with rising photon flux. Additionally, while increasing the photon flux, diffraction peaks of orthorhombic $Fe_4C_3O_{12}$ [69] appear. At the same pulse energies, a broad contribution to the signal from 2.1 to $2.9\,\text{Å}^{-1}$ underlying remaining diffraction peaks can be found. There are no clear peaks that hint towards Fe oxides as suggested by earlier studies (e.g. [70] and references within), which might be due to overlaying of peaks of those phases with the complex $Fe_4C_3O_{12}$ signal, especially in the 2.3 to $2.8\,\text{Å}^{-1}$ range, where the allocation of some diffraction peaks remains unclear. When increasing the pulse energy further to $144.4\,\mu\text{J}$ the contribution of the melting signal becomes more dominant and a single peak of CO_2-V [84] is found. De-

spite a clear and dominant melting contribution at $255.0\,\mu J$, a non-negligible fraction of cold and LS $FeCO_3$ remains visible in the diffraction data. while the signal of hot HS $FeCO_3$ decreases above $50\,\mu J$ when signs of melting and $Fe_4C_3O_{12}$ start to appear.
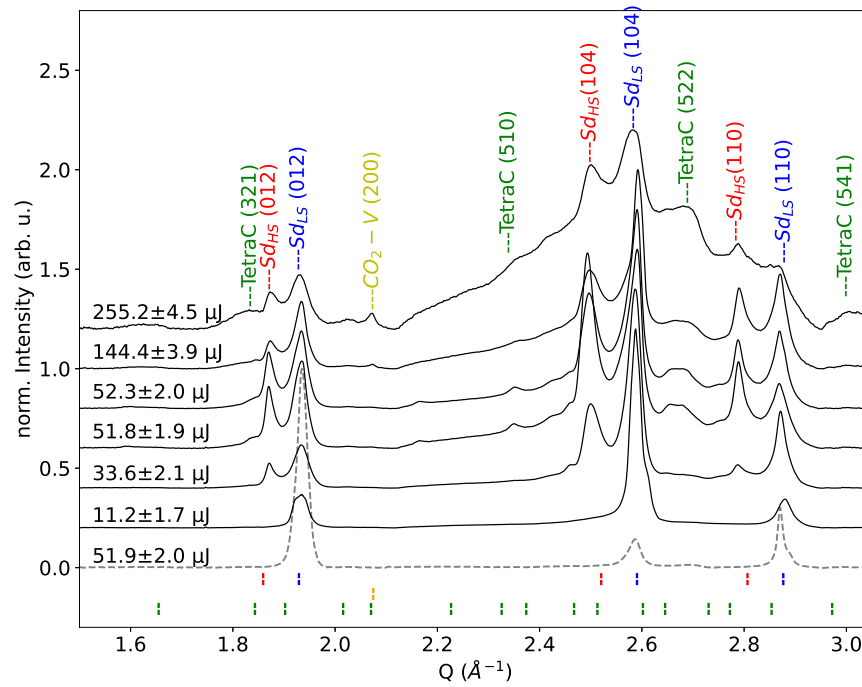
Figure 3.6: *In-situ* XRD pattern for specific pulse energies at $455\,kHz$ (dashed) and $2.2\,MHz$ showing the development of phases during heating in the $FeCO_3$ sample up to melting. Found phases are LS- and HS-siderite (Sd_{LS} (blue), Sd_{HS} (red)), orthorhombic Tetracarbonate (TetraC, green), CO_2-V (yellow) and melt. Patterns are normalized to the maximum peak value. Adapted after Kaa et al. [43]. ©2022 American Physical Society.

Figure 3.7 shows the peak splitting for the $FeCO_3$ (013) diffraction peak separately as the sample switches into HS. The splitting suggests a volume expansion from $209.4\,\text{Å}^3$ to $231.8\,\text{Å}^3$ using the EOS of Litasov et al. [83], confirming an volume increase of roughly $10\,\%$ described by Lavina et al. [66]. At $455\,kHz$ and $78.4\,\mu J$ the sample has a HS fraction of below $10\,\%$. The diffraction peak of the LS $FeCO_3$ shows a shift to lower values between $51.9\,\mu J$ and $78.4\,\mu J$, suggesting heating of $200\,K$. When all three sets of siderite diffraction peaks are taken into account, we can evaluate the fraction of HS siderite probed during each run. At $2.2\,MHz$ the HS fraction reaches its maximum at $71.8\,\mu J$ with a fraction between 45 to $50\,\%$, taking the three sets of diffraction peaks into account (see FIG 3.7). Between 33 to $34\,\mu J$ the HS fractions show inconsistencies, assuming constant heating of the sample at constant photon

flux, ranging between 25 to 40 % (see FIG 3.12).
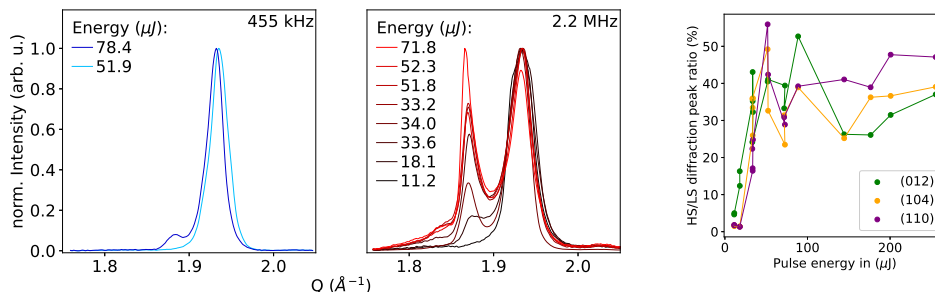
Figure 3.7: Seperated *in-situ* XRD peaks for FeCO$_3$ (012) for ambient 455 kHz [**Left**] and strongly heated 2.2 MHz [**Center**] runs for increasing photon flux, i.e. peak temperatures. The ratios of the diffraction peaks for the HS/LS-state volume for the siderite (012), (104) and (110) peak pairs are plotted [**Right**]. (Changed after Kaa et al. [43].

3.5 Ex-situ analysis

After the experiment, the sample was temperature quenched by blocking the X-ray beam after the last run. The sample had to undergo several *ex-situ* and, after opening the DAC and recovering the sample, *post-mortem* analysis, to fully understand data taken *in-situ*.

3.5.1 Quenched phases - X-ray diffraction and Raman spectroscopy

For a full understanding of phases and their distribution during heating, the sample was spatially measured using XRD at beamline P02.2 at PETRA III. The 31×31 grid has a step size of $2\,\mu m \times 2\,\mu m$ using a $2\,\mu m \times 2\,\mu m$ beam size (FWHM, H x V). At each position, the sample was rotated by $\Omega = \pm 5°$ relative to the beam for an exposure time of $30\,s$ to increase the diffraction signal of potentially single crystalline phases. $Fe_4C_3O_{12}$, CO_2-V and most iron oxides, as well as melt are quenchable and are therefore detectable after cooling the sample. An example diffraction pattern for the unheated sample and from the centre of the heating spot is shown in FIG 3.8. By plotting the intensity of single peaks belonging to specific phases for each pattern, we can track the relative abundance of those phases. The heating spot appears as a ring of $Fe_4C_3O_{12}$ with a diameter of $20\,\mu m$ with CO_2-V signal in the centre. The

intensity of the $FeCO_3$ peaks is lower compared to the unheated pattern. Due to the number of diffraction peaks especially of $Fe_4C_3O_{12}$, iron oxides can not be clearly identified due to the overlapping of diffraction peaks. The difference between a linear background and a Gaussian background can be taken as an estimation of increased amorphous signal and thus solidified melt. This plot is shown in FIG S1. However, also here the number of peaks of other phases in the heated area and subsequently elevated baseline can falsify this result.
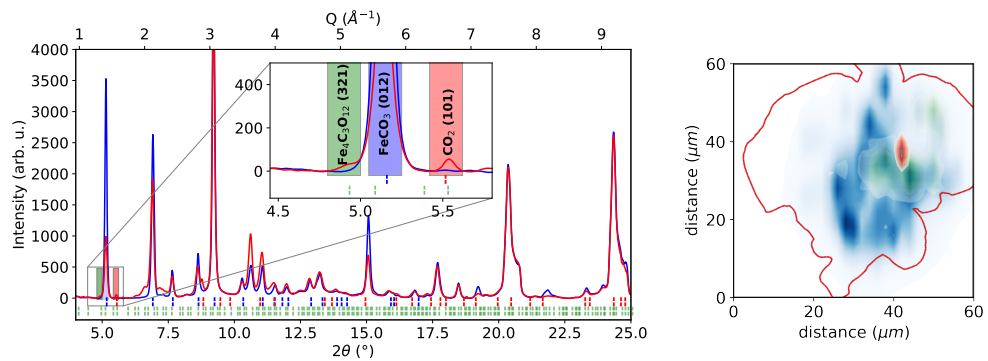
Figure 3.8: [**Left**] Example XRD pattern of the quenched sample for unheated sample (blue) and from the heating spot (red). Diffraction peaks for $FeCO_3$ (blue), CO_2-V (red) and $Fe_4C_3O_{12}$ (green) are shown. The 2θ range for plotting peak intensities is marked in the same colours. [**Right**] The sample borders from FIG 3.2 are marked in red. The distribution of the three phases is marked in their according colours. Changed after Kaa et al. [43].

The appearance order of phases along the heating gradient from the outer parts of the heating spot to the inner part are LS-$FeCO_3$ →$Fe_4C_3O_{12}$ →CO_2-V and melt. This is in good agreement with the appearance of the phases during heating (LS-$FeCO_3$ →(HS-$FeCO_3$) →$Fe_4C_3O_{12}$ →CO_2-V and melt).

Additionally $FeCO_3$ and CO_2-V are Raman active phases [85, 86]. Hence, we spatially measured the sample at high pressure using a LabRAM HR800 VIS Raman spectrometer utilizing a 532 nm laser. Spectra between 300 to 1200 cm^{-1} were measured on a 13×14 grid with a step size of 4 µm × 4 µm, laser beam focus of 4 µm × 4 µm and an exposure time of 1 min per spot. FIG 3.9 shows example Raman spectra, showing siderite and CO_2-V and a similar phase distribution as in FIG 3.8 with a decrease of $FeCO_3$ signal and the appearance of CO_2-V in the heating spot. $Fe_4C_3O_{12}$ shows no Raman modes as already stated by Albers et al. [42] and there is no signal of $Fe_4C_4O_{13}$, which crystallises from $Fe_4C_3O_{12}$ at higher temperatures and pressures. Between 300 to 500 cm^{-1} and 700 to 950 cm^{-1} there are two broad and low-intense

peaks resembling signal from amorphous graphite [87], which rather origins from the diamond anvils than carbon from the $FeCO_3$ sample and might have been caused by radiation damage of the diamonds. Thus, the amorphous graphite is not measured in the Raman laser focus, but as a side product while shooting the beam through the upstream anvil, explaining the low intensity. There are no Raman peaks of Fe-oxides such as Fe_2O_3 [88].

3.5.2 Spatially resolved X-ray emission spectrscopy

Even though temperature-induced HS-$FeCO_3$ is not stable when the sample is quenched, Fe in the various other phases can be present in an HS or combined spin state in the quenched sample. Thus, to understand the variation in the *in-situ* spin state measurement, a potential HS fraction in the other phases must be identified. This was done by measuring the spatial Fe Kβ emission distribution at P01 at PETRA III using a portable von Hámos setup, described by Albers et al. [89]. The 6×6 grid has a step size of $8\,\mu m \times 8\,\mu m$. The beam size was set to $8\,\mu m \times 8\,\mu m$ (FWHM, H x V) and each spot was measured for $5\,min$. Low-quality data measured at the edge of the sample was filtered out.

FIG 3.10 shows an XES spectra of non-heated sample and from the centre of the heating spot. The non-heated $FeCO_3$ shows a complete LS, while the heated sample is in a higher spin state with an IAD value of 0.29 ± 0.05 and an M1 shift of $0.92\,eV$,
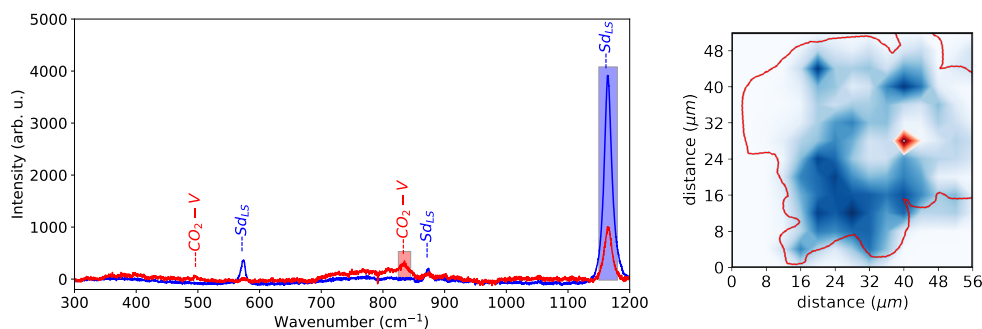
Figure 3.9: [**Left**] Example Raman pattern of non-heated siderite (blue) and taken from the heating spot (red). Raman modes for LS-siderite are marked in blue and for CO_2-V in red. Within the heating spot, we see a decrease in the intensity of siderite modes. Low intense and broad peaks from 300 to $500\,cm^{-1}$ and 700 to $950\,cm^{-1}$ show graphite. In the intensity distribution [**Right**] it becomes clear, that CO_2-V only appears in the heating spot. The sample border is marked in red. Changed after Kaa et al. [43].

corresponding to a spin state of 1.18 ± 0.10. The difference in the $K\beta_{2,5}$ signal shows a change in the valence and/or electronic structure of the iron measured.
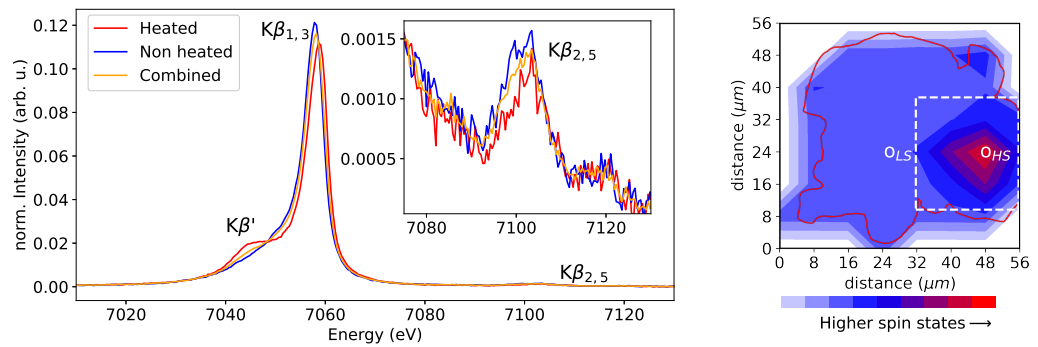
Figure 3.10: [**Left**] Example Fe $K\beta$ emission including the vtc signal for non-heated (blue) and heated sample (red) and a combination of both (orange). The inlay shows the vtc region zoomed in. [**Right**] IAD distribution of the sample showing an LS state (blue) values for unheated $FeCO_3$ and HS state (red) for the centre of the heating spot. The position of the example spectra (white, circle) and the area over which spectra were combined is shown (white, dashed). Changed after Kaa et al. [43].

When all spectra from the heating spot are summed up, we can estimate the spin state in an area $24\,\mu m \times 24\,\mu m$ and thus roughly the probed area by the X-ray beam at HED. The IAD value of this area is 0.08 ± 0.01 with an M1 shift of $0.31\,eV$ which corresponds to a quenched spin value of 0.36, which is above the spin state of 0 for ambient temperature $FeCO_3$. This suggests that the temperature-quenched Fe containing phases are in an HS state.

3.5.3 Electron microscopy

After recovering as many sample grains as possible by releasing the pressure and opening the DAC, they were transferred to a Quanta 3D field emission gun scanning electron microscope. On grains, which show melting and degassing structures, EDX analysis was performed. Two of the grains were cut into TEM foils using the Helios G4 UC DualBeam FIB and were transferred to a FEI Tecnai F20X-Twin TEM for further phase identification using ED.

The sample grain resembles a conglomerate of idiomorphic siderite crystals with a grain size of $5\,\mu m$ as seen in FIG 3.11. The sample has a solidified melt structure on the surface. The idiomorphic character becomes only evident in the profile cut in

the TEM lamella. Additionally, we can see large gaps, likely formed by gas bubbles during CO_2 accumulation in the melting process during the experiment. Based on this information, we can assume that HED11 originates near the heating centre. TEM pictures seen in FIG S2 show bubble-like features in the crystal lattice. ED measurements show that the inner porous crystals are made of Hematite (α-Fe_2O_3) [2]. We can assume that the depletion of carbon is due to the out-gassing of CO_2 during pressure release.
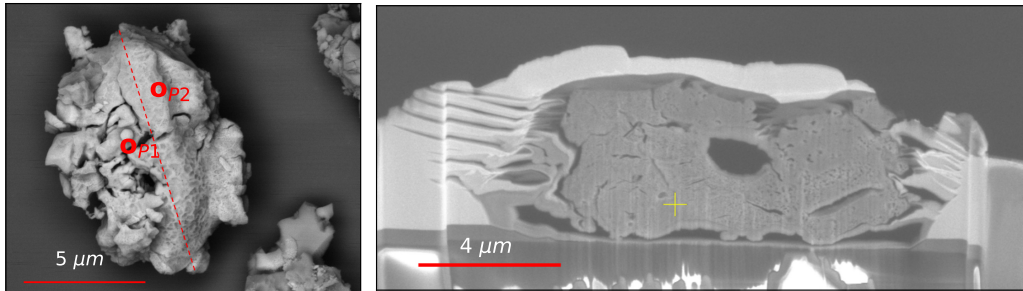
Figure 3.11: [**Left**] HED11 grain, melted together with the strong melting structure on the surface. P1 and P2 mark spots for EDX measurements (TAB 3.2) The TEM lamella [**Right**] was cut along the red, dashed line. In the profile, large round gaps, likely produced by outgassing between the crystals can be seen. Changed after Kaa et al. [43]. ©2022 American Physical Society.

The chemical composition shown in TAB 3.2 shows a near-$FeCO_3$ composition ($20\,\mathrm{mol}-\%$ Fe, $20\,\mathrm{mol}-\%$ C, $60\,\mathrm{mol}-\%$ O) for P2, while P1 is closer to the composition of $Fe_4C_3O_{12}$ ($21.0\,\mathrm{mol}-\%$ Fe, $15.8\,\mathrm{mol}-\%$ C, $63.2\,\mathrm{mol}-\%$ O). This is in line with the earlier results, confirming the position of the sample grain in the inner parts of the heating spot.

(mol.-%)	Fe	C	O	$\sum$
HED11 - P1	18.8	15.3	65.0	99.1
HED11 - P2	19.6	22.4	57.6	99.5

Table 3.2: EDX measurements for HED11 in FIG 3.11 in mol.-% for spot P1 and P2. The error is between 5 to 10 %.

We assume that P1 stems from the non-heated sample, P2 from the heated, but not molten, sample and the ED measurements from an area which was completely molten.

---

[2]Dr. V. Roddatis; private communication

3.6 Interpretation and Conclusion

The combined data of the $FeCO_3$ system shows a more complex phase relation when multiple heating circles with increasing peak temperatures are applied. While we also probe over a large temperature gradient at 2.2 MHz within each train, e.g. 298 to 2500 K at 255 µJ (see FIG 3.3), the interpretation of the data becomes more difficult with increasing pulse energy. Accordingly, we separate the discussion of the *in-situ* results into three parts. Runs below 50 µJ, between 50 to 144 µJ and above 144 µJ. FIG 3.12 shows the electronic spin state taken from the XES data, by determining the M1-energy shift (light blue) and by fitting reference spectra (dark blue), and from the diffraction peak splitting of $FeCO_3$ (red).
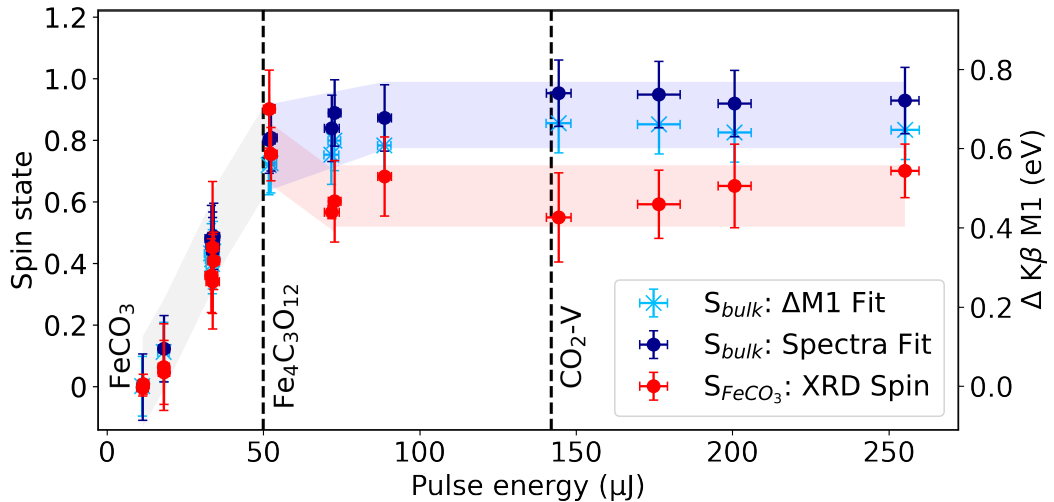
Figure 3.12: Spin state data taken from 2.2 MHz runs as a function of the pulse energy. M1 shift (light blue) and fitted references from Weis et al. [75] (dark blue) were taken from the $K\beta$ emission line. The HS fraction of $FeCO_3$ calculated from the diffraction peak splitting (red) is taken from the XRD data. Pure $FeCO_3$ sample, decomposition into $Fe_4C_3O_{12}$ and melting under CO_2-V crystalisation are marked (black, dashed). Transparent stripes serve to illustrate the trend lines. Changed after Kaa et al. [43]. ©2022 American Physical Society.

Below 50 µJ the probed sample consists of pure $FeCO_3$. Each X-ray train probes over the reversible temperature-induced spin state change, while not inducing any non-reversible changes in the sample, suggesting peak temperatures below 1200 K. Consequently, both spin states, obtained from XES and XRD data, are in very good agreement, showing a linear increase with rising pulse energies. The measured spin state reaches a maximum at a value of 0.75 ± 0.05, which corresponds to an HS fraction below 40 % assuming pure Fe^{2+}. This low amount of HS can be explained

in two ways. The Gaussian beam shape causes a temperature gradient perpendicular to the beam of up to several $100\,\text{K}$ (see FIG 3.3 and [90]). Thus, not all of the $FeCO_3$ within the beam spot gets heated above the spin change temperatures but were probed with beam tails while being relatively cold. Also, the heating spikes and the cooling after and before each pulse, cause peak temperatures to rise above the decomposition temperature before the probing temperatures reach $1000\,\text{K}$, where $FeCO_3$ would be in full HS.

Between 50 to $144\,\text{µJ}$ the spin state obtained from the XES signal, probing Fe in all Fe containing phases, and the HS fraction of $FeCO_3$ start to differ. The maximum spin state for both methods is achieved at $51\,\text{µJ}$ with a spin state of 0.8 ± 0.1. If we assume, that we are at high enough temperatures, to induce a complete HS state in $FeCO_3$, then that would mean that we only probe $40\,\%$ hot sample and $60\,\%$ relatively cold sample. With increasing pulse energy, Fe stays at a constant spin state of 0.85 ± 0.05 while the HS fraction of $FeCO_3$ obtained from the XRD signal slightly decreases. The appearance of $Fe_4C_3O_{12}$ in the diffraction signal suggests that (hot) $HS\text{-}FeCO_3$ decomposes into $Fe_4C_3O_{12}$. To balance the equation of decomposing $FeCO_3$ into $Fe_4C_3O_{12}$, it must also produce a pure C-containing phase such as diamond, which is difficult to detect in the DAC. This phase-change is not reversible and thus increases the relative abundance of (cold) $LS\text{-}FeCO_3$ probed with the X-ray beam tails as mentioned earlier. Because the spin state of Fe stays constant after decomposing $HS\text{-}FeCO_3$, the new phase ($Fe_4C_3O_{12}$) must also be in an HS state as expected [74, 42]. In addition at $51.8\,\text{µJ}$ first signs of melt appear in the diffraction signal but stay minor below $255\,\text{µJ}$.

Above $144\,\text{µJ}$ the appearance $CO_2\text{-}V$ indicates further decomposition. Due to a stable spin state for $FeCO_3$, decomposition or incongruent melting of $Fe_4C_3O_{12}$ instead of $FeCO_3$ is more likely. The diffraction peaks for $Fe_4C_3O_{12}$ show strong broadening. However, $FeCO_3$ is still the dominant phase. Taking this into account, our data suggest the following reaction paths during several heating cycles in the centre of the heating spot below $144\,\text{µJ}$:

$$HS{-}FeCO_3 \xrightarrow{\text{T}^+} Fe_4C_3O_{12} + HS{-}FeCO_3 \xrightarrow{\text{T}^-} Fe_4C_3O_{12} + LS{-}FeCO_3, \quad \text{(R1)}$$

and above $144\,\text{µJ}$ and during quenching and subsequent pressure release:

$$Fe_4C_3O_{12} \xrightarrow{\text{T}^+} \text{melt} + CO_2$$
$$\xrightarrow{\text{T}^-} \text{glass} + CO_2 \xrightarrow{\text{p}^-} Fe{-}\text{oxides} + CO_2 \cdot \quad \text{(R2)}$$
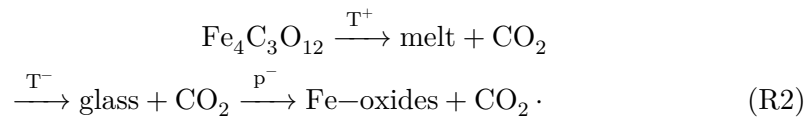
In conclusion, the combination of simultaneous XES and XRD with an X-ray heated DAC at an XFEL facility has been successfully tested. The sample was heated well above heating temperatures, without temperature isolation to the diamond anvils. The diamond anvil showed only minor effects due to the combined several hours of X-ray pulse exposure. This result allows for increasing the number of pulses per train from the conservatively chosen 10 pulses/train up to several 100 pulses/train, limited by the exposure window of the detector. This would improve the experimental data in two ways. Firstly, the signal for the emission signal would increase by a factor of at least 10, relative to the presented high-noise data from this experiment when collecting the same amount of trains, allowing for vtc analysis. Or it would decrease the exposure time, i.e. collected pulse trains, by a factor of 10. Secondly, the temperature increase after each X-ray pulse and the cooling start to reach an equilibrium after 8-10 pulses [9]. When using 10 pulses/train the train resolved data consists of measurements at 10 different temperatures, increasing the complexity of analysing *in-situ* data. When 100 pulses/train are used, the first 10 pulses of the pulse train heats the sample, while the remaining 90 pulses probe the same temperature. Train resolved data then consists of 90 % data taken at the same temperature, which is favourable when using 10 Hz detectors.
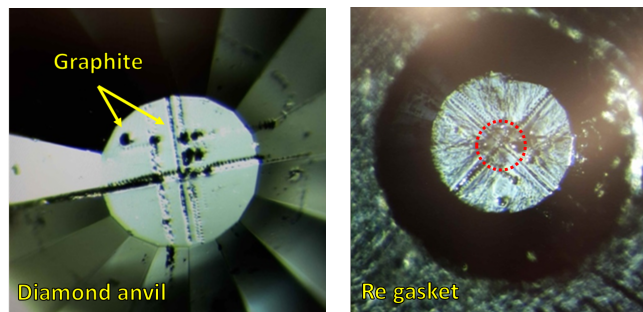
Figure 3.13: Damages on the diamond anvil [**Left**] showing trenches of graphite, where the focused beam was moved through the sample, and the gasket [**Right**] which was melded during a failed experiment. The damage was caused by a highly focused not-attenuated beam scanning the sample.

3.6.1 Implications for Diamond anvil cells

The energy threshold for non-thermal damage of the diamond anvil is 0.7 eV/atom [91]. For a maximum of 120 µJ energy per pulse on the diamond anvil and a focus of 20 µm × 20 µm (FWHM, H x V) $Q_{max} = 0.004$ eV/atom, which is well below the

damage threshold. For a focus of $10\,\mu m$ and $5\,\mu m$ the maximum pulse energy to stay below the damage threshold is $5000\,\mu J$ and $1000\,\mu J$, respectively. Thus, the graphite within the diamond was not caused by radiation damage but must have been due to thermal damage. Temperatures within the diamond anvil can exceed $1000\,K$ [9] during the X-ray heating of the sample. At this temperature, graphite becomes energetically favourable above diamond at a pressure below $4.3\,GPa$ [92]. Assuming a linear pressure gradient from the culet to the anvil back-side, this pressure is achieved $250\,\mu m$ below the anvil back-side. When the focused beam is positioned on the Re gasket, which is in closer proximity to the diamond culet, the temperatures on the diamond culet get much higher, which was tested during a test run in a DAC at $5\,GPa$. The resulting graphite trenches on the diamond and scanning lines on the gasket can be seen in FIG 3.13.

4 X-ray heating in a DAC: A high-resolution spectrometer setup at HED

The final setup for the following experiments in CHA 5 and future user-supported experiments was designed, implemented and thoroughly commissioned in IC1 at the HED instrument at the European XFEL. This chapter presents the results of multiple experiments conducted to classify current capabilities and future possibilities using the von Hámos spectrometer. The spectrometer was tested by measuring XES on free-standing metal foils and DACs loaded with $(Fe_{0.5}Mg_{0.5})O$ and FeS using SASE beam, and by measuring non-resonant inelastic X-ray scattering and XRS on a diamond sample in combination with a monochromatic beam.

Parts of this chapter were published earlier by Kaa et al. [29].

4.1 von Hámos spectrometer at Free-electron-lasers

Spectrometers are a crucial tool for the analysis of emitted or scattered X-rays at synchrotron facilities, by providing high energy resolution and efficiency. There are several spectrometers utilizing the von Hámos geometry available at hard X-ray FEL beamlines, each providing unique specifications for different measurement approaches. Spectrometers dedicated for single pulse measurements, e.g. at the FXS beamline at PAL-FEL [93], MEC at LCLS [94] or at the HED instrument at EuXFEL [95], are most commonly based on poly-crystalline mosaic analyser made from either highly oriented or highly annealed pyrolitic graphite (HOPG, HAPG) and provide high reflectivity with an energy resolution of several eV. This setup is usually applied to low-photon-yield methods such as Thomson scattering [96, 97] or non-resonant IXS, including plasmon excitations, in e.g. warm dense matter [98, 99, 100]. On the other hand, perfect, bent or segmented crystal analysers, e.g. tested at LCLS [101] or at PSI [102], have a higher energy resolution in the sub-eV regime with a lower efficiency and therefore have to rely on a combination of multiple analyser crystals in the spectrometer array.

X-ray spectrometers dedicated for measurements from a DAC are scarcely available at 3rd or 4th generation synchrotrons (e.g. DESY [89], APS [103] or ESRF [104]), however, until now there is no spectrometer dedicated for DAC measurements available at an FEL beamline.

4.2 Spectrometer concept and characterisation

The spectrometer follows the von Hámos geometry, described in SEC. 2.1.4. It was implemented on the circular rail on the horizontal breadboard in the large vacuum chamber IC1. It is operated under UHV conditions and is combined with either the Fast sample scanner (FSSS) or a DAC changer for fast DAC exchange. Therefore, the space impact on the Hexapod sample positioning system in the centre of the circular rail needs to be as small as possible to reduce the risk of collisions. The available space in IC1 allows for a sample-analyser crystal distance of 250 mm. The 4 x 1 analyser crystal positioning system was designed and manufactured together with JJ X-ray [105]. Due to the small opening angle of below 25° in a BX90-RD between DAC and gasket the analyser crystals need to cover a horizontal angular acceptance of at least 440 mrad, which corresponds to a analyser crystal width of 110 mm. The energy window needs to be above 100 eV to cover the Kβ emission including the K$\beta_{1,3}$ and vtc line. For a d spacing of 0.9 Å at 7.0 ± 0.5 keV the Bragg angle would range from 77.60 to 82.31°, resulting in a required analyser crystal height of 20 mm. To increase the signal intensity 4 analyser crystals are put into one column with a distance of 7 mm between analyser crystals to align them on the respective Rowland circle. To prevent damage through collision, iron foils with different electrical polarities are placed above and below each analyser crystal. The foils are connected to a DC voltage, activating a limit switch when two foils are touching. When using four analyser crystals, the signal of each crystal on the detector needs to be shifted. Thus, each crystal needs to be controlled in pitch, to control and correct the Bragg angle, and roll and yaw to horizontally shift the signal slightly on the detector array and optimise the focus of each crystal individually. This also allows for individual background correction of each of the four spectra. For larger positioning of the height, distance and parallel shift to the beam, the analyser crystal unit is placed on a combination of motorised linear OWIS stages. The XYZ-tower provides a movement of 300 mm for the height and 15 mm for the distance and parallel shift and controls the optimal focusing of the spectrometer. In horizontal 180° to this tower, a second XYZ-tower for the detector positioning is placed on the circular rail. The detector

array can be placed at a minimum height of 25 mm above the sample, limited by the sample environment and at a maximum height of 350 mm, limited by the dimensions of the vacuum chamber. This allows for a Bragg angle between 60 to 80° for an analyser crystal-sample/detector-axis distance of 250 mm. With the x and z stages, the detector can be controlled for perfect positioning of the detector array above the sample. For experiments conducted at 10 Hz , a Jungfrau500K (JF) [106] was placed on the detector tower. The setup can be freely placed in a 360° horizontal scattering angle, which allows for the versatile placement of additional detectors downstream of the sample for XRD measurements. Additionally, in most cases, an in-line microscope can be placed in the beam for optical control of the beam position and changes in the sample during measurements.

To exchange a DAC after an experiment run, IC1 needs to be vented and pumped. This procedure can take up to 60 min. To make the sample exchange while using DACs more time efficient, a rotational stage for up to 3 DACs utilizing a piezo-driven stage is put on the Hexapod. In between the DAC chambers, several free-standing samples can be placed on a flat aluminium piece. The samples within this DAC changer can be changed by rotating the changer without venting the vacuum chamber. The CAD design of the setup with the DAC changer and built-in IC1 is shown in FIG 4.1.
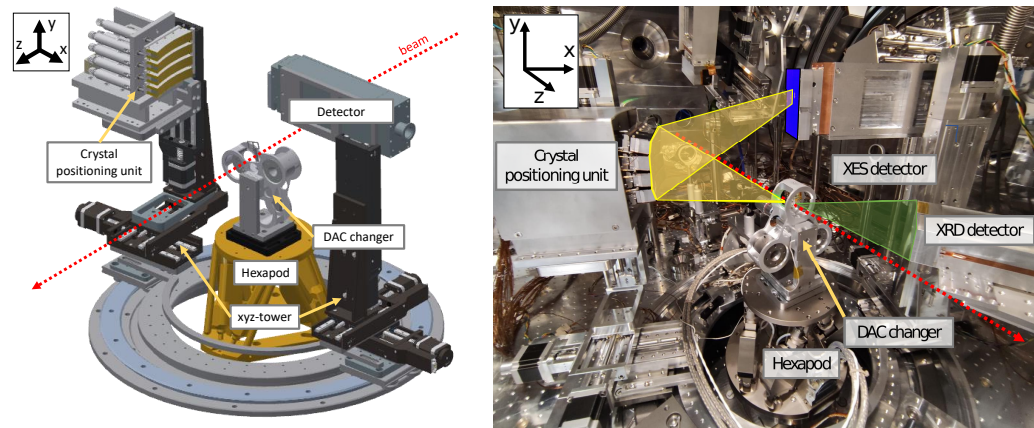
Figure 4.1: [**Left**] CAD design of the spectrometer on the circular rail in IC1. The analyser crystal positioning unit and the JF detector are placed on linear XYZ stages. Each tower sits on a slider on the circular rail surrounding the Hexapod. The DAC changer sits on the Hexapod, providing space for three DACs with a diameter of 50 mm. [**Right**] The setup assembled in IC1 with the beam path (red), the path for the emission (yellow) and the diffraction (green) signal. Figure is taken from Kaa et al. [29].

The crystals are cut from 180 µm thick Si and Ge wafer and are glued on a polymethyl-

methacrylate (PMMA) substrate with a bending radius of 250 mm. The substrate has a minimum thickness of 10 mm and was additionally glued on a 5 mm adapter plate to attach them to the spectrometer. The crystals were bought from the Crystal Analyser Laboratory (CAL) at the ESRF and by Compagnie de Saint-Gobain S.A.. To cover a wide range of energies in the possible Bragg range and enable the highest flexibility for multi-colour experiments, several cuts and crystal types were chosen. Available analyser crystal orientations are listed in TAB 4.1. The d-spacing values from first-order reflections range from 0.8281 to 3.2660 Å.

Crystal	Si(531)	Si(111)	Si(533)	Si(511)	Ge(220)	Ge(111)
d-spacing (Å)	0.9179	3.1355	0.8281	1.0451	2.0000	3.2660

Table 4.1: Available analyzer crystal sets with various crystallographic orientations. d-spacing in Å is given below.

FIG 4.2 shows the energy range covered by all available analyser crystals up to an energy of 12 keV including the energy window for the respective analyser crystal at a given Bragg angle. The analyser crystals cover the soft X-ray regime between 2 to 3 keV and the hard X-ray regime above 5.5 keV.
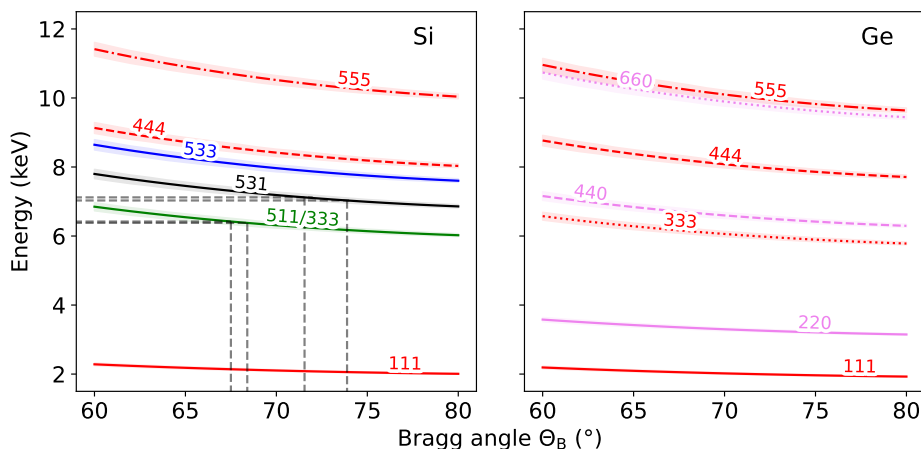
Figure 4.2: [**Left**] Diffracted photon energy ranges for Si(111) (red), Si(511) (green), Si(531) (black) and Si(533) (blue) and [**Right**] Ge(111) (red) and Ge(220) (violet) for an Bragg angle range from 60 to 80°. The shaded area shows the range of a crystal at a given Bragg angle. The Fe Kα and Kβ line from 6190 to 6410 eV and from 7020 to 7120 eV, respectively, and the responding Bragg angle for a Si(531) are plotted as a line (black, dashed). Changed after Kaa et al. [29].

Due to the large active area of the JF detector of roughly 8 cm × 4 cm (H x V) the diffracted signal of each analyser crystal, which appears as a vertical line, can be placed beside each other (see FIG. 4.3). Each signal can be noise-corrected, calibrated

and analysed individually. It allows for the utilisation of combined Bragg angle ranges to conduct multi-colour experiments by e.g. collecting with a different crystal orientation for the uppermost analyser crystal, compared to the remaining 3 crystals. When different crystal orientations are combined, multiple energies can be collected at the same time. For example, when working with Fe in a DAC, one could use a combination of Si(531) for the lower 3 analyser crystals and Si(111) for the top crystal to collect the Fe Kβ (see FIG 4.2) at higher Bragg angles (72 to 73°) and, using the third and fifth order reflection of Si(111), collecting the Fe Kα (see FIG 4.2) and Re Lα of the gasket at lower Bragg angles (65 to 68°). Figure 4.3 shows example images of the detector for this case and when using Si(111) for all 4 analyser crystals, measuring Fe Kα.
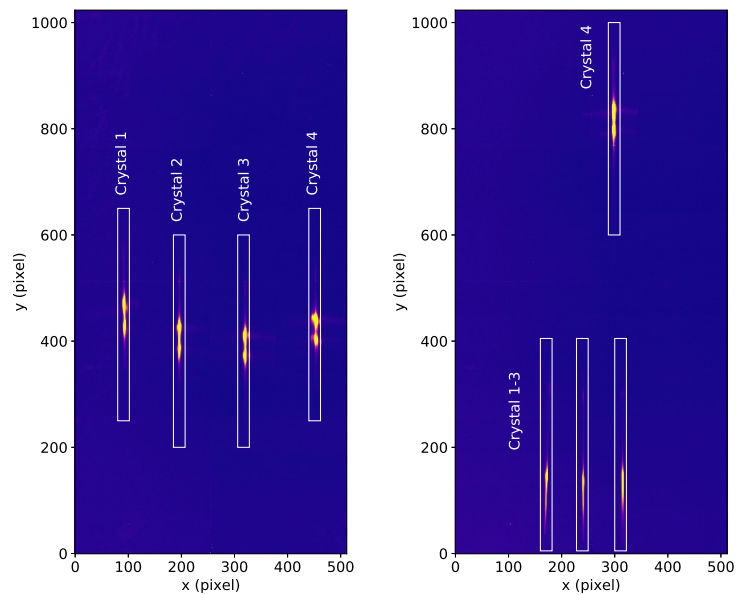
Figure 4.3: [**Left**] Detector array showing the reflections of Fe Kα using Si(333) for all 4 analyser crystals. [**Right**] Detector array of Si(111) for the top crystal, showing the Fe Kα reflection, and Si(531) for the remaining crystals, measuring the Fe Kβ line in various intensities [29].

The energy bandwidth of the spectrometer E_g for the geometric components (source size and detector pixel size, see FIG 2.6) is calculated by

$$\Delta E_g = \sqrt{\Delta E_y^2 + \Delta E_r^2 + \Delta E_d^2}, \tag{4.1}$$

with the contribution of the source size ΔE_y and ΔE_r, as well as the contribution of the pixel size of the detector ΔE_d [107, 29]:

$$\frac{\Delta E_y}{E} = cot\theta_{\mathrm{B}}\frac{rs_y}{r^2 + c_y^2}, \tag{4.2}$$

$$\frac{\Delta E_r}{E} = -cot\theta_{\mathrm{B}}\frac{c_y s_r}{r^2 + c_y^2}, \tag{4.3}$$

$$\frac{\Delta E_d}{E} = cot\theta_{\mathrm{B}}\frac{rp_d}{r^2 + c_y^2}, \tag{4.4}$$

for the vertical beam size s_y, the beam width and sample thickness s_r, the y position of the analyzer crystal c_y, and the detector pixel size p_d. Figure 4.4 shows E_g for all available Si crystals assuming a beam size and sample thickness of $10\,\mu\mathrm{m}$ and a pixel size of $75\,\mu\mathrm{m}$. Above Bragg angles of 65° all crystals provide a geometric energy resolution E_g in the sub-eV regime. This calculation is for an ideal von Hámos geometry, and does not include further geometric effects, caused when using multiple crystals, such as non-linear widening of the focus due to necessary tilting-corrections of the crystals.
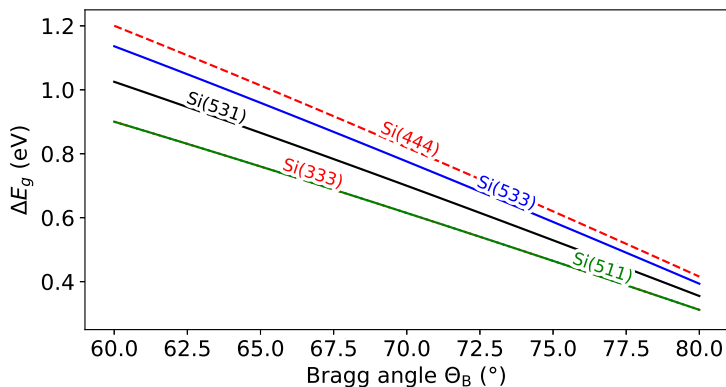
Figure 4.4: Geometric energy resolution E_g for all Si crystals (Si(333) and Si(444) (red, dotted and dashed), Si(511) (green), Si(531) (black) and Si(533) (blue)) available assuming a beam size and sample thickness of $10\,\mu\mathrm{m}$ a pixel size of $75\,\mu\mathrm{m}$.

4.3 Analyser crystal characterisation

Reflectivity measurements from strongly bent crystals are difficult to obtain. In an X-ray tube, the spot size on the crystal is sufficiently large to get affected by the horizontal bending of the crystal and therefore determines reflectivity values with insufficient accuracy. When using slits to decrease the horizontal spot size, the necessary exposure time due to the decreased intensity would be unproportionally long. On the other hand, at a synchrotron facility, the X-ray bandwidth needs to be reduced by a monochromator to be equal to or below the bandwidth of the measured analyser crystal. Perfect crystals have a similar bandwidth as the monochromators and thus the resulting rocking curves are a convolution of the monochromator and the measured crystal rocking curve. An alternative is to simulate the rocking curves using 1D Tagaki–Taupin equations [108, 109, 110]. Figure 4.5 shows a comparison between a simulated and a measured rocking curve for Si(531) at an energy of 14 keV, i.e. a Bragg angle of 28°. The measurements were conducted at BL9 of the Delta synchrotron using a double-bounce Si(311) monochromator ($\Delta E/E \approx 5 \times 10^{-5}$) and a vertical beam size of 20 µm. The crystal was rotated in 5.76 µrad steps and the signal was collected on a Pilatus100K area detector [111] in Bragg reflection geometry with a fixed position. The diffracted signal on the detector was normalised to the signal of the direct beam on the detector and to the photon flux measured by the signal on the I0 diode.
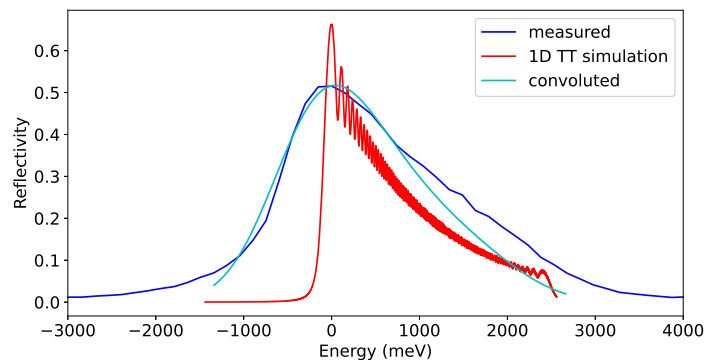
Figure 4.5: Measured (blue) and simulated (red) Si(531) rocking curve at 14 keV, i.e. 28° Bragg angle by solving the 1D Tagaki–Taupin equations using the pyTTE python package [a]. The convoluted signal (cyan) between the calculated rocking curve and an area normalised Gaussian distribution (FWHM = 0.6 eV) takes the bandwidth of the monochromator during the measurement into account.

---

[a]The python script was provided by Dr. C. J. Sahle

The form of both curves looks similar, with a comparable peak reflection between 0.5 to 0.65 . However, the FWHM of the measured curve is twice as much as that of the simulated curve due to the convolution between the measured crystal and the double-bounce monochromator. Thus, for the characterisation of the pure crystals, we will rely on the simulated values. Calculated curves for Si(531), Si(511), Si(333), Si(444) and Si(533) are shown in FIG 4.6 for Bragg angles 60°, 70° and 80°. From these curves, we can determine the Darwin width ΔE_{WD} of each analyser crystal, which shows a maximum of 0.23 eV for Si(533) at 60° (see TAB S2). Thus the crystal's energy bandwidth is in the sub-eV regime with a factor of 5-10 less compared to the HOPG crystals implemented in the respective spectrometer [112, 100]. From the reflection curve, we can also calculate the efficiency ϕ of the spectrometer for a source emitting in 4π, with the horizontal acceptance Ω_{lc}, the vertical acceptance R, given by the integral of the rocking curve, for an energy range given by its FWHM E_{FWHM}:

$$\phi = 4 \times \frac{\Omega_{lc} \times R}{4\pi \times E_{FWHM}} \left[\frac{\text{sr}}{\text{sr} \times \text{eV}} \right]. \tag{4.5}$$

All values taken from the rocking curves (FWHM, integrated reflectivity and peak reflectivity) are given in TAB S2.
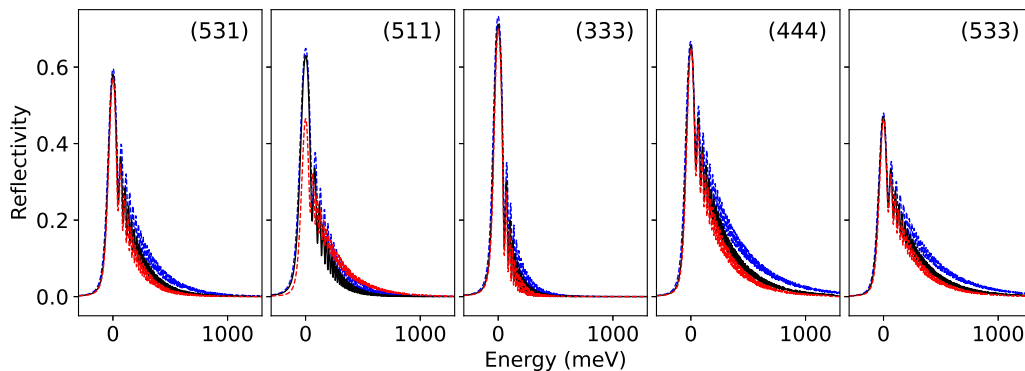
Figure 4.6: Rocking curves calculated by the 1D TT equations for Si(531), Si(511), Si(333), Si(444) and Si(533) for 60° (blue), 70° (black) and 80° (red). The crystals bandwidth (FWHM) gets smaller with increasing Bragg angles.

The values for ϕ for all three Bragg angles are given in TAB 4.2. Thus, we can say that the spectrometer collects for all available Si crystals between 1.80×10^{-5} to $12.90 \times 10^{-5}\,\text{eV}^{-1}$ of all photons emitted in 4π.

(hkl)	531	511	333	444	533
$\phi_{60°}$	2.53	3.06	4.11	2.45	**1.80**
$\phi_{70°}$	4.69	4.76	6.42	4.14	3.07
$\phi_{80°}$	9.52	9.02	**12.90**	9.56	7.19

Table 4.2: Efficiency values for EQ 4.5 calculated from values given in TAB S2 based on the rocking curves in FIG 4.6. All values are given in e-5/eV.

4.4 X-ray emission spectroscopy commissioning measurements

The setup was commissioned by measuring the Kα and Kβ emission lines including the vtc signal from free-standing metal foils for Fe, Ni and Co. The foils had a thickness of 5 μm and a purity of 99.99 %. Additionally, the Kβ, Kβ', Kβ_2 and Kβ_5 of Ge was measured from a GeO_2 powder placed between two Kapton foils. The foils and powder were mounted on the FSSS on the Hexapod. The photon energy of the XFEL beam was set to 13.16 keV in SASE mode with an energy bandwidth of $\Delta E/E \approx 1.3 \times 10^{-3}$ determined by the HIREX spectrometer [113]. The beam was operated either at single pulse mode, providing one pulse per train at 10 Hz, or using 50 to 200 pulses at 455 kHz. The maximum pulse energy was 850 μJ providing a photon flux of 4.1×10^{11} photons/pulse. However, the beamline transmission through CRLs, mirrors, etc can be estimated to be below 50 %. The beam was focused to 60 μm (FWHM) using CRLs, further decreasing the beamline transmission. The spectrometer was placed in a back-scattering near-100° horizontal scattering angle. One has to note that during the measurements, a significant inter- and intra- pulse train jitter caused a horizontal and vertical movement of several beam sizes, estimated by the signal reaching the beamstop diode when using a pinhole (e.g. the sample hole in a Re gasket).

To characterise the spectrometer, we measured the Fe and Co Kβ and vtc line Ni and Co Kα line using a set of four Si(531) crystals, and with a set of Si(111) in third order reflection the Fe Kα and fourth order the Ni and Ge Kβ. Depending on the pulse pattern and thus the photon flux and the fluorescence cross-section the emission signal was collected for 2 to 5 min. Using high-resolution references by Hölzer et al. [114] and Ito et al. [115] we calibrated each crystal signal (not including Ge) assuming a linear energy dispersion by fitting either the Kα_1 and Kα_2 peaks or by fitting the K$\beta_{1,3}$ and vtc peaks. Afterwards, the four signals were background corrected, added together and normalized to a peak value of 1.
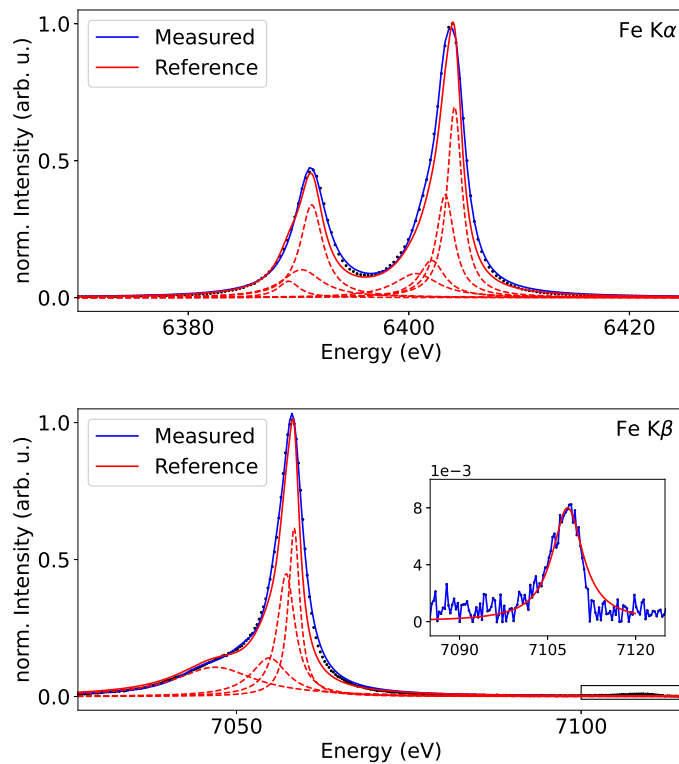
Figure 4.7: Measured (black) Fe Kα [**Top**] and Kβ and vtc emission lines [**Bottom**]. A set of Lorentzians (blue) were fitted to the experimental data to compare them to the references [114] (red) fitted by multiple Lorentzians (red, dashed). The broadening between the experimental data and the references gives us an idea about the instrumental broadening of the setup.

Figure 4.7 shows the measured spectra for Fe Kα and Kβ. A combination of multiple Lorentzian was necessary to achieve a near-perfect fit to the experimental data. The reference data, also consisting of multiple Lorentzian curves [114, 115], have a smaller FWHM for the peaks in comparison to our experimental data. The value of the broadening compared to the reference give us the instrumental broadening value. Table 4.3 summarises the FWHM values for all measured emission lines and for Fe, Ni and Co references. Fe Kβ was measured in a second and third experiment described in SEC 4.6 and 4.5. The instrumental broadening can be assumed as a Gaussian function. The mean Gaussian difference of all values is 2.13 ± 0.56 eV, which is well above the geometric broadening shown in FIG 4.4.

	Kα_1	Kα_2	Kβ
Fe	3.28 (2.55)	3.59 (3.14)	4.58 | 3.62^a | 3.60^b (3.53)
Ni	2.83 (2.24)	3.69 (3.16)	5.99 (5.40)
Co	2.93 (2.33)	3.47 (3.18)	5.36 (4.37)
GeO$_2$	-	-	8.14

Table 4.3: FWHM of measured fluorescence signals. Reference FWHM is given in parentheses.

---

^{a}with monochromatic and highly stable beam (taken during section 4.6)

^{b}with SASE beam and highly stable beam (taken during section 4.5)

This effect is due to the beam jitter, which enlarges the area of the beam on the sample, especially in the horizontal direction. We estimate an increase from 60 µm to at least 200 µm. Taking this into account we can calculate ΔE_g for a vertical beam size of $s_y = 60$ µm and an effective horizontal beam size of 200 µm. For those values and between 65 to 75° ΔE_g has a value between 1.5 to 2.5 eV for Si(531), Si(333) and Si(444), which is in good agreement with FWHM data presented in TAB 4.3. The signal output from the detector image can also be used to estimate collected photons on each pixel when the energy of the detected photon is known by dividing the output signal by the photon energy. Thus it allows us to calculate the number of collected photons and in comparison with the mean photon flux gives us an estimation of the efficiency of the setup. For a run at 13.16 keV with a photon flux of (50 µJ, i.e. 2.36×10^{10} photons on the sample, measured by diodes that were initially calibrated) on a Fe foil with a 5 µm thickness, the sample absorbs roughly 2.0×10^{10} photons. The Kα and Kβ, both measured with a single pulse with one crystal each, for this run, are shown in FIG 4.8. Taking the photoionization for Fe at 13.16 keV (80.6098 cm^2/g) and partial photoionization cross section for Fe K emission (71.7203 cm^2/g), the K shell fluorescence yield (0.3546) and the radiative transition probability (Kα 0.881 56,

Kβ 0.118 44)[116], we can estimate that 7.0×10^9 photons for the Kα emission and 9.44×10^8 photons for the Kβ emission are emitted in 4π. The sum of the collected photons on the detector is 30 000 photons for Kα and 9700 photons for Kβ, both for a roughly 100 eV window and with a $1.2 \times 10^{-5}\,\text{eV}^{-1}$ calculated spectrometer efficiency for a single crystal.

4.5 XES from a DAC - X-ray heating and single pulse

We conducted two DAC experiments with two different approaches (multi-pulse and single-pulse measurements), for testing the capabilities of the spectrometer to measure XES from samples contained in a DAC.

The multi-pulse experiments was conducted on $(\text{Fe}_{0.5}\text{Mg}_{0.5})\text{O}$. The sample was loaded in a DAC in a similar manner as described in SEC 2.3 using a Re gasket in an Ar pressure medium and was pressurised to $100 \pm 5\,\text{GPa}$ using diamond anvils with a diameter of 100 µm. The pressure was determined before the experiment by the Raman shift of the diamond peak and during the experiment using the EOS for Pt [117] at ambient temperatures. The latter was mixed with the sample powder before loading, for an internal temperature and pressure measurement and better X-ray coupling and subsequent additional indirect heating of the sample. Changes including volume changes due to heating were monitored with an ePix100 XRD detector. The detector was covered by a 5 µm thick Cu plate to prevent overexposure. The pulse pattern was set to 100 pulses/train at 2.2 MHz with a photon energy of 13.16 keV and a focus of 20 µm (FWHM) to heat and probe the sample at high temperatures. To prevent beam jitter, a different CRL combination and an inter-train beam po-
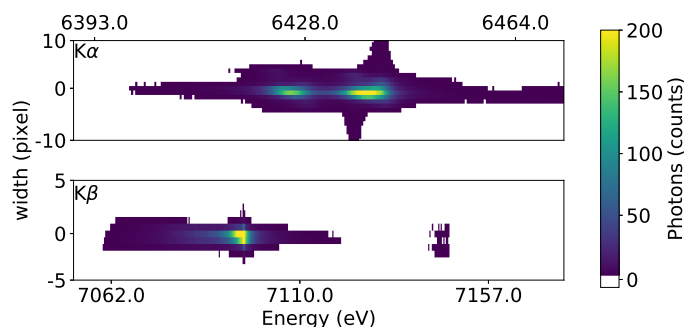
Figure 4.8: Single pulse detector image photon counts for Fe Kα [**Top**] and Kβ [**Bottom**] emission of a free-standing foil collected at full beamline transmission using Si(333) and Si(531).

sition feedback system were used for this run. The pressure-induced HS-LS and subsequent heating-induced LS-HS transition with an HS fraction below 50 % has been thoroughly researched [118, 119] for different fractions of Fe. By extrapolation of this data, the HS fraction should reach a value of 30 % at a pressure of 100 GPa at temperatures of 2500 K for 50 % Fe. The NaCl-structure of the sample (B1) stays stable throughout the reached pT conditions [120] until melting temperatures. The sample is therefore eminently suitable for probing with multiple heating cycles and with the particular heating pattern achieved during X-ray heating (see SEC 3.3) at the chosen pressure. Each run was collected over 3 to 5 min at the given pulse energy. FIG 4.9 shows the sample before heating at near ambient temperatures at $40.1 \pm 9.3\,\mu$J. The XRD signal consists of cold Re, Pt and the sample $(Fe_{0.5}Mg_{0.5})O$. The Re signal was always present in the XRD due to the small size of the gasket hole of 30 µm. The temperature increase in the pattern measured at the maximum pulse energy of $837.0 \pm 14.0\,\mu$J can be estimated by the sample (200) peak shift. The continuous shift of the sample peak suggests heating of the sample with increasing pulse energies below the melting temperature, which would become apparent in a stagnation of the peak shift slope. The XRD shows no melting contribution to the signal. A strong peak shift can be seen in the Re triple peak, which means that the temperature gets conducted from the sample in the gasket and diamond anvil. This significantly decreases the heating efficiency and causes relatively low temperatures at the peak pulse energy. In addition, the high temperatures in the gasket and diamond anvil favours damage to the diamond anvils and likely caused the pressure collapse before the sample was quenched. The quenched sample was probed at near ambient pressures, showing mostly Re and Pt peaks, while the diffraction signal of the sample disappeared. After recovering the DAC, it became apparent that the upstream diamond anvil failed and the sample was lost for further analysis.

The Fe Kβ signal shown in FIG 4.10 shows the development during photon flux increase. The signal was energy calibrated using a reference signal from a free-standing iron foil (see TAB 4.3) and integral normalised between 7020 to 7080 eV. The noise improved significantly compared to SEC 3.4 and shows an SNR of 4 to 200 , allowing for ΔM1 and IAD analysis to determine the spin state. While the value is above the suggested value of 100 by Albers et al. [30], a vtc analysis is possible but shows no change, due to the lack of transitions in the geometry of the sample.

Both the ΔM1 and IAD value rise from an initial complete LS to a higher spin state fraction with increasing pulse energy and reaches a plateau at IAD = 0.7 and ΔM1 = 0.26 eV, corresponding to an HS fraction of 22 to 23 %, which is well in
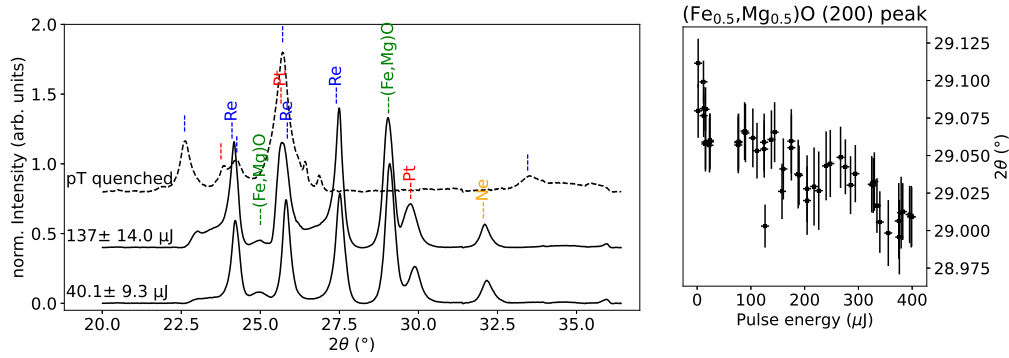
Figure 4.9: [**Left**] XRD pattern for $(Fe_{0.5}Mg_{0.5})O$ at $100\,GPa$ for near ambient temperature (bottom), at $2500\,K$ suggested by the Pt EOS (middle) and after quenching and pressure loss (top, dashed). Diffraction peaks are shown for Re (blue), Pt (red), Ne (orange) and $(Fe_{0.5}Mg_{0.5})O$ (green). [**Right**] With increasing pulse energy the (200) sample peak shifts to lower 2θ angles, suggesting a continuous temperature increase. Figures are taken from Kaa et al. [29].
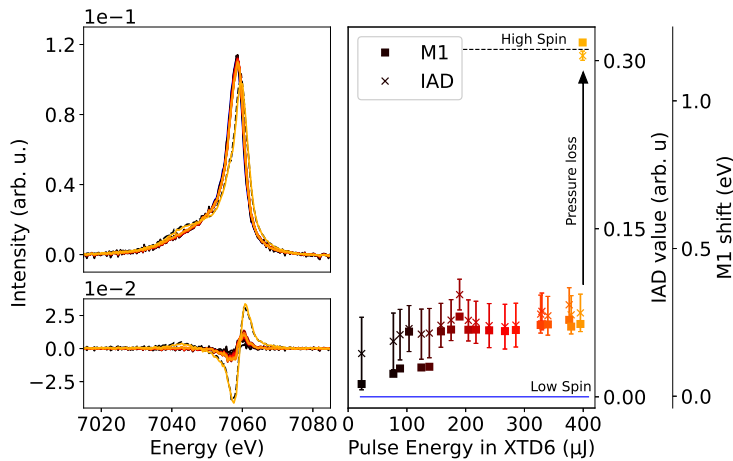
Figure 4.10: $K\beta_{1,3}$ emission for Fe in $(Fe_{0.5}Mg_{0.5})O$ as function of pulse energy. The difference against an LS reference shows an increase of the $\Delta M1$ and IAD value with increasing pulse energy, i.e. peak temperatures. During pressure loss the sample switches from an HS fraction of 22 to 23 % into a full HS. Figure is taken from Kaa et al. [29].

line with suggested HS fractions from earlier experiments at peak temperatures of 2500 K. During the last run and during pressure loss, the sample switches back into a complete HS state.

In the single pulse experimental run, we used the FeS sample compressed to 32.0 ± 0.5 GPa using diamond culet of 300 µJ diameter and Ne, gas loaded as pressure transmitting medium. The pressure was determined by the Raman peak shift of the diamond anvils. The pure sample was loaded as a compressed powder in a Re gasket. The beam pulse pattern was changed to single pulse mode, providing a single X-ray pulse at 10 Hz, allowing for single pulse measurements in combination with a 10 Hz detector. The same photon energy and focus from the earlier experiment were used. The beamline transmission was set to 100 % providing 500 µJ, i.e. 2.37×10^{11} photons, on the sample. The spectrometer was equipped with three Si(531) and one Si(111) analyser crystal to measure Fe Kβ and Kα simultaneously. The run was accumulated over 8000 pulses.

Figure 4.11 shows the collected emission signal of a single pulse-train, comparable to four analyser crystal signals accumulated for both K emission lines. The four pulses providing the highest photon flux on the sample and the analyser crystal reflection with the highest intensity were added together. This allows for estimating the optimal signal that can be achieved using a single pulse for a spectrometer equipped with four equal analyser crystals.
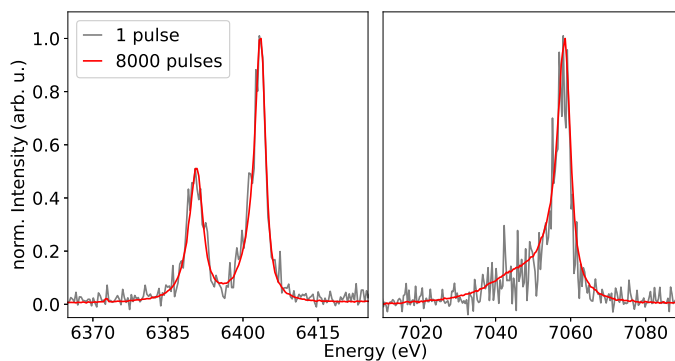
Figure 4.11: Single pulse Fe Kα [**Left**] and K$\beta_{1,3}$ [**Right**] emission for FeS at 32 GPa. Both signals were accumulated over 4 pulses using a single crystal reflection, simulating a single pulse run with four equal crystals (grey). The full 8000 pulse run shows three Si(531) and one Si(111) signal (red). Reproduced after Kaa et al. [29]

Kα shows an SNR of 10, providing an excellent intensity for a sub-eV energy resolution.

Despite the low SNR of the Kβ signal of 2.5, it allows for an assessment of the expected LS state of FeS at the given pressure. To be able to confidently conduct single-pulse spin-state studies from a DAC, the photon flux for the Kβ emission would need to improve by a factor of 4 to 10, to achieve similar data quality as in SEC 3.4, which will become possible when using a seeded beam or when achieving a higher pulse-throughput of the monochromator.

4.6 Inelastic X-ray scattering from ambient samples

While the spectrometer is not only limited to DAC measurements, it can also be applied to measurements besides relatively intense XES. Therefore, we tested its capabilities of measuring IXS and, in the special case of core electron scattering, XRS on free-standing samples. In both cases, IXS on valence electrons, and XRS were tested on an ambient multi-crystalline diamond sample. NRIXS measurements rely on a monochromatic incoming beam with a bandwidth comparable to the setup's sub-eV bandwidth, which is not given for a SASE beam. Therefore, the four-bounce Si(111) monochromator [33] was put into the beam. It was then set to an energy of 7100 eV for IXS and 7360 eV for the XRS measurements. The provided energy bandwidth of the monochromator is $\Delta E/E \approx 1.3 \times 10^{-4}$. To increase the photon flux after the monochromator, only one of the double-bounce monochromators was used. The beam profile was set to 5 pulses/train at 455 kHz while only 2-3 of the pulses per train reached the sample due to the heating of the monochromator. The beam was focused to 40 µm and was operated at full transmission using 2.2 mJ with roughly 500 µJ on the sample.

The spectrometer was placed in forward geometry at a horizontal scattering angle of 20°, equipped with four Si(531) crystals to measure energies between 7000 to 7100 eV for collecting a high-resolution Fe Kβ emission line and for focussing of the crystals, 7100 to 7200 eV for IXS and 7380 to 7480 eV for XRS measurements, in order to measure the energy losses in a range of 0 to 100 eV and 280 to 380 eV, respectively, to cover the signal from plasmon and K edge scattering. The four analyser crystals covered a scattering range of 10 to 15°. The Fe foil had a thickness of 5 µm. The diamond plate had a thickness of 400 µm and consists of diamond grains, synthetically grown in multiple directions with (111) as the preferred and dominant crystal orientation. Both samples were mounted on the FSSS and were individually moved into the beam for their measurements. Data on the Fe Kβ can be found in TAB 4.3. The broadening for this measurement, assuming a Gaussian

distribution is 0.80 eV.

For the IXS measurements of plasmon excitation in diamond, the spectrometer was placed with a central Bragg angle of 70.80°, which corresponds to a momentum transfer of $1.5\,\text{Å}^{-1}$. The central wave vector transfers q for 7100 eV for the four crystals from upper to lower crystal are $1.8\,\text{Å}^{-1}$, $1.6\,\text{Å}^{-1}$, $1.4\,\text{Å}^{-1}$ and $1.2\,\text{Å}^{-1}$. Thus, each crystal provided a different measurement of dynamic structure factor $S(q, \omega)$. The measurement was accumulated over 42 000 trains. Trains with low intensity on a photo-diode in the optics hutch were filtered out for an improved SNR. The energy window of the crystals for the IXS run was shifted to include the elastic line at 7100 eV. The pixels were energy calibrated using the elastic line and the energy dispersion set by the Fe Kβ measurement, assuming a linear energy dispersion per pixel for both measurements. The intensity was normalised to an elastic line maximum of 1.

Figure 4.12 shows the measurements from all four crystals as a function of the energy loss. References of Waidmann et al. [121] measured by electron energy loss
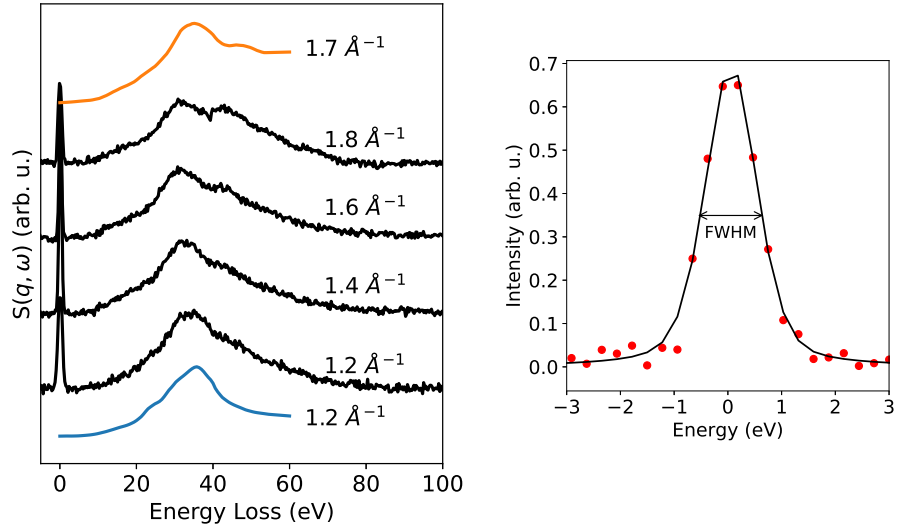
Figure 4.12: [**Left**] Plasmon and particle/hole-pair scattering on the diamond as a function of the energy loss and for different momentum transfers for each of the four Si(531) crystals (black). References [121] for $1.2\,\text{Å}^{-1}$ and $1.7\,\text{Å}^{-1}$ for a combination of diamond (100) (6/26th), (110) (12/26th) and (111) (8/26th) are shown (blue, orange). [**Right**] The elastic line (red, dotted) for crystal 2. The FWHM is calculated from a Gaussian curve fitted to the experimental data. Changed after Kaa et al. [29].

spectroscopy are plotted for a momentum transfer of $1.2\,\text{Å}^{-1}$ and $1.7\,\text{Å}^{-1}$ for a combination of equal parts (100), (110) and (111). With increasing q, the main peak between 20 to 60 eV, likely resulting from the bulk plasmon peak of diamond

at 33 eV[121, 122], shows increasing splitting and broadening resulting from the increasing influence of interband transitions in this energy range which can not be entangled due to the convolution of scattering signal along multiple unknown directions in the diamond sample. The elastic lines for all analyser crystals show a mean FWHM of 1.02 ± 0.23 eV, which is the combination of the energy bandwidth of the incoming beam, i.e. monochromator 0.7 eV [123], and the instrumental function of the spectrometer. Assuming a Gaussian distribution, the mean spectrometer bandwidth can be calculated to 0.74 eV, which is in line with the calculated intrinsic bandwidth of the setup.

For XRS measurements, we measured the C K edge of the same diamond sample. The photon energy of the beam was set to 7360 eV, while the sample and setup were not moved after the IXS measurement to keep the energy calibration for the XRS run. The run was collected over 3 hours with the same pulse pattern as before and was filtered with the same photodiode as before. During this run, a strong beam jitter decreased the signal on the sample significantly. The result is shown in FIG 4.13 with a reference by Schedel-Niedrig et al. [124]. The low SNR of 0.05 does not allow for analysing the data beyond fitting it to a reference spectrum and would need two orders of magnitude more in intensity to obtain meaningful interpretations but showcases the limits of the setup.
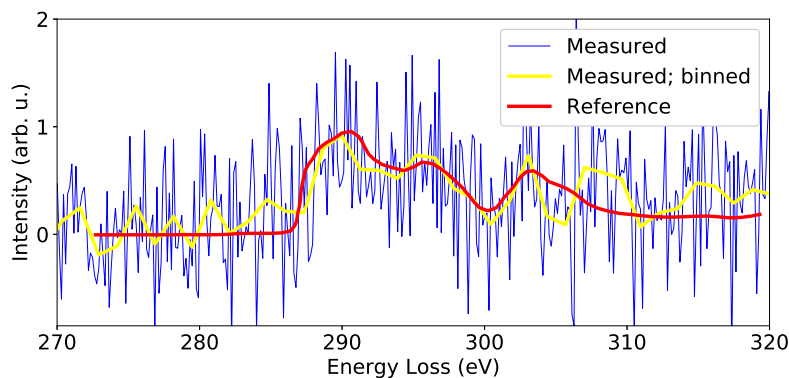
Figure 4.13: Carbon K edge from the diamond plate, measured over 108 000 pulse trains background corrected (blue) and binned (bin=9, yellow), which were filtered by the intensity of a photodiode after the X-ray optics. A reference by Schedel-Niedrig et al. [124] (red) shows the K edge in low noise quality.

4.7 Conclusion

The spectrometer provides a way to measure in versatile and flexible sample geometries including free-standing samples using the FSSS, allowing for sample exchanges at a 10 Hz repetition rate. The spectrometer provides to-date the only way to conduct X-ray spectroscopy measurements from a DAC at an XFEL beamline. With a SASE beam, it allows for high- and low-intensity XES measurements in the hard X-ray regime. From samples in a DAC and when utilizing pulsed X-ray heating, even minor changes in the electronic spin state of e.g. Fe can be detected during heating. To achieve high-quality data and to be able to measure electronic structures via vtc measurements, multiple trains, i.e. multiple heating cycles, have to be accumulated. Thus, this can only be applied to measure samples with reversible changes during heating and quenching. In combination with a monochromator, the spectrometer can be applied to IXS measurements with certain limitations, for example, it can only be measured from free-standing samples, which still can provide a wide field of applications.

The energy resolution of this setup is determined by the geometric energy fraction ΔE_g, the intrinsic energy resolution, i.e. Darwin width, of the crystals ΔE_D and the bandwidth of the source ΔE_s. At 7050 eV using a Si(531) crystal at a Bragg angle of 73.3° and for a beam size of 20 µm and sample thickness of 5 µm using a JF detector, ΔE_g is 0.71 eV. The Darwin width of the crystal is roughly 0.12 eV resulting in a setup bandwidth of 0.72 eV for XES experiments. This is in good agreement with Fe Kβ emission broadening (see TAB 4.3 and SEC 4.6 and 4.5), which is 0.75 ± 0.10 eV. It also agrees with measurements of the elastic line FWHM of 1.02 ± 0.23 eV, assuming a source bandwidth of 0.7 eV and a Gaussian distribution, which sets the setup bandwidth to 0.74 ± 0.30 eV. Thus, in this energy range, the spectrometer provides a sub-eV energy resolution.

The calculated efficiency for Fe Kα of 1.2×10^{-5} eV^{-1} per crystal overestimates the measured efficiency (3.8×10^{-7} eV^{-1}) by a factor of 30. This likely is due to less absorption in the Fe foil, which is caused by drilling a hole during the measurement and thus significantly higher transmission through the sample. This could be solved by using a constantly moving sample instead of shooting on a static sample or using a tamper as is the case while using a DAC.

The spectrometer's efficiency is sufficient for longer exposure times and close to being able to measure single pulse XES from a DAC. Latter would allow for either MHz-resolved XES using an MHz detector (e.g. Gotthard-II) to resolve inner train spin state changes to research chemically driven changes in the electronic spin state

of solids and melts. It could also open up the possibility for combining DACs with ultrahigh power and ultrashort fs pump laser to measure single pulse XES signals from pre-compressed dynamically laser-driven shocked samples as a function of the pump-probe-delay, potentially reaching pressures above the megabar regime and temperature above $1\,\text{eV}$, which would allow researching spin state dynamics at extreme conditions.

The setup reaches its limits when it comes to inelastic scattering measurements due to its relatively low efficiency. As beamtime at HED is scarce and therefore valuable, measurements of plasmon scattering over several tens of minutes or hours are not yet sufficient in combination with the monochromator. This will potentially change with the use of beam seeding at HED, which provides an intensity increase of rough factor 5 and an energy bandwidth comparable with a monochromator [36, 125].

5 Scientific case: XES on X-ray heated Iron sulfide at Martian core pressures

This chapter describes the first scientific application studied with the newly implemented von Hámos spectrometer at IC1 at HED (see CHA 4) of the European XFEL. FeS, as a simplified composition of the Martian core, was X-ray heated at pressures between 6 to 25 GPa up to melting, while the electronic spin state was monitored simultaneously to the change in phase and structure. The samples contained in three DACs at different pressures were temperature quenched after the HED experiment and were measured with a spatial resolution using XRD at P02.2 and XES at P01. Optical Raman spectroscopy was tested and found to be not required due to the lack of Raman active phases of FeS at the given pT conditions. In an additional run at beamline P01, the spin state data set was completed to cover the whole Martian core pressure, with an LH-DAC experiment at 40 GPa. The collected data allows for a first insight into the electronic spin state at pT conditions of the Martian core.

5.1 The Fe-S system in the Martian interior

Mars is the Earth's neighbour and the terrestrial planet in our solar system furthest away from the sun. It is the most researched planet regarding geomorphology, chemical composition and internal structure and its geological history (e.g. [126, 127, 128, 129]) with a main focus on biosignatures (e.g. [130, 131]), besides the Earth. Earlier studies on the interior of Mars were based on geochemical models and isotopic compositions of Martian meteoroids under the assumption of a chondritic bulk composition (see Morgan and Anders [132] and Waenke and Dreibus [133] as well as Burbine and O'Brien [134], and references therein). Mars missions, orbiting Mars or landing on the Martian surface, later provided geophysical properties, such as the density [135], the moment of inertia [136, 137, 138] and the tidal response (Love-number) k_2, and allow for making rough statements concerning the Martian interior. The moment of inertia < 0.4 indicates that Mars is differentiated into a

mantle and core, while $k_2 > 0.1$ suggests the core to be partially molten [137].
Combining geochemical and geophysical information provides for more detailed
constraints on the Martian interior by e.g. Khan et al. [139], who suggests a crust-
mantle boundary at 1100 km depth and a CMB in a depth of roughly 1700 km with
a molten FeNi core with up to 25 wt% S. The suggested pT conditions at the CMB
are 20 GPa and 2000 K. Other models suggest similar values from a core radius of
1800 km with a composition of Fe with 36 wt% S [140] to a core radius of 1480 km
with a composition of Fe/Ni with 15 wt% S [141].

The first seismic measurements from the Martian core stem from the InSight mission
[4, 5]. The lander is equipped with an instrument to measure the heat flow in a
depth of up to 5 m as well as a communication system to track the rotation of Mars
with a minute resolution. The main instrument of the rover is a seismometer which
collects seismic waves triggered by meteoroid impacts on the Martian surface. The
first results suggest a homogeneous mantle, similar in composition to the Earth's
upper mantle, without a transition zone to a lower mantle, due to insufficient pT
conditions for Bridgmanite to become stable. The core is in a molten state and has
a radius of roughly 1800 km [7]. The most recent published data [6] are based on
seismic waves passing through the core, further confirming its molten state and size
of the core. Stähler et al. [7] propose a core composition of FeNi with 10 to 15 wt%
S, up to 5 wt% O and traces (up to 1 wt%) of H and C with a CMB at 18 to 19 GPa
and 1900 to 2000 K. Irving et al. [6] suggest a core density of 6.2 to 6.3 g/cm^3 which
would agree with a Fe-alloy core with 20 to 22 wt% light elements. The maximum
core pressure is calculated to 38 GPa [142]. The existence of a solid inner core, similar
to the Earth's inner core, could neither be proven nor ruled out due to the lack of
spatial resolution of the seismic measurement.

The phase relations in the Fe$_y$S$_x$ system under high pT conditions during melting
becomes more complex for $x, y \neq 1$, i.e. below/above 36.5 wt% S and at pressures at
10 GPa and above. For the Fe–FeS system researched by Fei, Bertka, and Finger
[143], they suggest a eutectic melt with 18 to 21 wt% S and secondary phases Fe and
Fe$_2$S$_3$. With increasing pressure, the eutectic melt temperature rises while the wt%
of S in the melt decreases significantly ([144] and references within). At pressures
beyond the Martian core conditions, Fe$_3$S [145] and Fe$_2$S [146] have been reported.
For the simplified case of FeS there exist several confirmed structures at high pT
conditions as shown in FIG 5.1. In all structures up to FeS-VI Fe is in a sixfold
coordination. At ambient conditions, FeS crystallises in a hexagonal NiAs-like
structure ($P\bar{6}2c$) as the mineral Troilit. This hexagonal structure is also found in the
high pT phases FeS-IV ($P6_3mc$) [147, 148] and FeS-V ($P6_3\backslash mmc$) [149]. In those

two structures Urakawa et al. [150] reported a pressure-induced volume decrease of roughly 5 % between 4 to 12 GPa at 500 K and 1200 K, which likely can be connected to an HS-LS transition as similarly described in SEC 3.1, independently from the FeS IV-V phase boundary. Both phases stay stable at pressures up to 41 to 43 GPa. When FeS is pressurised at ambient temperatures, it forms the orthorhombic MnP-like structure FeS-II ($Pnma$) above roughly 3 GPa [151] and the monoclinic FeS-III ($P2_1 \backslash a$) above roughly 6 GPa [149, 152]. At even higher pressures above 40 GPa and high temperatures, the structure changes back to an MnP-like structure FeS-VI.
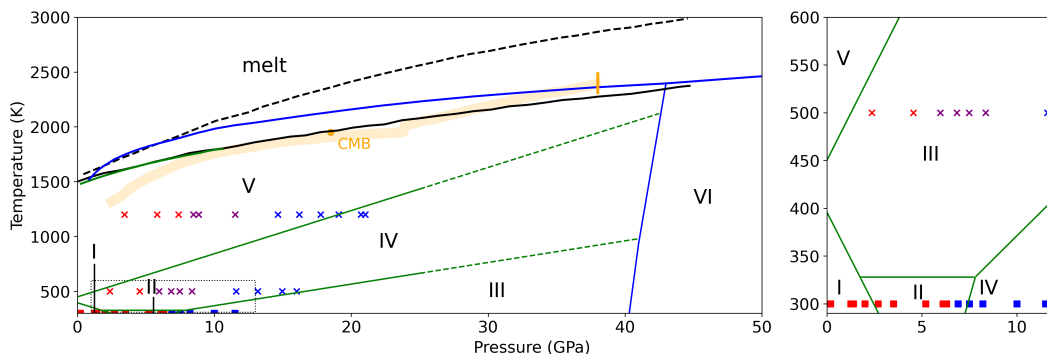
Figure 5.1: [**Left**] Compiled phase diagram for FeS at high pressure and temperature. Phase boundaries of Kavner, Duffy, and Shen [141] and Boehler [153] (black) and Williams and Jeanloz [52] (black, dashed), Urakawa et al. [150] (green) and Ono et al. [154] (blue) are marked in full lines. Boundaries for FeS III-IV and IV-V are extrapolated (dashed). The Martian areotherm by Fei and Bertka [155], CMB by Stähler et al. [7] and inner core conditions by Rivoldini et al. [142] are drawn in orange. A volume collapse of roughly 5 % from a large volume (red) to an intermediate volume (purple) to a small volume (blue) reported by Urakawa et al. [150] is marked as crosses. Spin states at ambient temperatures from LS (blue) to HS (red) from Rueff et al. [156] are marked as squares. The area of the zoomed-in plot [**Right**] is shown (black, dotted).

5.2 Experimental setup at HED and PETRA III

For this experimental run in IC1 at the HED instrument of the European XFEL, we used the simplified Martian core composition of FeS as the sample. The sample was loaded as a powder in a DAC with diamond anvils with a culet diameter of 300 µm. The sample was put in a Re gasket and was encapsulated in KCl which acted as temperature insulation and to a lower degree as the pressure transmitting medium. In total, three DACs were loaded and pressurised tp 6 GPa, 14 GPa and 25 GPa, which was confirmed using the Raman peak shift of the diamond at the position of the culets. Changes in the electronic spin state of Fe were then monitored during heating

at those pressure points using pulsed X-ray heating at HED as described in CHA 3 using the setup described in CHA 4. For simultaneous XRD measurements, an ePix100 detector was placed downstream of the sample and was calibrated with CeO_2. Three DACs were loaded in the DAC changer in IC1, which was set to pressures below 1×10^{-4} mbar. The beam was set to $12\,996.0 \pm 38.7$ eV photon energy, measured by the HOPG spectrometer in IC1 [100], that was calibrated to Se $K\beta$ and vtc signal. The beam utilized either 455 kHz for cold and 2.2 MHz for heating runs. For heating and probing we used 100 pulses per train. The beam was focused to 8 μm using CRLs, which was confirmed by tungsten rod edge transmission measurements. The beam-drift correction was activated to ensure an inter-train spatially stable beam position on the sample. The photon flux after the optics were controlled using solid attenuators and measured with a calibrated photodiode. The maximum photon flux was 410 μJ on the sample. The Fe spin state was determined using the $K\beta_{1,3}$ emission line measured with four Si(531) analyser crystals. The von Hámos spectrometer was calibrated using the $K\beta_{1,3}$ and vtc signal of a Fe foil. Runs were taken for 1200 to 3000 trains.

Additionally, one DAC was pressurised to 42 GPa, to cover the upper boundary pressures from the Martian core. This DAC was placed in a water-cooled DAC holder on a portable double-sided laser heating table [157] at P01 at Petra III. The beam of the 100 W 1070 nm laser was split and focused to 20 μm on the sample from both sides. The heating-induced emitted light from the sample was measured in a wavelength range from 600 to 800 nm. The temperature was determined by fitting Planck's law of black body radiation to the spectra. With the von Hámos spectrometer described by Albers et al. [89] the Fe $K\beta$ was measured during stepwise laser heating using four Si(110) 30 mm × 110 mm (H x V) analyser crystals cylindrically bent with a 500 mm radius using the third order reflection and a Pilatus 100K detector. To calibrate the detector, elastic lines between 6970 to 7150 eV were collected. The energy resolution is in the sub-eV regime and similar to the von Hámos spectrometer at HED. For the *in-situ* emission measurements, the photon energy of the synchrotron beam was set to an incident energy of 10 keV with a focal size of 8 μm × 8 μm (FWHM, H x V). To ensure laser and X-ray beam alignment on the sample, the sample was spatially measured while keeping the laser position on the sample stable during mapping. Each run was accumulated over several minutes. Additionally, all DACs were XES mapped at P01 to check the electronic spin state of the quenched samples using the same setup and beam settings described above. For phase identification before and after the heating experiments, the samples were mapped using XRD at beamline P02.2.

The beam was set to 42.7 keV with a beam size of $2\,\mu m \times 2\,\mu m$ (FWHM, H x V). The diffraction signal was detected with a PerkinElmer XRD1621 area detector, which was calibrated with CeO_2. At each step of the spatial map, the sample was rotated by $\Omega = \pm\,5°$ during signal collection. Spatially resolved Raman measurements were conducted on one sample, to further confirm the non-Raman active state of the quenched phases. It was decided that further Raman measurements on the remaining DACs were not required.

5.3 In-situ results at HED

5.3.1 X-ray emission from X-ray heated FeS

The XES results for FeS at 6.0 ± 0.5 GPa, 14.00 ± 0.75 GPa and 25 ± 1 GPa are shown in FIG 5.2. The spectra were calibrated and corrected as described in SEC. 2.1.3. IAD values are noise-offset corrected relative to the noise levels.

Compared to the normalised FeS LS and HS references by Rueff et al. [156], a full HS ($S = 2$) is reached for a IAD value of 0.31 and a ΔM1 value of 1.15 eV, as suggested for $FeCO_3$ by Kaa et al. [43], respectively.
At 6.0 ± 0.5 GPa and small pulse energies both the IAD value and ΔM1 show a larger spread and values between 0 to 0.15 and 0 to 0.5 eV, respectively. Due to the low pressure and expected lower temperatures needed to induce an LS-HS transition, we measured at smaller energies with narrow pulse energy increases. With increasing photon flux, we see a drop to a value spread at lower values and a subsequent increase up to a full HS at roughly 150 µJ, where it reaches a plateau and stays on the HS values for the remaining runs with a good agreement for both IAD and ΔM1 values. At 14.00 ± 0.75 GPa the samples are in a complete LS state, indicated by IAD and ΔM1 values below 0.05 and 0.2 eV. With increasing pulse energies above values of 50 µJ both values increase in very good agreement linear to the pulse energy increase. Values connected to a completed HS transition are reached at 200 µJ. With further increase of the pulse energy above 280 µJ, both values drop slightly below the HS values and above 340 µJ the values drop by another step. At all pulse energies, IAD and ΔM1 values are in very good agreement. At 25 ± 1 GPa both values start at a similar low value as at 14.00 ± 0.75 GPa suggesting a (near) complete LS state. Up to 150 µJ both values increase with increasing pulse energy, reaching a maximum mixed spin state of estimated $S = 1.75$. With higher pulse energies, IAD and ΔM1

(a) 6 GPa

(b) 14 GPa

(c) 25 GPa
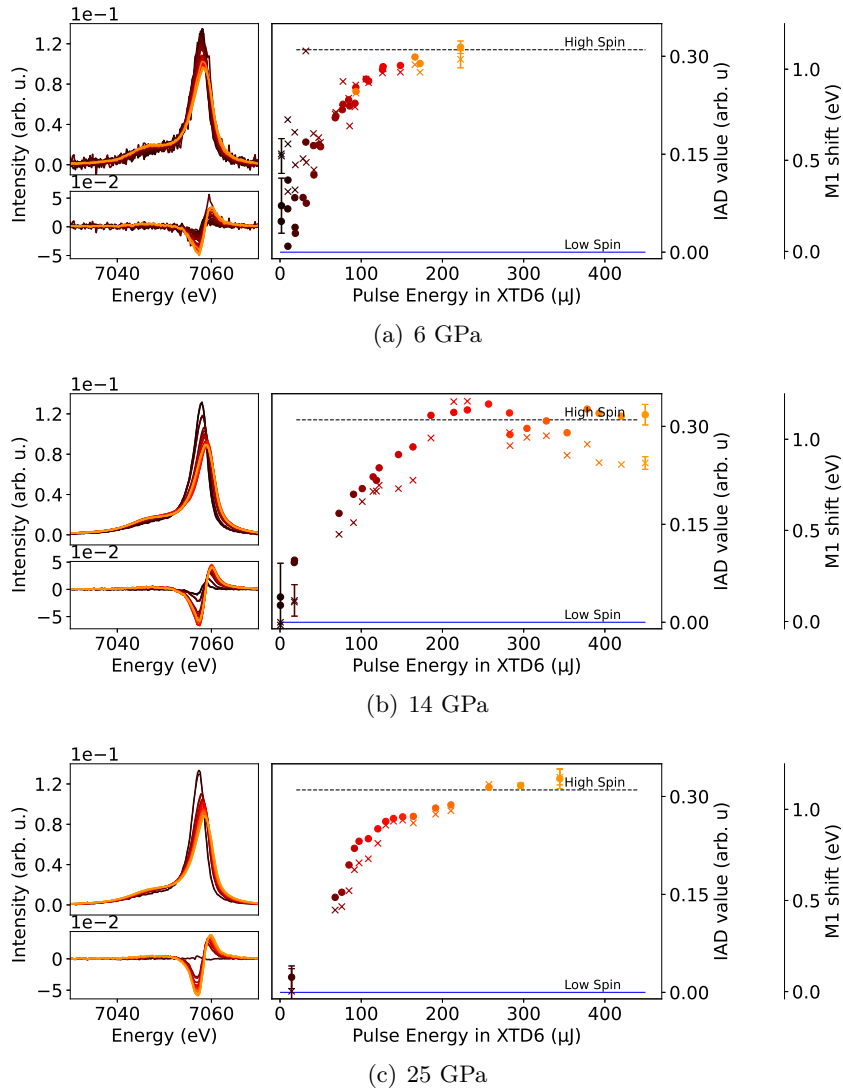
Figure 5.2: XES results for FeS in KCl at different pressures. [**Left, Top**] The Kβ signal and the difference to an LS reference [**Left, Bottom**]. The IAD value and ΔM1 [**Right**] are plotted as a function of the pulse energy on the DAC. LS (blue) and HS ($S = 2$, black, dotted) values from references are marked as lines. For clarity, only example error bars are given for high and low pulse energies. Values are only shown for increasing pulse energies. The complete data sets including values from quenched runs are given in SI FIG. S3.

values further increase and reach a complete HS above 260 μJ where it reaches a plateau with very good agreement for both values.

Assuming the same linear temperature increase with increasing pulse energies, the sample reaches a complete HS state at higher temperatures with increasing pressure.

5.3.2 X-ray diffraction

XRD was measured simultaneously during heating at all three pressure points. This data mainly yields information on the phase contributions in the sample, especially for melt. Due to the very small solid angle covered by the ePix100 detector and large similarities between the different structures of FeS at high pT, qualitative phase identification is difficult. FIG. 5.3 shows selected runs for all three pressure points. The signal was averaged over all trains in each run and was background corrected and loaded in DIOPTAS [13] to integrate the 2D sensor images to a 1D diffraction signal. Diffraction peaks of relevant phases in the given pT range are shown in different colours. The melting contribution to the signal is a broad Gaussian peak between 18 to 24°. Due to the high crystallinity i.e. large sample single crystals, the intensities of all diffraction peaks undergo fluctuations.

At 6 GPa (FIG 5.3 a) the sample is composed of FeS-III and FeS-II at the lowest pulse energies. At a relatively low pulse energy of 10 ± 9 μJ, the FeS-II FeS-III mixture shows a transition to FeS-IV. At the same time, the shift of the KCl peak suggests an increase of (thermal) pressure accompanied by the disappearance of FeS-II. The change to FeS-V is indistinct due to overlaying peaks. It can be argued that at 32 ± 10 μJ FeS-V becomes apparent. Above 86 ± 10 μJ melt can be detected. A single peak at 18° is still unidentified, which could hint towards graphite within the upstream diamond, which is off-focus and subsequently shifted to larger 2θ angles than expected.

At 14 GPa (FIG 5.3 b), the starting material consists of pure FeS-III at low pulse energies. FeS-IV is found above 27 ± 4 μJ and changes into FeS-V above 86 ± 10 μJ, both at higher values compared to the 6 GPa run. A faint melt signature is found above 164 μJ. Above 353 ± 38 μJ the peak shifts to lower 2θ values suggests a partial pressure loss to roughly 6 GPa based on the EOS of KCl. The KCl peak FWHM is increased compared to the other two pressure runs and shows broadening with increasing pulse energy. The peaks of the sample strongly vary in intensity. The same peak at 18° also found at 6 GPa could again hint towards off-axis graphite in the upstream diamond anvil.
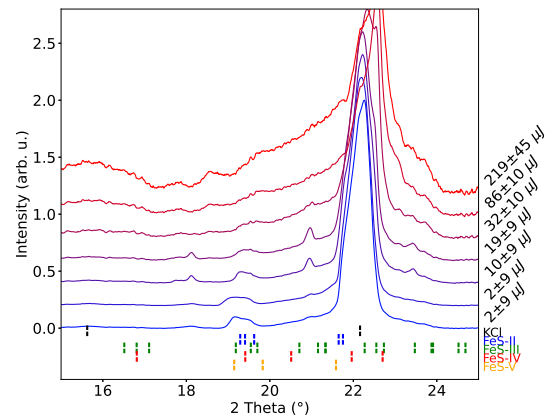
(a) 6 GPa
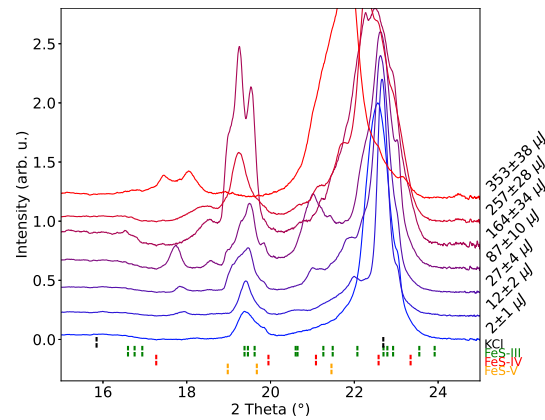
(b) 14 GPa
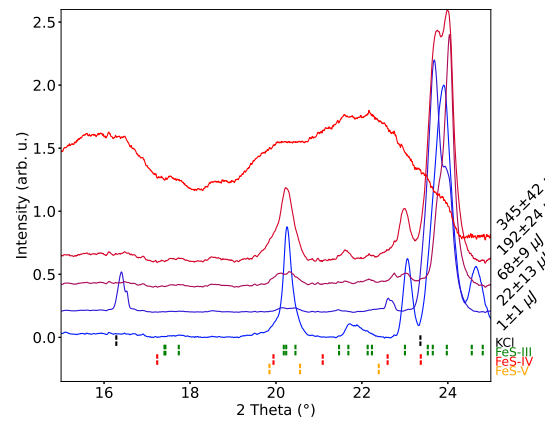
(c) 25 GPa

Figure 5.3: Peak normalised XRD results for X-ray heated FeS at 6 GPa, 14 GPa and 25 GPa for selected runs at different pulse energies. Peaks for KCl (black), FeS-II (blue), FeS-III (green), FeS-IV (red) and FeS-V (orange) are marked in the corresponding colours.

At a pressure of 25 GPa (FIG 5.3 c) the starting sample consists of pure FeS-III, which transforms into FeS-IV at $22 \pm 13\,\mu$J and, in a similiar unclear manner as seen at 6 GPa, further transforms to FeS-V at 68 ± 9 GPa. A clear melting signal is seen at 192 μJ, while above $345 \pm 42\,\mu$J no crystalline sample can be detected. There is no signal of graphite.

Taking the appearance of the phases and the temperatures taken from FIG. 5.1 into account, a linear dependence of the temperature as a function of the pulse energy becomes apparent (see FIG. 5.4). We assume a linear dependency of pulse energy and temperature as shown by Ball et al. [60]. The different pressure points show differing heating efficiencies, likely due to differences in sample and KCl layer thickness.
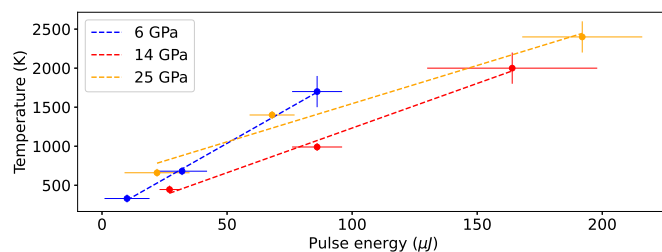
Figure 5.4: Correlation of pulse energy and temperatures for 6 GPa, 14 GPa and 25 GPa by plotting the expected temperature of a phase change against the pulse energy at which the signal of the phase is seen the first time.

5.4 In-situ results at P01

5.4.1 XES

The Fe K$\beta_{1,3}$ signal of FeS at 1450 K, 2000 K, 2200 K and 2500 K and at 42 ± 1 GPa is shown in FIG. 5.5 [left]. The optical spectra taken during heating at 2500 K for upstream and downstream including a fit of Planck's law are shown as well [right].

The IAD value and M1 shift were calculated using a reference measured at ambient temperatures before heating the sample. The sample was heated step-wise from 1450 ± 200 K to a maximum of 2500 ± 200 K. Subsequently, the laser power was continuously increased, while the temperature evened out at 2300 to 2500 K. Up- and downstream measurements are in good agreement within ± 100 K. In FIG. 5.5 and 5.6 it becomes obvious, that even close to melting temperatures, the emission signal does not show any changes in its shape or position, hinting towards a constant LS
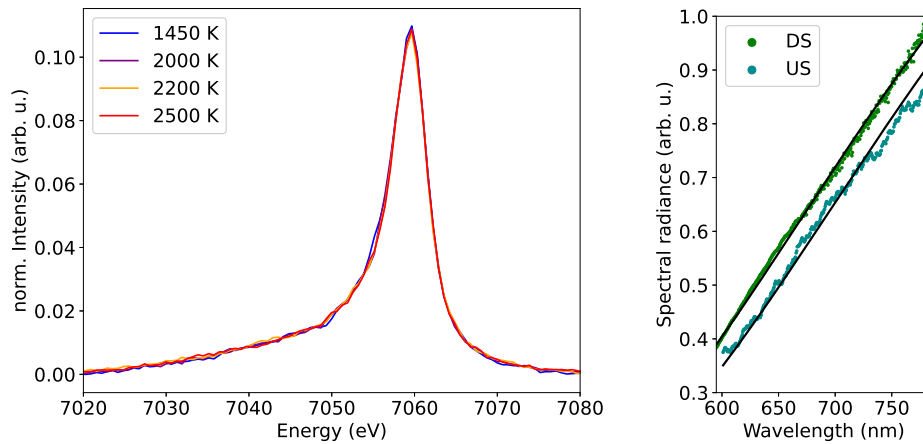
Figure 5.5: [**Left**] FeK$\beta_{1,3}$ signal of FeS at $1450\,\mathrm{K}$, $2000\,\mathrm{K}$, $2200\,\mathrm{K}$ and $2500\,\mathrm{K}$ and at $42\pm1\,\mathrm{GPa}$. [**Right**] The thermal radiation measured up- and downstream was fitted to Planck's law (black).

state throughout the reached temperatures. The trend with increasing temperatures is a flat line for both values. Changes in the M1 shift and IAD value can only be seen due to lower emission intensity, resulting in larger errors. The same results were also achieved for later runs where the sample was measured with a spatial resolution, while keeping the laser heating spot on the sample constant, to ensure alignment of the X-ray beam and the laser. Temperatures above $2500\pm200\,\mathrm{K}$ were not reached. While there were no *in-situ* diffraction measurements, melting or the suggested FeS-VI structure could not be confirmed. However, the heating plateau at the expected melting temperature and pressures near the suggested III-VI transition allows for the assumption, that the sample consists of coexisting FeS-III and -VI up to the melt.

5.5 Ex-situ results

5.5.1 Spatially resolved X-ray emission spectroscopy

The Fe $K\beta_{1,3}$ emission data were analysed using the IAD and ΔM1 value compared to an internal LS spectrum taken from each map. FIG. 5.7 shows the intensity map of both values over $96\,\mu m \times 96\,\mu m$ (H x V) for 6 GPa and 25 GPa and $55\,\mu m \times 55\,\mu m$ (H x V) for the 14 GPa DAC. High-noise data, due to a lack of sample (e.g. on the gasket) was filtered and both IAD and ΔM1 were set to 0 for those cases.

At 6 GPa, shown in FIG. 5.7 (a), both values show a slight increase in the upper parts of the sample. When comparing the signal of this region and a region of lower values, it becomes apparent, that the higher values are due to a slight change and energy shift of the $K\beta$ peak, not by an increase of the electronic spin state indicated by a non-splitting of the $K\beta_{1.3}$ and the $K\beta'$ peak. This hints towards different crystal field strengths caused by different phases.

The similar change in emission line shape and lack of splitting of the $K\beta$ peak can be recognised for the map at 14 GPa shown in FIG. 5.7 (b). The area with increased IAD and ΔM1 values show a similar elongated shape as in the intensity maps a 6 GPa.

At 25 GPa the differences within the sample are less obvious. The intensity map shows a relatively homogeneous emission signal with only slight changes in the maximum intensity of the emission signal due to different noise levels of the signals.
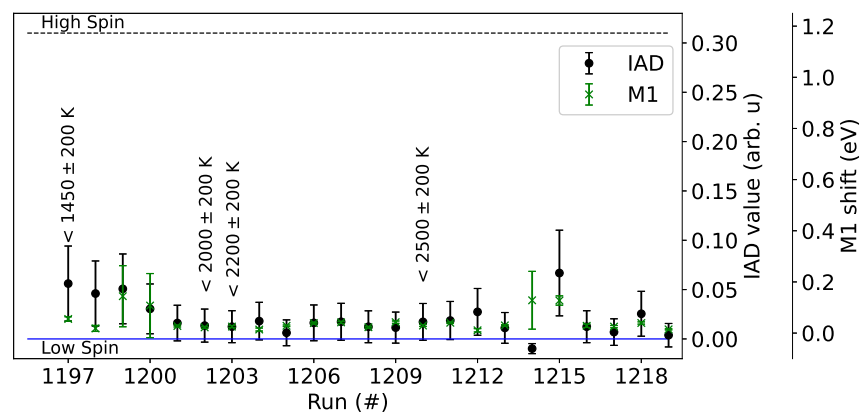
Figure 5.6: Spin state development for XES runs on FeS at 42 ± 1 GPa for various temperatures determined via the M1 shift (green) and IAD value (black) compared to an ambient temperature LS reference. The temperatures of four selected runs are marked. The temperature does not linear increase with increasing run numbers.

All quenched samples show an LS state at ambient temperatures. Increased values in IAD and ΔM1 for the analysis suggest a change in symmetry rather than an increase in the spin state.

(a) 6 GPa
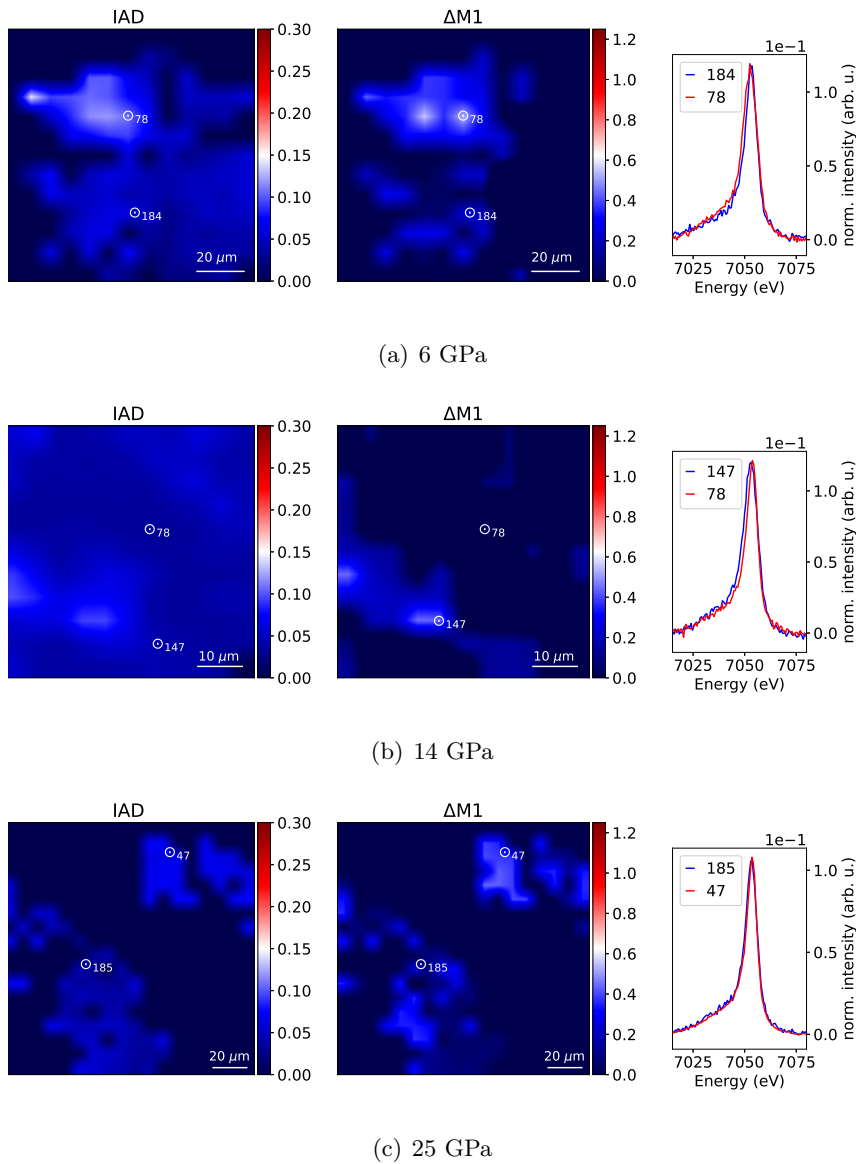
(b) 14 GPa

(c) 25 GPa

Figure 5.7: *Ex-situ* XES intensity maps for IAD [**Left**] and ΔM1 [**Center**] values for 6 GPa, 14 GPa and 25 GPa. Kβ emission spectra for different areas are shown for each pressure point [**Right**].

5.5.2 Spatially resolved X-ray diffraction

Differences in the Fe coordination , hinting towards different phases, were already suggested by slight changes in the emission signal. To identify the potential phase changes in the sample, they were further investigated by spatial measurements of the XRD signal. The distribution of both intensity maps was compared for XES and XRD measurements and was put into relation afterwards by comparing different phases with different IAD and ΔM1 values.

The structures for FeS-II [158], FeS-III [152], FeS-IV [149], FeS-V [159] and FeS-VI [160] were fitted using EoS taken from Ono et al. [154] and Urakawa et al. [150] and references therein. Due to very similar structures in the FeS system, several peaks overlay each other. The pressure determined by Raman spectroscopy was confirmed by the peak shift of KCl by using the EoS [161].

FIG. 5.8 (a) shows the phase distribution of the 6 GPa sample. It consists mainly of co-existing FeS-II and Fes-III. At the top of the sample near the gasket FeS-IV can be found over an area of 30 μm × 20 μm (H x V). On the left edge of the sample near the gasket a 20 μm × 10 μm (H x V) large area of graphite can be found. However, this phase appears at larger 2θ values, due to the off-focus position upstream in the upstream diamond anvil. The position of FeS-IV fits the area of elevated IAD and ΔM1 values sown in FIG. 5.7 (a). FeS-V, even though it was found *in-situ*, was not found in the quenched sample. Additionally, no diffuse background, suggesting quenched melt, can be found.

FIG. 5.8 (b) shows a distribution of FeS-III at 14 GPa with a distinct spot of 20 μm × 10 μm (H x V) size. In this supposed heating spot, FeS-IV and graphite can be found together suggesting a delimited heating spot. As before, the shape and size of the appearance of FeS-IV fits the area of elevated IAD and ΔM1 values suggested in FIG. 5.7 (b). Also as for the sample before, neither FeS-V nor quenched melt can be found. The offset to a higher than expected 2θ value for graphite can also be seen in this sample, suggesting graphite within the upstream diamond anvil.

The sample measured at 25 GPa shows a spatially heterogeneous sample signal within the gasket. It mostly consists, as expected, of FeS-III. The heating spot again is can be identified by a distinct area of FeS-IV accompanied by graphite. Due to the indistinct signal distribution in the XES heating map and the phase distribution, comparing the position of both maps is possible only to a certain extent. Even though having a clear melting signal *in-situ*, no quenched melt or FeS-V is found.

The DAC at 42 GPa shows co-existing FeS-III and FeS-VI. FeS-IV shows the heating spot in the lower part of the sample coexisting with Graphite.

(a) 6 GPa

(b) 14 GPa
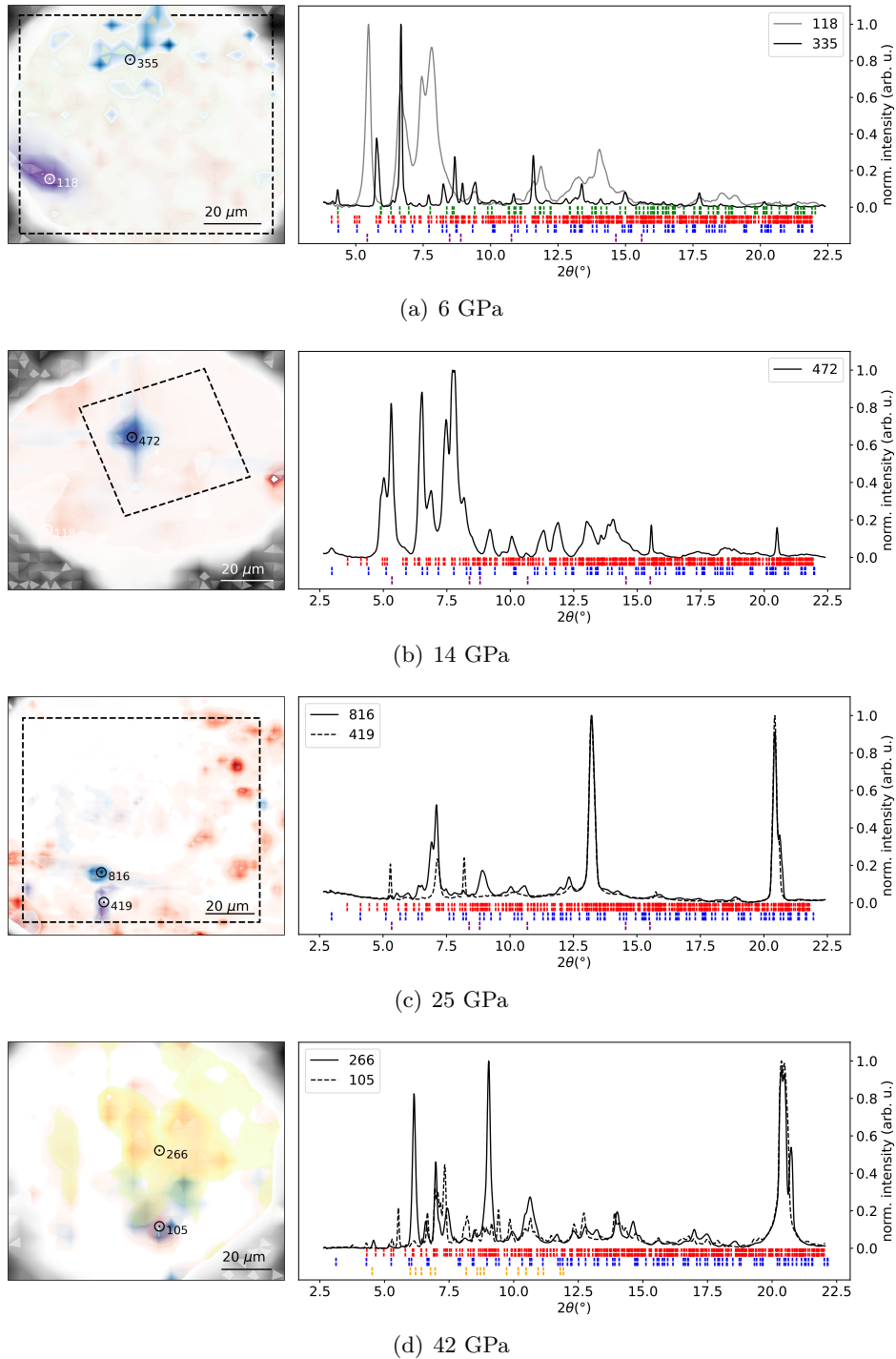
(c) 25 GPa

(d) 42 GPa

Figure 5.8: *Ex-situ* XRD intensity maps for 6 GPa, 14 GPa, 25 GPa and 42 GPa. The intensities of distinct peaks for FeS-II (green), FeS-III (red), FeS-IV (blue), FeS-VI (orange), Graphite (purple) and Re (grey) are shown [**left**]. The positions of XES maps are marked at their assumed position (black, dashed). Various XRD patterns and all peaks of the phases [**right**] are plotted as well.

5.6 Discussion and conclusion

The starting phases in all four DACs fit the phase diagram shown in FIG. 5.1 well with co-existing FeS-II and -III at 6 GPa, FeS-III at 14 to 25 GPa and FeS-III and -VI at 42 GPa. Heating at HED induced a phase change from FeS-III to -IV to -V and subsequent melt. In non of the four DACs FeS-V or melt were found in the quenched state, suggesting a phase change from FeS-V into FeS-IV during cooling and recrystallisation of the melt into FeS. The former suggests that FeS-V is not quenchable under the achieved cooling rates, while the latter would allow assessing of the elemental composition of the eutectic melt of 50 at % Fe and S due to the lack of element depletion in the starting material, i.e. lack of phases with a different element composition in the quenched state (in accordance with Jaisle et al. [61]). This proves FeS as a suitable candidate for probing over several accumulated heating cycles at HED. Using a more realistic composition of the Martian core, i.e. a lower amount of S, would potentially cause a change from a glassy starting material to the melt with varying S content relative to the pressure [162], which would crystallise to a mixture of FeS and metallic Fe. The starting material for the second train, i.e. heating cycle, would be different compared to the first train, making the data interpretation over several accumulated trains more difficult.

In the three DACs at lower pressures, it was possible to induce a heating-driven LS-HS transition. The different heating efficiencies are shown in FIG. 5.4 are due to different thicknesses of the KCl layer and sample thicknesses. Using the linear dependency taken from the phase transitions measured with *in-situ* XRD, it becomes clear, that the spin state change happens between 700 to 1500 K in the FeS-IV and/or -V stability field (see FIG. 5.9). The lack of diffraction peak splitting, caused by volume increase, as can be seen in the $FeCO_3$ system, hints towards a phase transition connected spin change. A complete HS is measured in the FeS-V stability field while one has to take into account that with each train ambient temperature sample and the heating history after each pulse gets probed.

It was not possible to induce an LS-HS transition while laser-heating at 42 GPa. The measured temperatures suggest that the sample was close to the melting phase. The co-existing FeS-III and FeS-IV besides FeS-VI in the quenched sample, suggests that the LS state at the maximum temperature was achieved in FeS-III, -IV, -V and -VI. The complete LS character of the quenched phases measured with *ex-situ* XES showcases the reversibility of the spin state change during cooling. FeS-IV therefore has, as suggested by Urakawa et al. [150], a LS state. The HS phase boundary can be plotted in the pT diagram as $T_{HS}(p) = 30p[\frac{K}{GPa}] + 800[K]$ for $7\,GPa < p <$

25 GPa, which nearly follows the -IV -V phase boundary, further suggesting that the spin transition could be connected to the -IV -V phase boundary. To complete the information about the spin state transition throughout the pT conditions in the Martian core, more experiments in the pressure range 25 to 42 GPa need to be conducted at a temperature above 2500 K.
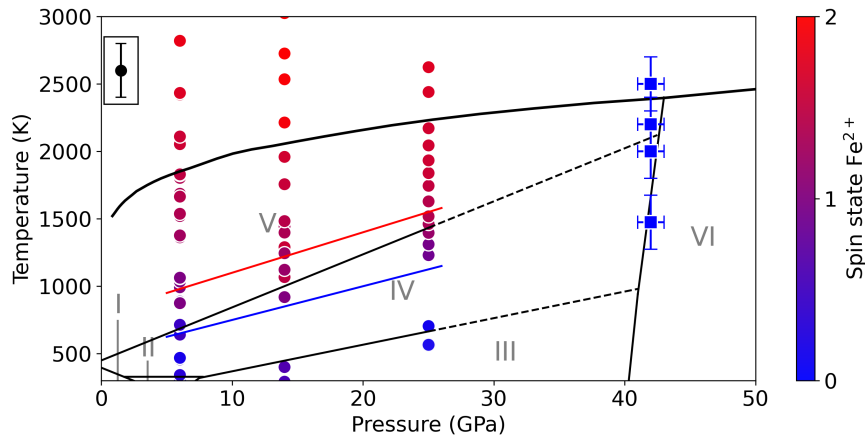
Figure 5.9: Combined spin state data of Fe in the FeS phase diagram for X-ray heated (circles) and laser-heated (squares) runs. Phase boundaries are taken from FIG. 5.1. The temperature reached during X-ray heating was calibrated using *in-situ* XRD data. A change from a complete LS (blue) and a complete HS (red) are plotted as lines. For clarity, the temperature error is given as an example (black).

When we transfer this simplified model to the Martian core, the data set could hint towards a pressure-induced HS-LS transition with increasing depth. This transition, accompanied by a density increase, could explain a possible denser and even solid inner core, as suggested by Stähler et al. [7]. To come to this conclusion, one has to conduct a similar set of experiments with a more realistic composition.

6 Concluding remarks and outlook

This thesis reported on the implementation of a novel approach to enable electronic state measurements, including the spin state and electronic structure, from samples in a DAC and, at a later stage, low-photon NRIXS measurements on free-standing samples, at a hard X-ray FEL facility.

In early 2019, McWilliams [163] initiated the establishment of an experimental station at the HED instrument dedicated to MHz-resolved XRD measurements from a DAC. The team focused on investigating the stability of the diamond anvil cells when exposed to single train measurements, often combined with pulsed IR laser heating. To expand on this work, the project from this thesis aimed to subject the diamond anvils to the energy input of several thousand pulsed X-ray trains, necessary for collecting the Kβ emission signal of Fe from a loaded $FeCO_3$ sample. Despite the peak energy load on the DAC being similar to an experiment in IC2, our proof-of-concept in the vacuum chamber IC1 demonstrated the stability of the diamond anvils when exposed to the pulsed X-ray beam for several minutes. To achieve this, a temporary von Hámos spectrometer with a single Si(531) analyser crystal ($110\,mm \times 30\,mm$ (H x V)) was implemented. Our experiment used $2.2\,MHz$ and 10 pulses per train and resulted in an electronic spin state change in $FeCO_3$ at $51\,GPa$, using only a fraction of the available pulse energy. This was measured by changes in the Kβ emission line and by the splitting of the X-ray diffraction peaks, which were collected at $10\,Hz$ using a detector in transmission of the sample. However, when exposed to higher pulse energies, the sample experienced melting, confirmed by the XRD signal. Further analysis showed heat damage on the upstream anvil in the form of an amorphous graphite-like carbon signal within the diamond. This can affect the stability of the anvil and could suggest a reduced likelihood of reusing the diamond after an experiment. As a secondary result, our experiment revealed a complex phase behaviour in the Fe-C-O system when multiple heating cycles are applied.

Several shortcomings of the spectrometer setup were identified during the first experiment and needed to be improved. The main improvements necessary were a higher efficiency, reducing the setup broadening function, optimising the sample exchange in the vacuum chamber and optimising the approach to the X-ray beam setup. With

the company JJ-Xray, we agreed on a vacuum compatible 4x1 crystal positioning unit, allowing for crystal dimensions of up to $110\,\text{mm} \times 20\,\text{mm}$ (H x V). By the slightly smaller crystals, compared to the proof-of-principle experiment, each crystal provided a smaller energy window but allowed the space for placing four crystals in one column and thus increasing the efficiency of the spectrometer. Three 2-phase stepper motors on each crystal plate control the yaw, pitch and roll. Two pairs of XYZ-stages controlled the positioning of the crystal unit and the detector relative to the sample. All motors were connected to the Karabo controlling system [164]. This flexibility and degrees of freedom allowed for a quasi-perfect focusing of the diffracted signal on the detector, reducing the fraction of the geometric component to the setup broadening to a minimum. The DAC exchanger, consisting of a rotation stage and three arms holding a BX90-RD each, enabled to place three different samples per pump-vent procedure in IC1, optimising the usage of the beamtime. With this new setup, we tested several measuring schemes. Increasing the pulses per train from 10 to 100, the emission intensity increased significantly. At the same time, the inter-train temperature was easier to interpret due to the relatively stable temperature after the first pulses in each train.

This beam setting, using 100 pulses per train, was tested with the final von Hámos spectrometer on FeS at three different pressures between 6 to 25 GPa. In all three cases Fe is in a LS state and changed to a complete HS upon pulse energy increase. A phase change from FeS-III to -IV to -V was induced. In all three cases melting temperatures were reached. The LS-HS change can be placed in the pT space of the FeS-IV to -V phase transition. In an additional experiment at the beamline P01 at Petra III using a double-sided laser heating system, FeS at 42 GPa was heated up to melting temperatures, showing a constant LS state throughout all increased temperatures, potentially connected to the FeS-IV phase. The extrapolated data sets from all four pressure points suggest a pressure-induced HS-LS transition within the pT range of the Martian core. The results yield information about the interior of smaller terrestrial planets. A similar result for a sample with a composition closer to what is expected in the Martian core, would allow us to make a statement about a transition from the molten outer core to a potentially more dense and even solid inner core.

Other measuring schemes tested are NRIXS on a polycrystalline diamond plate at ambient pressure using a monochromatic beam with a Si(311) double bounce monochromator. In transmission geometry, the energy-loss spectra for all four crystals, providing different momentum transfers each, were collected between 0 to 100 eV. The resulting q depending plasmon excitation signal could provide sufficient intensity

to extract information about the valence electron levels of the diamond lattice. When combined with the continuous movement of the FSSS and a larger sample, this kind of measurement can be conducted on various samples by collecting over several minutes in a 10 Hz manner. Measurements of the XRS signal, i.e. K edge of the same diamond plate, show the limit of the efficiency of the setup. While the energy resolution is viable, these measurements need to be conducted with a seeded beam, providing a significantly higher photon flux for a monochromatic beam.

The setup and its current applications expand to the highly efficient HAPG spectrometer [100] and the high energy resolution diced crystal analysers [123] already implemented in IC1, with a higher energy resolution than the former and a higher efficiency than the latter. While it is already available for user experiments, there are plenty of potentially novel approaches utilizing the setup, that can be tested in the future. The already mentioned seeded beam will allow for NRIXS measurements in the tens of eV energy loss range with high-quality data from free-standing samples with a simple X-ray probe or in combination with a pump laser source. The data also suggests that single pulse Kα and, when further improving the DAC loading for measurements in near-90° scattering angle, by e.g. using X-ray transparent gasket materials, Kβ measurements from DACs are possible. This opens up several new possibilities such as pump-probe experiments in the femtosecond timescale, which would allow for electronic spin state measurements as a function of the delay between the laser pump and the X-ray probe. This sDAC approach is already available at laser facilities [165, 166, 167] and is currently prepared for the laser sources available at HED. Pulse-resolved measurements from a DAC would also allow for highly time-efficient measurements through a large pT space, when combined with a MHz-resolved detector, as it is already routinely done at IC2 for XRD. Potentially a single pulse could probe from ambient temperatures above melting. In the near future, an optical path to a streak camera for radiometric measurements of the thermal radiation, allowing for *in-situ* temperature measurements.

In conclusion, this setup and the continued effort and improvements at HED allow us to access new fields of exciting new possibilities to study the electronic state of condensed matter at extreme conditions up to the warm dense matter regime.

Appendix

Run #	XGM_{up} in µJ	XGM_{do} in µJ	# of trains
179[1]	713.2 ± 10.3	51.9 ± 2.0	3185
189[1]	687.8 ± 9.3	78.4 ± 2.3	2243
190[2]	760.6 ± 12.3	11.2 ± 1.7	3091
191[2]	793.8 ± 8.3	11.4 ± 1.7	3062
193[2]	778.6 ± 12.8	18.1 ± 1.8	2778
194[2]	775.7 ± 6.8	18.0 ± 1.8	2901
195[2]	776.4 ± 11.3	33.6 ± 2.1	3456
196[2]	777.2 ± 10.7	33.6 ± 1.9	2651
197[2]	790.3 ± 11.0	34.0 ± 1.8	3469
198[2]	772.3 ± 12.6	33.2 ± 2.0	4019
199[2]	790.5 ± 7.1	51.8 ± 1.9	3330
202[2]	798.4 ± 9.0	52.3 ± 2.0	3012
204[2]	787.6 ± 8.6	72.7 ± 2.0	3002
206[2]	777.0 ± 11.6	71.8 ± 2.4	2955
207[2]	781.0 ± 10.7	88.7 ± 2.2	3033
208[2]	780.1 ± 9.3	144.4 ± 3.9	3002
209[2]	752.1 ± 3.0	176.5 ± 6.8	3005
210[2]	765.5 ± 18.7	200.7 ± 5.3	3040
211[2]	788.0 ± 12.5	255.2 ± 4.5	3122

Table S1: Mean pulse energy over all trains for each conducted run including the standard deviation and amount of trains per run. Values from XGM_{up} are measured before the attenuation of the beam. Pulse energies in XGM_{do} correspond to the attenuated beam.

[a]Rep. rate 455 kHz
[b]Rep. rate 2.2 MHz
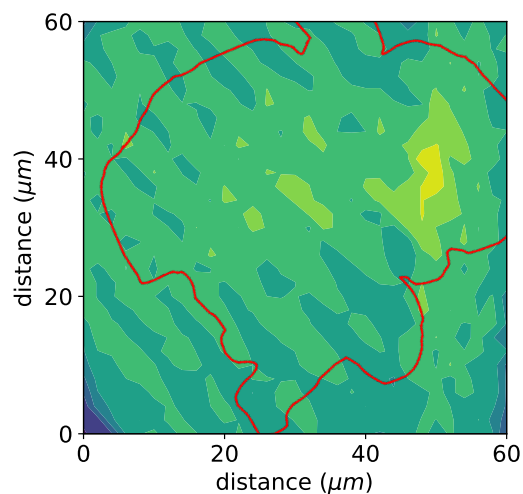
Figure S1: *Ex-situ* XRD background intensity map for the $FeCO_3$ sample. Higher intensities (yellow) potentially mark an increase in the fraction of amorphous signal to the background. The position alignes with the heating spot during the experiment.
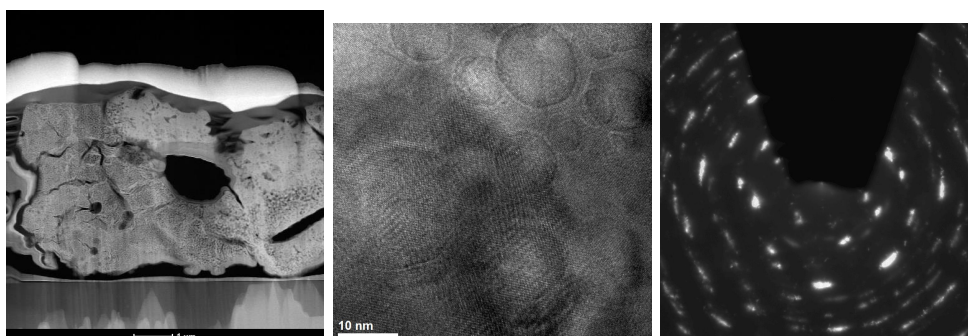
Figure S2: [**Left**] High resolution SEM image of the TEM foil cut from a heated grain and recovered to ambient pressures. [**Center**] TEM measurement of the same foil, showing ring like structures in the crystal lattice. This could hint toward outgasing during pressure release. [**Right**] Electron diffraction image of the same foil, showing Fe_2O_3.
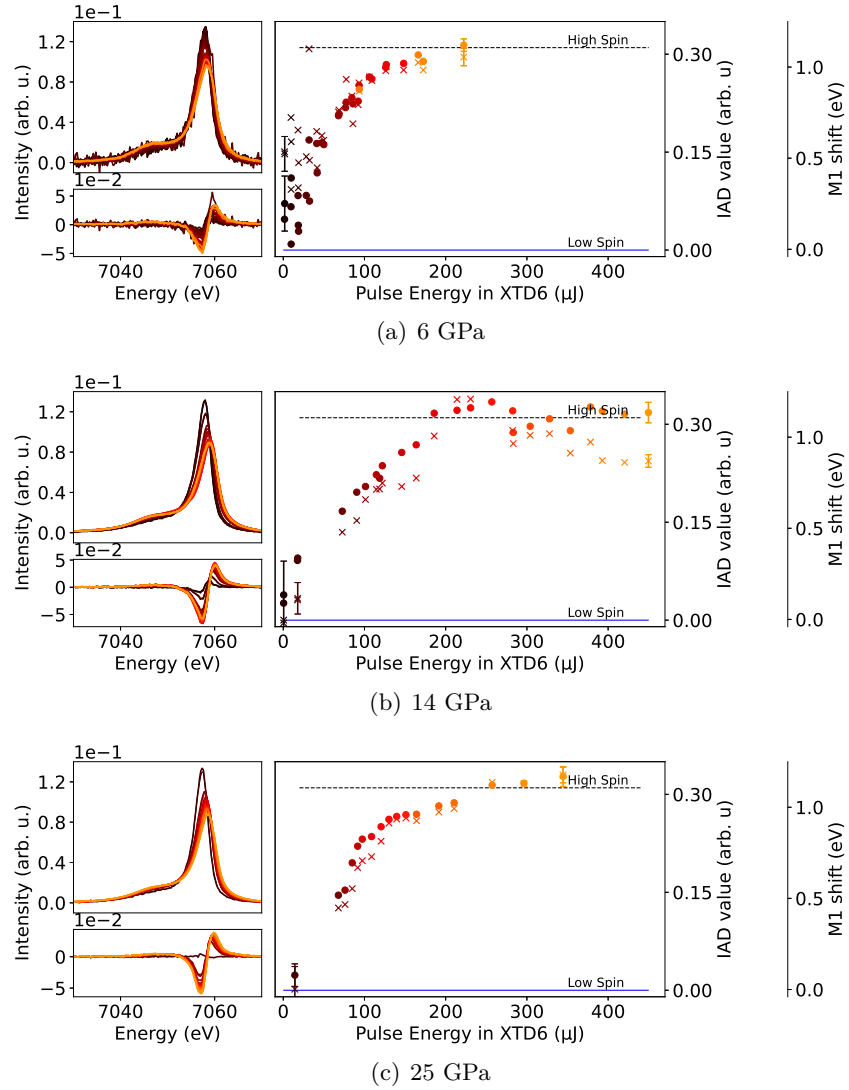
Figure S3: Complete XES results for FeS in KCl at different pressures. [**Left, Top**] The Kβ signal and the difference to an LS reference [**Left, Bottom**]. The IAD value and ΔM1 [**Right**] are plotted as a function of the pulse energy on the DAC. LS (blue) and HS ($S = 2$, black, dotted) values from references are marked as lines.

(hkl)	531	511	333	444	533
60°					
peak reflectivity	0.60	0.65	0.73	0.67	0.48
FWHM (meV)	165.44	149.43	88.06	221.48	226.82
R (µrad)	30.39	33.15	26.24	39.37	29.54
70°					
peak reflectivity	0.58	0.63	0.71	0.66	0.47
FWHM (meV)	122.75	133.42	80.05	178.79	181.45
R (µrad)	41.73	46.01	37.31	53.75	40.41
80°					
peak reflectivity	0.57	0.46	0.70	0.65	0.460
FWHM (meV)	114.74	146.76	77.38	146.76	146.76
R (µrad)	79.23	96.06	72.40	101.73	76.52

Table S2: Peak reflectivity, FWHM and integrated reflectivity R for Si(531), Si(333) and Si(444) at Bragg angles of 60°, 70° and 70°, calculated from the rocking curves (see FIG.).

Bibliography

[1] Chiara Anzolini et al. "Depth of formation of super-deep diamonds: Raman barometry of $CaSiO_3$-walstromite inclusions". In: *American Mineralogist* 103.1 (Jan. 2018), pp. 69–74. DOI: 10.2138/am-2018-6184. URL: https://doi.org/10.2138/am-2018-6184.

[2] Frank E. Brenker et al. "Origin, properties, and structure of breyite: The second most abundant mineral inclusion in super-deep diamonds". In: *American Mineralogist* 106.1 (Jan. 2021), pp. 38–43. DOI: 10.2138/am-2020-7513. URL: https://doi.org/10.2138/am-2020-7513.

[3] Matteo Alvaro, Ross John Angel, and Fabrizio Nestola. "Inclusions in diamonds probe Earth's chemistry through deep time". In: *Communications Chemistry* 5.1 (Jan. 2022). DOI: 10.1038/s42004-022-00627-1. URL: https://doi.org/10.1038/s42004-022-00627-1.

[4] W. B. Banerdt et al. "The InSight Mission for 2018". In: *48th Annual Lunar and Planetary Science Conference*. Lunar and Planetary Science Conference. Mar. 2017, 1896, p. 1896.

[5] Ingrid Daubar et al. "Impact-Seismic Investigations of the InSight Mission". In: *Space Science Reviews* 214.8 (Dec. 2018). DOI: 10.1007/s11214-018-0562-x. URL: https://doi.org/10.1007/s11214-018-0562-x.

[6] Jessica C. E. Irving et al. "First observations of core-transiting seismic phases on Mars". In: *Proceedings of the National Academy of Sciences* 120.18 (Apr. 2023). DOI: 10.1073/pnas.2217090120. URL: https://doi.org/10.1073/pnas.2217090120.

[7] Simon C Stähler et al. "Seismic detection of the martian core". en. In: *Science* 373.6553 (July 2021), pp. 443–448.

[8] Alberto G. Fairén. "Interiors and Surfaces of Terrestrial Planets and Major Satellites". In: *Handbook of Exoplanets*. Springer International Publishing, 2017, pp. 1–25. DOI: 10.1007/978-3-319-30648-3_43-1. URL: https://doi.org/10.1007/978-3-319-30648-3_43-1.

[9]   J. Meza-Galvez et al. "Thermomechanical response of thickly tamped targets and diamond anvil cells under pulsed hard X-ray irradiation". In: *Journal of Applied Physics* 127.19 (May 2020), p. 195902. DOI: 10.1063/1.5141360. URL: https://doi.org/10.1063/1.5141360.

[10]   Winfried Schülke. *Electron dynamics by inelastic X-ray scattering.* Oxford Series on Synchrotron Radiation. London, England: Oxford University Press, June 2007.

[11]   Stefan P Hau-Riege. *High-intensity X-rays - interaction with matter.* en. Weinheim, Germany: Wiley-VCH Verlag, Oct. 2011.

[12]   P P Willmott. *An Introduction to Synchrotron Radiation - Techniques and Applications.* 2nd ed. Hoboken, NJ: Wiley-Blackwell, Apr. 2019.

[13]   Clemens Prescher and Vitali B Prakapenka. "DIOPTAS: a program for reduction of two-dimensional X-Ray diffraction data and data exploration". In: *High Press. Res.* 35.3 (July 2015), pp. 223–230.

[14]   A.P. Hammersley, S.O. Svensson, and A. Thompson. "Calibration and correction of spatial distortions in 2D detector systems". In: *Nuclear Instruments and Methods in Physics Research Section A: Accelerators, Spectrometers, Detectors and Associated Equipment* 346.1-2 (July 1994), pp. 312–321. DOI: 10.1016/0168-9002(94)90720-x. URL: https://doi.org/10.1016/0168-9002(94)90720-x.

[15]   B E Warren. *X-Ray Diffraction.* en. Dover Books on Physics. Mineola, NY: Dover Publications, June 1990.

[16]   E. R. Pike and J. Ladell. "The Lorentz factor in powder diffraction". In: *Acta Crystallographica* 14.1 (Jan. 1961), pp. 53–54. DOI: 10.1107/s0365110x61000085. URL: https://doi.org/10.1107/s0365110x61000085.

[17]   B B He. *Two-dimensional X-ray diffraction.* en. Hoboken, NJ: Wiley-Blackwell, July 2009.

[18]   H A Kramers and W Heisenberg. "Über die Streuung von Strahlung durch Atome". de. In: *Z. Phys.* 31.1 (Feb. 1925), pp. 681–708.

[19]   F. Calegari et al. "Ultrafast electron dynamics in phenylalanine initiated by attosecond pulses". In: *Science* 346.6207 (Oct. 2014), pp. 336–339. DOI: 10.1126/science.1254061. URL: https://doi.org/10.1126/science.1254061.

[20]   Léon Van Hove. "Correlations in Space and Time and Born Approximation Scattering in Systems of Interacting Particles". In: *Physical Review* 95.1 (July 1954), pp. 249–262. DOI: 10.1103/physrev.95.249. URL: https://doi.org/10.1103/physrev.95.249.

[21]   Galambosi Szabolcs. "Electronic excitations in solids studied using inelastic x-ray scattering". dissertation. University of Helsinki, 2007. URL: https://helda.helsinki.fi/handle/10138/23292.

[22]   B.L. Henke, E.M. Gullikson, and J.C. Davis. "X-Ray Interactions: Photoabsorption, Scattering, Transmission, and Reflection at E = 50-30.000 eV, Z = 1-92". In: *Atomic Data and Nuclear Data Tables* 54.2 (July 1993), pp. 181–342. DOI: 10.1006/adnd.1993.1013. URL: https://doi.org/10.1006/adnd.1993.1013.

[23]   Pieter Glatzel and Uwe Bergmann. "High resolution 1s core hole X-ray spectroscopy in 3d transition metal complexes - electronic and structural information". In: *Coordination Chemistry Reviews* 249.1-2 (Jan. 2005), pp. 65–95. DOI: 10.1016/j.ccr.2004.04.011. URL: https://doi.org/10.1016/j.ccr.2004.04.011.

[24]   György Vankó et al. "Probing the 3d Spin Momentum with X-Ray Emission Spectroscopy: The Case of Molecular-Spin Transitions". In: *The Journal of Physical Chemistry B* 110.24 (May 2006), pp. 11647–11653. DOI: 10.1021/jp0615961. URL: https://doi.org/10.1021/jp0615961.

[25]   Sara Lafuerza et al. "Chemical Sensitivity of Kβ and Kα X-Ray Emission from a Systematic Investigation of Iron Compounds". In: *Inorganic Chemistry* 59.17 (Aug. 2020), pp. 12518–12535. DOI: 10.1021/acs.inorgchem.0c01620. URL: https://doi.org/10.1021/acs.inorgchem.0c01620.

[26]   J. B. Jones and D. S. Urch. "Metal–ligand bonding in some vanadium compounds: a study based on X-ray emission data". In: *Journal of the Chemical Society, Dalton Transactions* 19 (1975), p. 1885. DOI: 10.1039/dt9750001885. URL: https://doi.org/10.1039/dt9750001885.

[27]   Erik Gallo and Pieter Glatzel. "Valence to Core X-ray Emission Spectroscopy". In: *Advanced Materials* 26.46 (May 2014), pp. 7730–7746. DOI: 10.1002/adma.201304994. URL: https://doi.org/10.1002/adma.201304994.

[28]   G. Spiekermann et al. "Persistent Octahedral Coordination in Amorphous GeO_2 Up to 100 GPa by Kβ'' X-Ray Emission Spectroscopy". In: *Phys. Rev.*

X 9 (1 Feb. 2019), p. 011025. DOI: `10.1103/PhysRevX.9.011025`. URL: `https://link.aps.org/doi/10.1103/PhysRevX.9.011025`.

[29] Johannes M. Kaa et al. "A von Hámos spectrometer for diamond anvil cell experiments at the High Energy Density Instrument of the European X-ray Free-Electron Laser". In: *Journal of Synchrotron Radiation* 30.4 (May 2023). DOI: `10.1107/s1600577523003041`. URL: `https://doi.org/10.1107/s1600577523003041`.

[30] Christian Albers et al. "High-efficiency X-ray emission spectroscopy of cold-compressed Fe_2O_3 and laser-heated pressurized $FeCO_3$ using a von Hámos spectrometer". In: *J. Anal. At. Spectrom.* (2023). DOI: `10.1039/D3JA00014A`. URL: `http://dx.doi.org/10.1039/D3JA00014A`.

[31] Henrik Enquist et al. "FemtoMAX – an X-ray beamline for structural dynamics at the short-pulse facility of MAX IV". In: *Journal of Synchrotron Radiation* 25.2 (Feb. 2018), pp. 570–579. DOI: `10.1107/s1600577517017660`. URL: `https://doi.org/10.1107/s1600577517017660`.

[32] W. Decking et al. "A MHz-repetition-rate hard X-ray free-electron laser driven by a superconducting linear accelerator". In: *Nature Photonics* 14.6 (May 2020), pp. 391–397. DOI: `10.1038/s41566-020-0607-z`. URL: `https://doi.org/10.1038%2Fs41566-020-0607-z`.

[33] Ulf Zastrau et al. "The High Energy Density Scientific Instrument at the European XFEL". In: *Journal of Synchrotron Radiation* 28.5 (Aug. 2021), pp. 1393–1416. DOI: `10.1107/s1600577521007335`. URL: `https://doi.org/10.1107/s1600577521007335`.

[34] Y. Li et al. "Magnetic Measurement Techniques for the Large-Scale Production of Undulator Segments for the European XFEL". In: *Synchrotron Radiation News* 28.3 (May 2015), pp. 23–28. DOI: `10.1080/08940886.2015.1037679`. URL: `https://doi.org/10.1080/08940886.2015.1037679`.

[35] G. Margaritondo and Primoz Rebernik Ribic. "A simplified description of X-ray free-electron lasers". In: *Journal of Synchrotron Radiation* 18.2 (Jan. 2011), pp. 101–108. DOI: `10.1107/s090904951004896x`. URL: `https://doi.org/10.1107/s090904951004896x`.

[36] Ichiro Inoue et al. "Generation of narrow-band X-ray free-electron laser via reflection self-seeding". In: *Nature Photonics* 13.5 (Mar. 2019), pp. 319–322. DOI: `10.1038/s41566-019-0365-y`. URL: `https://doi.org/10.1038/s41566-019-0365-y`.

[37] Thomas Tschentscher et al. "Photon Beam Transport and Scientific Instruments at the European XFEL". In: *Applied Sciences* 7.6 (June 2017), p. 592. DOI: 10.3390/app7060592. URL: https://doi.org/10.3390/app7060592.

[38] Theophilos Maltezopoulos et al. "Operation of X-ray gas monitors at the European XFEL". In: *Journal of Synchrotron Radiation* 26.4 (June 2019), pp. 1045–1051. DOI: 10.1107/s1600577519003795. URL: https://doi.org/10.1107/s1600577519003795.

[39] Earl F. O'Bannon et al. "Contributed Review: Culet diameter and the achievable pressure of a diamond anvil cell: Implications for the upper pressure limit of a diamond anvil cell". In: *Review of Scientific Instruments* 89.11 (Nov. 2018), p. 111501. DOI: 10.1063/1.5049720. URL: https://doi.org/10.1063/1.5049720.

[40] Saiana Khandarkhaeva et al. "Testing the performance of secondary anvils shaped with focused ion beam from the single-crystal diamond for use in double-stage diamond anvil cells". In: *Review of Scientific Instruments* 93.3 (Mar. 2022), p. 033904. DOI: 10.1063/5.0071786. URL: https://doi.org/10.1063/5.0071786.

[41] Lin-Gun Liu, Taro Takahashi, and William A. Bassett. "Effect of pressure and temperature on the lattice parameters of rhenium". In: *Journal of Physics and Chemistry of Solids* 31.6 (June 1970), pp. 1345–1351. DOI: 10.1016/0022-3697(70)90138-1. URL: https://doi.org/10.1016/0022-3697(70)90138-1.

[42] Christian Albers et al. "Fe^{3+}-hosting carbon phases in the deep Earth". In: *Phys. Rev. B* 105 (8 Feb. 2022), p. 085155. DOI: 10.1103/PhysRevB.105.085155. URL: https://link.aps.org/doi/10.1103/PhysRevB.105.085155.

[43] Johannes M Kaa et al. "Structural and electron spin state changes in an X-Ray heated iron carbonate system at the Earth's lower mantle pressures". en. In: *Phys. Rev. Research* 4.3 (July 2022).

[44] K. Syassen. "Ruby under pressure". In: *High Pressure Research* 28.2 (June 2008), pp. 75–126. DOI: 10.1080/08957950802235640. URL: https://doi.org/10.1080/08957950802235640.

[45] Agnès Dewaele et al. "Compression curves of transition metals in the Mbar range: Experiments and projector augmented-wave calculations". In: *Physical*

Review B 78.10 (Sept. 2008). DOI: `10.1103/physrevb.78.104102`. URL: `https://doi.org/10.1103/physrevb.78.104102`.

[46] Yuichi Akahama and Haruki Kawamura. "Pressure calibration of diamond anvil Raman gauge to 310 GPa". In: *Journal of Applied Physics* 100.4 (Aug. 2006), p. 043516. DOI: `10.1063/1.2335683`. URL: `https://doi.org/10.1063/1.2335683`.

[47] Francis Birch. "Finite Elastic Strain of Cubic Crystals". In: *Physical Review* 71.11 (June 1947), pp. 809–824. DOI: `10.1103/physrev.71.809`. URL: `https://doi.org/10.1103/physrev.71.809`.

[48] James D. McHardy et al. "On the creation of thermal equations of state for use in Dioptas". In: *High Pressure Research* (Mar. 2023), pp. 1–18. DOI: `10.1080/08957959.2023.2187294`. URL: `https://doi.org/10.1080/08957959.2023.2187294`.

[49] Tomoo Katsura and Yoshinori Tange. "A Simple Derivation of the Birch–Murnaghan Equations of State (EOSs) and Comparison with EOSs Derived from Other Definitions of Finite Strain". In: *Minerals* 9.12 (Nov. 2019), p. 745. DOI: `10.3390/min9120745`. URL: `https://doi.org/10.3390/min9120745`.

[50] Orson L. Anderson. "An experimental high-temperature thermal equation of state bypassing the Grüneisen parameter". In: *Physics of the Earth and Planetary Interiors* 22.3-4 (June 1980), pp. 165–172. DOI: `10.1016/0031-9201(80)90029-1`. URL: `https://doi.org/10.1016/0031-9201(80)90029-1`.

[51] A. B. P. Lever. "The Crystal Field Splitting Parameter Dq: Calculation and Significance". In: *Werner Centennial*. AMERICAN CHEMICAL SOCIETY, Jan. 1967, pp. 430–451. DOI: `10.1021/ba-1967-0062.ch029`. URL: `https://doi.org/10.1021/ba-1967-0062.ch029`.

[52] Quentin Williams and Raymond Jeanloz. "Melting relations in the iron-sulfur system at ultra-high pressures: Implications for the thermal state of the Earth". In: *Journal of Geophysical Research* 95.B12 (1990), p. 19299. DOI: `10.1029/jb095ib12p19299`. URL: `https://doi.org/10.1029/jb095ib12p19299`.

[53] Martin v Allmen and Andreas Blatter. *Laser-beam interactions with materials*. en. 2nd ed. Springer series in materials science. Berlin, Germany: Springer, Aug. 1995.

[54] R. Stewart McWilliams et al. "Opacity and conductivity measurements in noble gases at conditions of planetary and stellar interiors". In: *Proceedings of the National Academy of Sciences* 112.26 (June 2015), pp. 7925–7930. DOI: 10.1073/pnas.1421801112. URL: https://doi.org/10.1073/pnas.1421801112.

[55] Alexander F. Goncharov et al. "X-ray diffraction in the pulsed laser heated diamond anvil cell". In: *Review of Scientific Instruments* 81.11 (Nov. 2010), p. 113902. DOI: 10.1063/1.3499358. URL: https://doi.org/10.1063/1.3499358.

[56] Zuzana Konôpková et al. "Laser heating system at the Extreme Conditions Beamline, P02.2, PETRA III". In: *Journal of Synchrotron Radiation* 28.6 (Oct. 2021), pp. 1747–1757. DOI: 10.1107/s1600577521009231. URL: https://doi.org/10.1107/s1600577521009231.

[57] Zuzana Konôpková et al. "Direct measurement of thermal conductivity in solid iron at planetary core conditions". In: *Nature* 534.7605 (June 2016), pp. 99–101. DOI: 10.1038/nature18009. URL: https://doi.org/10.1038/nature18009.

[58] Dion L. Heinz and Raymond Jeanloz. "Measurement of the melting curve of $Mg_{0.9}Fe_{0.1}SiO_3$ at lower mantle conditions and its geophysical implications". In: *Journal of Geophysical Research: Solid Earth* 92.B11 (Oct. 1987), pp. 11437–11444. DOI: 10.1029/jb092ib11p11437. URL: https://doi.org/10.1029/jb092ib11p11437.

[59] M. O. Krause and J. H. Oliver. "Natural widths of atomic K and L levels, K X-ray lines and several KLL Auger lines". In: *Journal of Physical and Chemical Reference Data* 8.2 (Apr. 1979), pp. 329–338. DOI: 10.1063/1.555595. URL: https://doi.org/10.1063/1.555595.

[60] Orianna B. Ball et al. "Dynamic Optical Spectroscopy and Pyrometry under Optical and X-ray Laser Heating at European XFEL". To be published. 2023.

[61] Nicolas Jaisle et al. "Reproducing and interpreting MHz Free Electron Laser X-ray Diffraction experiments by Finite Element Modeling". To be published. 2023.

[62] Ian R Lewis and Howell Edwards. *Handbook of Raman spectroscopy*. Practical Spectroscopy. Boca Raton, FL: CRC Press, Aug. 2001.

[63] Ray Egerton. *Physical principles of electron microscopy*. 1st ed. New York, NY: Springer, May 2008.

[64] H.-P. Liermann et al. "The Extreme Conditions Beamline P02.2 and the Extreme Conditions Science Infrastructure at PETRA III". In: *Journal of Synchrotron Radiation* 22.4 (June 2015), pp. 908–924. DOI: 10.1107/s1600577515005937. URL: https://doi.org/10.1107/s1600577515005937.

[65] Beth N. Orcutt, Isabelle Daniel, and Rajdeep Dasgupta, eds. *Deep Carbon.* Cambridge University Press, Oct. 2019. DOI: 10.1017/9781108677950. URL: https://doi.org/10.1017/9781108677950.

[66] B. Lavina et al. "Siderite at lower mantle conditions and the effects of the pressure-induced spin-pairing transition". In: *Geophysical Research Letters* 36.23 (Dec. 2009). DOI: 10.1029/2009gl039652. URL: https://doi.org/10.1029/2009gl039652.

[67] J. Liu et al. "Thermal equation of state and spin transition of magnesiosiderite at high pressure and temperature". In: *American Mineralogist* 99.1 (Jan. 2014), pp. 84–93. DOI: 10.2138/am.2014.4553. URL: https://doi.org/10.2138/am.2014.4553.

[68] Valerio Cerantola et al. "High-pressure spectroscopic study of siderite ($FeCO_3$) with a focus on spin crossover". In: *American Mineralogist* 100.11-12 (Nov. 2015), pp. 2670–2681. DOI: 10.2138/am-2015-5319. URL: https://doi.org/10.2138/am-2015-5319.

[69] Valerio Cerantola et al. "Stability of iron-bearing carbonates in the deep Earth's interior". In: *Nature Communications* 8.1 (July 2017). DOI: 10.1038/ncomms15960. URL: https://doi.org/10.1038/ncomms15960.

[70] Valerio Cerantola et al. "Experimental investigation of $FeCO_3$ (siderite) stability in Earth's lower mantle using XANES spectroscopy". In: *American Mineralogist* 104.8 (Aug. 2019), pp. 1083–1091. DOI: 10.2138/am-2019-6428. URL: https://doi.org/10.2138/am-2019-6428.

[71] Barbara Lavina et al. "Structure of siderite $FeCO_3$ to 56 GPa and hysteresis of its spin-pairing transition". In: *Phys. Rev. B* 82 (6 Aug. 2010), p. 064110. DOI: 10.1103/PhysRevB.82.064110. URL: https://link.aps.org/doi/10.1103/PhysRevB.82.064110.

[72] Sergey S. Lobanov, Alexander F. Goncharov, and Konstantin D. Litasov. "Optical properties of siderite ($FeCO_3$) across the spin transition: Crossover to iron-rich carbonates in the lower mantle". In: *American Mineralogist* 100.5-6 (May 2015), pp. 1059–1064. DOI: 10.2138/am-2015-5053. URL: https://doi.org/10.2138/am-2015-5053.

[73]   A Mattila et al. "Pressure induced magnetic transition in siderite $FeCO_3$ studied by x-ray emission spectroscopy". In: *Journal of Physics: Condensed Matter* 19.38 (Aug. 2007), p. 386206. DOI: `10.1088/0953-8984/19/38/386206`. URL: `https://dx.doi.org/10.1088/0953-8984/19/38/386206`.

[74]   Jin Liu, Jung-Fu Lin, and Vitali B. Prakapenka. "High-Pressure Orthorhombic Ferromagnesite as a Potential Deep-Mantle Carbon Carrier". In: *Scientific Reports* 5.1 (Jan. 2015). DOI: `10.1038/srep07640`. URL: `https://doi.org/10.1038/srep07640`.

[75]   Christopher Weis et al. "Combining X-ray $K\beta_{1,3}$, valence-to-core, and X-ray Raman spectroscopy for studying Earth materials at high pressure and temperature: the case of siderite". In: *Journal of Analytical Atomic Spectrometry* 34.2 (2019), pp. 384–393. DOI: `10.1039/c8ja00247a`. URL: `https://doi.org/10.1039/c8ja00247a`.

[76]   Gabriel Blaj et al. "X-ray detectors at the Linac Coherent Light Source". In: *Journal of Synchrotron Radiation* 22.3 (Apr. 2015), pp. 577–583. DOI: `10.1107/s1600577515005317`. URL: `https://doi.org/10.1107/s1600577515005317`.

[77]   I. Klačková et al. "Radiation hardness study of the ePix100 sensor and ASIC under direct illumination at the European XFEL". In: *Journal of Instrumentation* 16.09 (Sept. 2021), P09009. DOI: `10.1088/1748-0221/16/09/p09009`. URL: `https://doi.org/10.1088/1748-0221/16/09/p09009`.

[78]   Han Hsu et al. "Anomalous thermal properties and spin crossover of ferromagnesite $(Mg, Fe)CO_3$". In: *Physical Review B* 103.5 (Feb. 2021). DOI: `10.1103/physrevb.103.054401`. URL: `https://doi.org/10.1103/physrevb.103.054401`.

[79]   Keng-Hsien Chao and Wen-Pin Hsieh. "Thermal Conductivity Anomaly in $(Fe_{0.78}, Mg_{0.22})CO_3$ Siderite Across Spin Transition of Iron". In: *Journal of Geophysical Research: Solid Earth* 124.2 (Feb. 2019), pp. 1388–1396. DOI: `10.1029/2018jb017003`. URL: `https://doi.org/10.1029/2018jb017003`.

[80]   Chrystèle Sanloup et al. "Polymerized 4-Fold Coordinated Carbonate Melts in the Deep Mantle". In: *Frontiers in Earth Science* 7 (Apr. 2019). DOI: `10.3389/feart.2019.00072`. URL: `https://doi.org/10.3389/feart.2019.00072`.

[81]   G Hölzer et al. "$K\alpha_{1,2}$andK$\beta_{1,3}$X-Ray emission lines of the3dtransition metals". In: *Phys. Rev. A* 56.6 (Dec. 1997), pp. 4554–4568.

[82]   Christopher Weis et al. *Pressure driven spin transition in siderite and mag-nesiosiderite single crystals*. Nov. 2017. DOI: 10.1038/s41598-017-16733-3. URL: https://doi.org/10.1038/s41598-017-16733-3.

[83]   Konstantin D. Litasov et al. "P–V–T equation of state of siderite to 33 GPa and 1673 K". In: *Physics of the Earth and Planetary Interiors* 224 (Nov. 2013), pp. 83–87. DOI: 10.1016/j.pepi.2013.07.011. URL: https://doi.org/10.1016/j.pepi.2013.07.011.

[84]   Choong-Shik Yoo et al. "Transformation and structure of silicatelike CO_2-V". In: *Phys. Rev. B* 87 (21 June 2013), p. 214103. DOI: 10.1103/PhysRevB.87.214103. URL: https://link.aps.org/doi/10.1103/PhysRevB.87.214103.

[85]   Anna Spivak et al. "Raman study of $MgCO_3$-$FeCO_3$ carbonate solid solution at high pressures up to 55 GPa". In: *Physics and Chemistry of Minerals* 41.8 (Apr. 2014), pp. 633–638. DOI: 10.1007/s00269-014-0676-y. URL: https://doi.org/10.1007/s00269-014-0676-y.

[86]   Xue Yong et al. "Crystal structures and dynamical properties of dense CO_2". In: *Proceedings of the National Academy of Sciences* 113.40 (Sept. 2016), pp. 11110–11115. DOI: 10.1073/pnas.1601254113. URL: https://doi.org/10.1073/pnas.1601254113.

[87]   C. Pardanaud et al. "Raman spectroscopy investigation of the H content of heated hard amorphous carbon layers". In: *Diamond and Related Materials* 34 (Apr. 2013), pp. 100–104. DOI: 10.1016/j.diamond.2013.02.009. URL: https://doi.org/10.1016/j.diamond.2013.02.009.

[88]   Sang-Heon Shim and Thomas S. Duffy. "Raman spectroscopy of Fe2O3 62 GPa". In: *American Mineralogist* 87.2-3 (Feb. 2002), pp. 318–326. DOI: 10.2138/am-2002-2-314. URL: https://doi.org/10.2138/am-2002-2-314.

[89]   Christian Albers et al. "Non-resonant and resonant X-ray emission at high pressure using a von Hámos setup: the case of FeO". In: *Journal of Physics: Conference Series* 2380.1 (Dec. 2022), p. 012128. DOI: 10.1088/1742-6596/2380/1/012128. URL: https://doi.org/10.1088/1742-6596/2380/1/012128.

[90]   H. P. Liermann et al. "Novel experimental setup for megahertz X-ray diffrac-tion in a diamond anvil cell at the High Energy Density (HED) instrument of the European X-ray Free-Electron Laser (EuXFEL)". In: *Journal of Syn-chrotron Radiation* 28.3 (Apr. 2021). DOI: 10.1107/s1600577521002551. URL: https://doi.org/10.1107/s1600577521002551.

[91]   N. Medvedev, H. O. Jeschke, and B. Ziaja. "Nonthermal graphitization of diamond induced by a femtosecond X-ray laser pulse". In: *Physical Review B* 88.22 (Dec. 2013). DOI: 10.1103/physrevb.88.224304. URL: https://doi.org/10.1103/physrevb.88.224304.

[92]   A. R. Oganov et al. "Structure, Bonding, and Mineralogy of Carbon at Extreme Conditions". In: *Reviews in Mineralogy and Geochemistry* 75.1 (Jan. 2013), pp. 47–77. DOI: 10.2138/rmg.2013.75.3. URL: https://doi.org/10.2138/rmg.2013.75.3.

[93]   Muhammad Ijaz Anwar et al. "Hard X-Ray von Hamos Spectrometer for Single-Pulse Emission Spectroscopy". In: *Journal of the Korean Physical Society* 75.7 (Oct. 2019), pp. 494–497. DOI: 10.3938/jkps.75.494. URL: https://doi.org/10.3938/jkps.75.494.

[94]   Bob Nagler et al. "The Matter in Extreme Conditions instrument at the Linac Coherent Light Source". In: *Journal of Synchrotron Radiation* 22.3 (Apr. 2015), pp. 520–525. DOI: 10.1107/s1600577515004865. URL: https://doi.org/10.1107/s1600577515004865.

[95]   T.R. Preston et al. "Design and performance characterisation of the HAPG von Hámos Spectrometer at the High Energy Density Instrument of the European XFEL". In: *Journal of Instrumentation* 15.11 (Nov. 2020), P11033–P11033. DOI: 10.1088/1748-0221/15/11/p11033. URL: https://doi.org/10.1088/1748-0221/15/11/p11033.

[96]   H. J. Lee et al. "X-Ray Thomson-Scattering Measurements of Density and Temperature in Shock-Compressed Beryllium". In: *Physical Review Letters* 102.11 (Mar. 2009). DOI: 10.1103/physrevlett.102.115001. URL: https://doi.org/10.1103/physrevlett.102.115001.

[97]   Siegfried H. Glenzer and Ronald Redmer. "X-ray Thomson scattering in high energy density plasmas". In: *Reviews of Modern Physics* 81.4 (Dec. 2009), pp. 1625–1663. DOI: 10.1103/revmodphys.81.1625. URL: https://doi.org/10.1103/revmodphys.81.1625.

[98]   P. Neumayer et al. "Plasmons in Strongly Coupled Shock-Compressed Matter". In: *Physical Review Letters* 105.7 (Aug. 2010). DOI: 10.1103/physrevlett.105.075003. URL: https://doi.org/10.1103/physrevlett.105.075003.

[99]   B. B. L. Witte et al. "Warm Dense Matter Demonstrating Non-Drude Conductivity from Observations of Nonlinear Plasmon Damping". In: *Physical*

Review Letters 118.22 (May 2017). DOI: `10.1103/physrevlett.118.225001`. URL: `https://doi.org/10.1103/physrevlett.118.225001`.

[100] T. R. Preston et al. "Measurements of the momentum-dependence of plasmonic excitations in matter around 1 Mbar using an X-ray free electron laser". In: *Applied Physics Letters* 114.1 (Jan. 2019), p. 014101. DOI: `10.1063/1.5070140`. URL: `https://doi.org/10.1063/1.5070140`.

[101] Roberto Alonso-Mori et al. "A multi-crystal wavelength dispersive X-Ray spectrometer". In: *Review of Scientific Instruments* 83.7 (July 2012), p. 073114. DOI: `10.1063/1.4737630`. URL: `https://doi.org/10.1063/1.4737630`.

[102] J. Szlachetko et al. "A von Hamos X-Ray spectrometer based on a segmented-type diffraction crystal for single-shot X-Ray emission spectroscopy and time-resolved resonant inelastic X-Ray scattering studies". In: *Review of Scientific Instruments* 83.10 (Oct. 2012), p. 103105. DOI: `10.1063/1.4756691`. URL: `https://doi.org/10.1063/1.4756691`.

[103] Jung-Fu Lin et al. "X-ray emission spectroscopy with a laser-heated diamond anvil cell: a new experimental probe of the spin state of iron in the Earth's interior". In: *Journal of Synchrotron Radiation* 12.5 (Aug. 2005), pp. 637–641. DOI: `10.1107/s0909049505020741`. URL: `https://doi.org/10.1107/s0909049505020741`.

[104] Eaazhisai Kandiah et al. "CM01: a facility for cryo-electron microscopy at the European Synchrotron". In: *Acta Crystallographica Section D Structural Biology* 75.6 (May 2019), pp. 528–535. DOI: `10.1107/s2059798319006880`. URL: `https://doi.org/10.1107/s2059798319006880`.

[105] *JJ X-Ray.* June 2021. URL: `https://www.jjxray.dk/`.

[106] A Mozzanica et al. "Prototype characterization of the JUNGFRAU pixel detector for SwissFEL". In: *J. Instrum.* 9.05 (May 2014), pp. C05010–C05010.

[107] Ch. J. Sahle et al. "A compact von Hámos spectrometer for parallel X-Ray Raman scattering and X-Ray emission spectroscopy at ID20 of the European Synchrotron Radiation Facility". In: *Journal of Synchrotron Radiation* 30.1 (Jan. 2023). DOI: `10.1107/s1600577522011171`. URL: `https://doi.org/10.1107/s1600577522011171`.

[108] S. Takagi. "Dynamical theory of diffraction applicable to crystals with any kind of small distortion". In: *Acta Crystallographica* 15.12 (Dec. 1962), pp. 1311–1312. DOI: `10.1107/s0365110x62003473`. URL: `https://doi.org/10.1107/s0365110x62003473`.

16

[109] Satio Takagi. "A Dynamical Theory of Diffraction for a Distorted Crystal". In: *Journal of the Physical Society of Japan* 26.5 (May 1969), pp. 1239–1253. DOI: 10.1143/jpsj.26.1239. URL: https://doi.org/10.1143/jpsj.26.1239.

[110] Daniel Taupin. "Théorie dynamique de la diffraction des rayons X par les cristaux déformés". In: *Bulletin de la Société française de Minéralogie et de Cristallographie* 87.4 (1964), pp. 469–511. DOI: 10.3406/bulmi.1964.5769. URL: https://doi.org/10.3406/bulmi.1964.5769.

[111] M. Bech et al. "X-ray imaging with the PILATUS 100k detector". In: *Applied Radiation and Isotopes* 66.4 (Apr. 2008), pp. 474–478. DOI: 10.1016/j.apradiso.2007.10.003. URL: https://doi.org/10.1016/j.apradiso.2007.10.003.

[112] U. Zastrau et al. "Resolving Ultrafast Heating of Dense Cryogenic Hydrogen". In: *Physical Review Letters* 112.10 (Mar. 2014). DOI: 10.1103/physrevlett.112.105002. URL: https://doi.org/10.1103/physrevlett.112.105002.

[113] Jan Grünert et al. "X-ray photon diagnostics at the European XFEL". In: *Journal of Synchrotron Radiation* 26.5 (Aug. 2019), pp. 1422–1431. DOI: 10.1107/s1600577519006611. URL: https://doi.org/10.1107/s1600577519006611.

[114] G. Hölzer et al. "$K\alpha_{1,2}$ and $K\beta_{1,3}$ X-ray emission lines of the 3d transition metals". In: *Physical Review A* 56.6 (Dec. 1997), pp. 4554–4568. DOI: 10.1103/physreva.56.4554. URL: https://doi.org/10.1103/physreva.56.4554.

[115] Y. Ito et al. "Structure of high-resolution $K\beta_{1,3}$ X-ray emission spectra for the elements from Ca to Ge". In: *Phys. Rev. A* 97 (5 May 2018), p. 052505. DOI: 10.1103/PhysRevA.97.052505. URL: https://link.aps.org/doi/10.1103/PhysRevA.97.052505.

[116] A. Brunetti et al. "A library for X-ray–matter interaction cross sections for X-ray fluorescence applications". In: *Spectrochimica Acta Part B: Atomic Spectroscopy* 59.10-11 (Oct. 2004), pp. 1725–1731. DOI: 10.1016/j.sab.2004.03.014. URL: https://doi.org/10.1016/j.sab.2004.03.014.

[117] V M Elkin et al. "A wide-range multiphase equation of state for platinum". In: *Journal of Physics: Condensed Matter* 32.43 (July 2020), p. 435403. DOI: 10.1088/1361-648x/aba428. URL: https://doi.org/10.1088/1361-648x/aba428.

[118] Jung-Fu Lin et al. "Spin Transition Zone in Earth's Lower Mantle". In: *Science* 317.5845 (2007), pp. 1740–1743. DOI: 10.1126/science.1144997. eprint: https://www.science.org/doi/pdf/10.1126/science.1144997. URL: https://www.science.org/doi/abs/10.1126/science.1144997.

[119] Jung-Fu Lin, Steven D. Jacobsen, and Renata M. Wentzcovitch. "Electronic Spin Transition of Iron in the Earth's Deep Mantle". In: *Eos, Transactions American Geophysical Union* 88.2 (Jan. 2007), p. 13. DOI: 10.1029/2007eo020001. URL: https://doi.org/10.1029/2007eo020001.

[120] Jung-Fu Lin et al. "Stability of magnesiowüstite in Earth's lower mantle". In: *Proceedings of the National Academy of Sciences* 100.8 (Mar. 2003), pp. 4405–4408. DOI: 10.1073/pnas.252782399. URL: https://doi.org/10.1073/pnas.252782399.

[121] S Waidmann et al. "Local-field effects and anisotropic plasmon dispersion in diamond". In: *Phys. Rev. B Condens. Matter* 61.15 (Apr. 2000), pp. 10149–10153.

[122] Igor I. Vlasov et al. "Recent Results on Characterization of Detonation Nanodiamonds". In: *Ultananocrystalline Diamond*. Elsevier, 2012, pp. 291–326. DOI: 10.1016/b978-1-4377-3465-2.00009-8. URL: https://doi.org/10.1016/b978-1-4377-3465-2.00009-8.

[123] L. Wollenweber et al. "High-resolution inelastic X-Ray scattering at the high energy density scientific instrument at the European X-Ray Free-Electron Laser". In: *Review of Scientific Instruments* 92.1 (Jan. 2021), p. 013101. DOI: 10.1063/5.0022886. URL: https://doi.org/10.1063/5.0022886.

[124] Th. Schedel-Niedrig et al. "In Situ X-ray Absorption Spectroscopy in the Soft Energy Range: Novel Prospects for the Chemical Characterization of Solid State Surfaces at High Pressure And High Temperature". In: *MRS Proceedings* 678 (2001). DOI: 10.1557/proc-678-ee8.3.1. URL: https://doi.org/10.1557/proc-678-ee8.3.1.

[125] J. Amann et al. "Demonstration of self-seeding in a hard-X-ray free-electron laser". In: *Nature Photonics* 6.10 (Aug. 2012), pp. 693–698. DOI: 10.1038/nphoton.2012.180. URL: https://doi.org/10.1038/nphoton.2012.180.

[126] S Clifford. "The Evolution of the Martian Hydrosphere: Implications for the Fate of a Primordial Ocean and the Current State of the Northern Plains". In: *Icarus* 154.1 (Nov. 2001), pp. 40–79. DOI: 10.1006/icar.2001.6671. URL: https://doi.org/10.1006/icar.2001.6671.

[127]   P. Kenneth Seidelmann et al. "Report of the IAU/IAG Working Group on cartographic coordinates and rotational elements: 2006". In: *Celestial Mechanics and Dynamical Astronomy* 98.3 (July 2007), pp. 155–180. DOI: `10.1007/s10569-007-9072-y`. URL: `https://doi.org/10.1007/s10569-007-9072-y`.

[128]   Caleb I. Fassett and James W. Head. "Valley network-fed, open-basin lakes on Mars: Distribution and implications for Noachian surface and subsurface hydrology". In: *Icarus* 198.1 (Nov. 2008), pp. 37–56. DOI: `10.1016/j.icarus.2008.06.016`. URL: `https://doi.org/10.1016/j.icarus.2008.06.016`.

[129]   Michael H. Carr and James W. Head. "Geologic history of Mars". In: *Earth and Planetary Science Letters* 294.3-4 (June 2010), pp. 185–203. DOI: `10.1016/j.epsl.2009.06.042`. URL: `https://doi.org/10.1016/j.epsl.2009.06.042`.

[130]   J. P. Grotzinger et al. "A Habitable Fluvio-Lacustrine Environment at Yellowknife Bay, Gale Crater, Mars". In: *Science* 343.6169 (Jan. 2014). DOI: `10.1126/science.1242777`. URL: `https://doi.org/10.1126/science.1242777`.

[131]   Jennifer L. Eigenbrode et al. "Organic matter preserved in 3-billion-year-old mudstones at Gale crater, Mars". In: *Science* 360.6393 (June 2018), pp. 1096–1101. DOI: `10.1126/science.aas9185`. URL: `https://doi.org/10.1126/science.aas9185`.

[132]   John W Morgan and Edward Anders. "Chemical composition of Mars". In: *Geochimica et Cosmochimica Acta* 43.10 (Oct. 1979), pp. 1601–1610. DOI: `10.1016/0016-7037(79)90180-7`. URL: `https://doi.org/10.1016/0016-7037(79)90180-7`.

[133]   H. Waenke and G. Dreibus. "Chemical Composition and Accretion History of Terrestrial Planets". In: *Philosophical Transactions of the Royal Society of London Series A* 325.1587 (July 1988), pp. 545–557. DOI: `10.1098/rsta.1988.0067`.

[134]   Thomas H. Burbine and Kevin M. O'Brien. "Determining the possible building blocks of the Earth and Mars". In: *Meteoritics & Planetary Science* 39.5 (May 2004), pp. 667–681. DOI: `10.1111/j.1945-5100.2004.tb00110.x`. URL: `https://doi.org/10.1111/j.1945-5100.2004.tb00110.x`.

[135]   P. B. Esposito et al. "Gravity and tophography." In: *Mars.* Ed. by Michael George. 1992, pp. 209–248.

[136] W. M. Folkner et al. "Interior Structure and Seasonal Mass Redistribution of Mars from Radio Tracking of Mars Pathfinder". In: *Science* 278.5344 (Dec. 1997), pp. 1749–1752. DOI: `10.1126/science.278.5344.1749`. URL: `https://doi.org/10.1126/science.278.5344.1749`.

[137] C. F. Yoder et al. "Fluid Core Size of Mars from Detection of the Solar Tide". In: *Science* 300.5617 (Apr. 2003), pp. 299–303. DOI: `10.1126/science.1079645`. URL: `https://doi.org/10.1126/science.1079645`.

[138] Frank Sohl, Gerald Schubert, and Tilman Spohn. "Geophysical constraints on the composition and structure of the Martian interior". In: *Journal of Geophysical Research* 110.E12 (2005). DOI: `10.1029/2005je002520`. URL: `https://doi.org/10.1029/2005je002520`.

[139] A. Khan et al. "A Geophysical Perspective on the Bulk Composition of Mars". In: *Journal of Geophysical Research: Planets* 123.2 (Feb. 2018), pp. 575–611. DOI: `10.1002/2017je005371`. URL: `https://doi.org/10.1002/2017je005371`.

[140] V. N. Zharkov and T. V. Gudkova. "Construction of Martian Interior Model". In: *Solar System Research* 39.5 (Sept. 2005), pp. 343–373. DOI: `10.1007/s11208-005-0049-7`. URL: `https://doi.org/10.1007/s11208-005-0049-7`.

[141] Abby Kavner, Thomas S. Duffy, and Guoyin Shen. "Phase stability and density of FeS at high pressures and temperatures: implications for the interior structure of Mars". In: *Earth and Planetary Science Letters* 185.1-2 (Feb. 2001), pp. 25–33. DOI: `10.1016/s0012-821x(00)00356-3`. URL: `https://doi.org/10.1016/s0012-821x(00)00356-3`.

[142] A. Rivoldini et al. "Geodesy constraints on the interior structure and composition of Mars". In: *Icarus* 213.2 (June 2011), pp. 451–472. DOI: `10.1016/j.icarus.2011.03.024`. URL: `https://doi.org/10.1016/j.icarus.2011.03.024`.

[143] Yingwei Fei, Constance M. Bertka, and Larry W. Finger. "High-Pressure Iron-Sulfur Compound, Fe_3S_2, and Melting Relations in the Fe-FeS System". In: *Science* 275.5306 (Mar. 1997), pp. 1621–1623. DOI: `10.1126/science.275.5306.1621`. URL: `https://doi.org/10.1126/science.275.5306.1621`.

[144] Liudmila Chudinovskikh and Reinhard Boehler. "Eutectic melting in the system Fe–S to 44 GPa". In: *Earth and Planetary Science Letters* 257.1-2

(May 2007), pp. 97–103. DOI: 10.1016/j.epsl.2007.02.024. URL: https://doi.org/10.1016/j.epsl.2007.02.024.

[145] G. Morard et al. "In situ determination of Fe–Fe3S phase diagram and liquid structural properties up to 65 GPa". In: *Earth and Planetary Science Letters* 272.3-4 (Aug. 2008), pp. 620–626. DOI: 10.1016/j.epsl.2008.05.028. URL: https://doi.org/10.1016/j.epsl.2008.05.028.

[146] Claire C. Zurkowski et al. "The crystal structure of Fe$_2$S at 90 GPa based on single-crystal X-ray diffraction techniques". In: *American Mineralogist* 107.4 (Apr. 2022), pp. 739–743. DOI: 10.2138/am-2022-7973. URL: https://doi.org/10.2138/am-2022-7973.

[147] F. Keller-Besrest and G. Collin. "Structural aspects of the α transition in stoichiometric FeS: Identification of the high-temperature phase". In: *Journal of Solid State Chemistry* 84.2 (Feb. 1990), pp. 194–210. DOI: 10.1016/0022-4596(90)90319-s. URL: https://doi.org/10.1016/0022-4596(90)90319-s.

[148] K. Kusaba et al. "Second-order phase transition of FeS under high pressure and temperature". In: *Journal of Physics and Chemistry of Solids* 61.9 (Sept. 2000), pp. 1483–1487. DOI: 10.1016/s0022-3697(00)00005-6. URL: https://doi.org/10.1016/s0022-3697(00)00005-6.

[149] Y. Fei et al. "Structures of FeS Polymorphs at High Pressure and Temperature." In: *The review of high pressure science and technology* 7 (1998), pp. 55–58. DOI: 10.4131/jshpreview.7.55. URL: https://doi.org/10.4131/jshpreview.7.55.

[150] Satoru Urakawa et al. "Phase relationships and equations of state for FeS at high pressures and temperatures and implications for the internal structure of Mars". In: *Physics of the Earth and Planetary Interiors* 143-144 (June 2004), pp. 469–479. DOI: 10.1016/j.pepi.2003.12.015. URL: https://doi.org/10.1016/j.pepi.2003.12.015.

[151] H. E. King and C. T. Prewitt. "High-pressure and high-temperature polymorphism of iron sulfide (FeS)". In: *Acta Crystallographica Section B Structural Crystallography and Crystal Chemistry* 38.7 (July 1982), pp. 1877–1887. DOI: 10.1107/s0567740882007523. URL: https://doi.org/10.1107/s0567740882007523.

[152]   R. J. Nelmes et al. "Structure of the high-pressure phase III of iron sulfide". In: *Physical Review B* 59.14 (Apr. 1999), pp. 9048–9052. DOI: `10.1103/physrevb.59.9048`. URL: `https://doi.org/10.1103/physrevb.59.9048`.

[153]   R. Boehler. "Melting of the FeFeO and the FeFeS systems at high pressure: Constraints on core temperatures". In: *Earth and Planetary Science Letters* 111.2-4 (July 1992), pp. 217–227. DOI: `10.1016/0012-821x(92)90180-4`. URL: `https://doi.org/10.1016/0012-821x(92)90180-4`.

[154]   Shigeaki Ono et al. "High-pressure phase transformations of FeS: Novel phases at conditions of planetary cores". In: *Earth and Planetary Science Letters* 272.1-2 (July 2008), pp. 481–487. DOI: `10.1016/j.epsl.2008.05.017`. URL: `https://doi.org/10.1016/j.epsl.2008.05.017`.

[155]   Yingwei Fei and Constance Bertka. "The Interior of Mars". In: *Science* 308.5725 (May 2005), pp. 1120–1121. DOI: `10.1126/science.1110531`. URL: `https://doi.org/10.1126/science.1110531`.

[156]   J. P. Rueff et al. "Pressure-Induced High-Spin to Low-Spin Transition in FeS Evidenced by X-Ray Emission Spectroscopy". In: *Physical Review Letters* 82 (1998), pp. 3284–3287.

[157]   Georg Spiekermann et al. "A portable on-axis laser-heating system for near-90° X-ray spectroscopy: application to ferropericlase and iron silicide". In: *Journal of Synchrotron Radiation* 27.2 (Feb. 2020), pp. 414–424. DOI: `10.1107/s1600577519017041`. URL: `https://doi.org/10.1107/s1600577519017041`.

[158]   W. G. Marshall et al. "High-pressure neutron-diffraction study of FeS". In: *Physical Review B* 61.17 (May 2000), pp. 11201–11204. DOI: `10.1103/physrevb.61.11201`. URL: `https://doi.org/10.1103/physrevb.61.11201`.

[159]   Jian-Min Shen and Yi-Tao Feng. "Formation of Flower-Like Carbon Nanosheet Aggregations and Their Electrochemical Application". In: *The Journal of Physical Chemistry C* 112.34 (July 2008), pp. 13114–13120. DOI: `10.1021/jp802285c`. URL: `https://doi.org/10.1021/jp802285c`.

[160]   S. Ono and T. Kikegawa. "High-pressure study of FeS, between 20 and 120 GPa, using synchrotron X-ray powder diffraction". In: *American Mineralogist* 91.11-12 (Nov. 2006), pp. 1941–1944. DOI: `10.2138/am.2006.2347`. URL: `https://doi.org/10.2138/am.2006.2347`.

[161] Andrew J. Campbell and Dion L. Heinz. "Compression of KCl in the B2 structure to 56 GPa". In: *Journal of Physics and Chemistry of Solids* 52.3 (Jan. 1991), pp. 495–499. DOI: 10.1016/0022-3697(91)90181-x. URL: https://doi.org/10.1016/0022-3697(91)90181-x.

[162] Doris Breuer, Tina Rueckriemen, and Tilman Spohn. "Iron snow, crystal floats, and inner-core growth: modes of core solidification and implications for dynamos in terrestrial planets and moons". In: *Progress in Earth and Planetary Science* 2.1 (Nov. 2015). DOI: 10.1186/s40645-015-0069-y. URL: https://doi.org/10.1186/s40645-015-0069-y.

[163] Ryan Stewart McWilliams. *Femtosecond Hard X-ray Studies at High Static Pressure.* en. 2019. DOI: 10.22003/XFEL.EU-DATA-002292-00. URL: https://in.xfel.eu/metadata/doi/10.22003/XFEL.EU-DATA-002292-00.

[164] Steffen Hauf et al. "The Karabo distributed control system". In: *Journal of Synchrotron Radiation* 26.5 (Aug. 2019), pp. 1448–1461. DOI: 10.1107/s1600577519006696. URL: https://doi.org/10.11072Fs1600577519006696.

[165] J. Eggert et al. "Hugoniot Data for Helium in the Ionization Regime". In: *Physical Review Letters* 100.12 (Mar. 2008). DOI: 10.1103/physrevlett.100.124503. URL: https://doi.org/10.1103/physrevlett.100.124503.

[166] Marius Millot et al. "Experimental evidence for superionic water ice using shock compression". In: *Nature Physics* 14.3 (Feb. 2018), pp. 297–302. DOI: 10.1038/s41567-017-0017-4. URL: https://doi.org/10.1038/s41567-017-0017-4.

[167] S. Brygoo et al. "Evidence of hydrogen-helium immiscibility at Jupiter-interior conditions". In: *Nature* 593.7860 (May 2021), pp. 517–521. DOI: 10.1038/s41586-021-03516-0. URL: https://doi.org/10.1038/s41586-021-03516-0.